Supplementary Information

Yolk-Shell Zeolite Nanoreactors Enable Multi-Poison Resistance for NO_x Reduction

Yonglong Li,[a, b‡] Guobo Li,[a‡] Rongxing Li,[a] Jian Ji,[a] Xiaonan Hu,[a] Fengbo Yu,[a] Wenming Liu,[c] Hongmei Li,[d] Min Liu,[d, e] and Honggen Peng[a, c*]

[a] *Engineering Research Center of Watershed Carbon Neutrality of Ministry of Education and School of Resources and Environment, Nanchang University, Nanchang, Jiangxi, 330031, China*

[b] *School of Life Sciences, Jinggangshan University, Ji'an, Jiangxi, 343009, China*

[c] *School of Chemistry and Chemical Engineering, Nanchang University, Nanchang, Jiangxi, 330031, China*

[d] *Hunan Joint International Research Center for Carbon Dioxide Resource Utilization, State Key Laboratory of Powder Metallurgy, School of Physics, Central South University, Changsha, Hunan, 410083, China*

[e] *School of Metallurgy and Environment, Central South University, Changsha, Hunan, 410083, China*

[‡] *These authors contributed equally to this work.*

[*] Corresponding author, E-mail: penghonggen@ncu.edu.cn (H.G. Peng)

(This Supplementary Information includes **88 pages**, **61 figures**, and **7 tables**)

List of Content

Supplementary Methods

Catalyst preparation

The ZSM-5 zeolite (Si/Al = 100) was synthesized using a hydrothermal method. Tetrapropylammonium hydroxide (TPAOH, 25%), tetraethoxysilane (TEOS, AR), and aluminum isopropoxide (98%) were used as the starting materials. Initially, 90.7 mL of TPAOH was combined with 94.5 mL of TEOS, and the resulting mixture was stirred at 35 °C for 3 h. A stoichiometric quantity of aluminum isopropoxide was then dissolved in 209 mL of water, and the resulting suspension was stirred at 85 °C for 3 h. Following this, the aluminum isopropoxide solution was added dropwise to the TPAOH-TEOS mixture. The combined solution was stirred at 35 °C for 3 h, then heated at 85 °C for an additional hour to remove the alcohols formed during the hydrolysis of aluminum isopropoxide and TEOS. Water was subsequently added to adjust the volume, and the mixed solution underwent hydrothermal treatment at 170 °C for 72 h. The product was then washed with water, dried at 110 °C for 12 h, and calcined at 540 °C for 6 h (2 °C min^{-1}).

The supported $MnFeO_x$/ZSM-5 catalyst was prepared via an impregnation method. $FeCl_3 \cdot 6H_2O$ and $MnCl_2 \cdot 4H_2O$ served as the precursors. The total MnO_2 and Fe_2O_3 active components constituted 15% with a Mn/Fe molar ratio of 1:1. Initially, add appropriate amounts of the two metal precursors to 20 ml of ethanol solution, stir to dissolve, then add 2.0 g of ZSM-5 zeolite and continue stirring at room temperature for 12 h. Following this, the mixture was dried under stirring at 50 °C for 20 h. Finally, the resulting yellow powder was calcined at 500 °C for 4 h (2 °C min^{-1}). It should be noted

that the sample calcined once for 4 h was only used for the subsequent preparation of yolk-shell structured nanoreactors. Since the complete fabrication process of the yolk-shell structured nanoreactors described below involves two consecutive calcinations at 500 °C for 4 h each, to ensure the consistency of catalyst calcination conditions and the comparability of experiments, various supported catalysts (including $MnFeO_x$/ZSM-5, $MnFeO_x$/S-1, and $MnFeO_x$/Hollow-ZSM-5 below) subjected to two calcinations at 500 °C for 4 h were also prepared in parallel for all catalytic performance tests and characterization analyses.

The yolk-shell structured $MnFeO_x$@YS-ZSM-5 nanoreactor was synthesized by treating the $MnFeO_x$/ZSM-5 catalyst with an aqueous TPAOH solution. In the first step, 8.03 mL of TPAOH was mixed with 25.1 mL of water. Next, 1.66 g of $MnFeO_x$/ZSM-5 was introduced into the aqueous solution. The resulting mixture was then hydrothermally processed at 170 °C for 72 h. The product was washed with water, dried at 80 °C for 10 h, and subsequently calcined at 500 °C for 4 h (2 °C min^{-1}). The actual total MnO_2 and Fe_2O_3 content in the sample, determined by ICP, was approximately 15 wt.%.

The pure $MnFeO_x$ metal oxides catalysts with a Mn/Fe molar ratio of 1:1 was synthesized using the co-precipitation method. Typically, moderate $MnCl_2 \cdot 4H_2O$ and $FeCl_3 \cdot 6H_2O$ were first dissolved in distilled water. After 3 h of stirring, diluted ammonia solution was slowly added to the above mixed solution under vigorous stirring until the pH was approximately 10. After stirring for 5 h, then the obtained suspension was filtered and washed with deionized water and ethanol several times to remove

residual chloride ions. Finally, the precipitate was dried at 80 °C for 12 h and subsequently calcined, the calcination procedures were identical to that used for the preparation $MnFeO_x$@YS-ZSM-5 nanoreactor.

The preparation method of the S-1 zeolite was the same as that of the ZSM-5 zeolite, except that aluminum isopropoxide was not added during the preparation process. The preparation method of the hollow ZSM-5 zeolite (named Hollow-ZSM-5) was consistent with that of the $MnFeO_x$@YS-ZSM-5 nanoreactor, except that ZSM-5 was used instead of $MnFeO_x$/ZSM-5 for the TPAOH hydrothermal treatment. The supported $MnFeO_x$/S-1 and $MnFeO_x$/Hollow-ZSM-5 catalysts were prepared in the same method as the $MnFeO_x$/ZSM-5 catalyst, both by the impregnation method, and only the supports need to be changed.

The K-poisoned catalysts were obtained by wet impregnation method. Typically, fresh catalysts were added to an aqueous KNO_3 solution and stirred at 35 °C for 30 min. Subsequently, the mixture was stirred at 80 °C to evaporate the water to dryness. The dried powder was placed in a muffle furnace and calcined at 500 °C for 30 min (heating rate was 5 °C min^{-1}), yielding K-poisoned samples with a 0.5 wt.% K_2O loading. Catalysts after K poisoning were named with "K-" as the prefix, such as K-$MnFeO_x$@YS-ZSM-5.

To evaluate the SO_2 poisoning resistance of the catalysts, the long-term stability tests for SO_2 poisoning resistance was performed on the catalysts under the following conditions: at 246 °C, 100 mg of fresh catalyst was first exposed to NH_3-SCR reaction gas (500 ppm NO, 500 ppm NH_3, 5 vol.% H_2O, 5 vol.% O_2, with N_2 as the balance gas,

total gas flow rate was controlled at 100 mL min^{-1}) for 1.5 h. Subsequently, SO_2 was introduced into the system (with a SO_2 concentration of 50 ppm in the mixed gas), and the reaction was maintained stably for an additional 7.5 h. Thereafter, SO_2 was removed, allowing the catalyst to continue reacting in SO_2-free NH_3-SCR reaction gas for a further 10.5 h. The SO_2-poisoned catalyst obtained after the entire test was designated with the prefix "S-", such as S-$MnFeO_x$@YS-ZSM-5. Furthermore, SO_2 pre-sulfation treatments were also carried on the catalysts. The detailed procedure is as follows: 100 mg of fresh catalyst was loaded into a quartz tube and fed with a pretreatment gas (gas composition: 50 ppm SO_2, 500 ppm NO, 500 ppm NH_3, 5 vol.% H_2O, 5 vol.% O_2, with N_2 as the balance gas), and the total gas flow rate was controlled at 100 mL min^{-1}. The pre-sulfation treatment was conducted at 200 or 300 °C for 3 h. After the pre-sulfation treatment, all gases were immediately shut off, and the catalyst was cooled to room temperature before testing its NH_3-SCR catalytic activity. Catalysts subjected to SO_2 pre-sulfation treatment were named with "SO_2-" as the prefix, such as SO_2-$MnFeO_x$@YS-ZSM-5.

To investigate the universality of the impregnation-dissolution-recrystallization (IDR) method for preparing yolk-shell structured nanoreactor materials, supported $MnCoO_x$/ZSM-5 and $MnCeO_x$/ZSM-5 samples were prepared, as well as the corresponding yolk-shell structured $MnCoO_x$@YS-ZSM-5 and $MnCeO_x$@YS-ZSM-5 nanoreactor materials, following the same experimental procedures above. For reagent usage, the Mn source remained unchanged, while the Co source employed was $CoCl_2 \cdot 6H_2O$ and the Ce source was $CeCl_3 \cdot 7H_2O$.

Catalytic test

NH_3-SCR performances were conducted through the use of a fixed-bed quartz flow reactor (with an inner diameter of 6 mm). The gas mixture comprised 500 ppm of NO, 500 ppm of NH_3, 5 vol. % O_2, 5 vol. % H_2O and N_2 as the balance gas, maintaining a total flow rate of 100 mL min^{-1}. 100 mg of catalyst (40–60 mesh) was used for each NH_3-SCR test, this arrangement led to a weight hourly space velocity (WHSV) of 60,000 mL $g_{cat.}^{-1}$ h^{-1}. The assessment of catalytic activity involved ramping up the fixed-bed temperature at a rate of 2 °C min^{-1}. The composition and concentration of the outlet gases were continuously monitored using Fourier transform infrared (FT-IR) spectroscopy with an Antaris IGS-Gas Analyzer (Thermo Fisher Scientific Inc., Waltham, MA, USA) equipped with a 2-meter gas cell. NO_x conversion and N_2 selectivity were figured out using the given equations:

NO_x conversion (X_{NO_x}) and N_2 selectivity (S_{N_2}) were then calculated using the following equations:

$$X_{NO_x} = \left(1 - \frac{[NO_x]_{outlet}}{[NO_x]_{inlet}}\right) \times 100\% \quad (1)$$

$$S_{N_2} = \left(1 - \frac{2[N_2O]_{outlet}}{[NO_x]_{inlet} - [NO_x]_{outlet} + [NH_3]_{inlet} - [NH_3]_{outlet}}\right) \times 100\% \quad (2)$$

where $[NO_x] = [NO] + [NO_2]$, $[NH_3]_{inlet}$, $[NO_x]_{inlet}$, $[NO_x]_{outlet}$, $[N_2O]_{outlet}$, and $[NO_x]_{outlet}$ are the relative gas concentrations at the input and output, respectively.

Kinetic test

In the investigation of NH_3-SCR kinetics over $MnFeO_x$, $MnFeO_x$/S-1, $MnFeO_x$/ZSM-5, and $MnFeO_x$@YS-ZSM-5 catalysts, a fixed-bed quartz reactor was employed. Within a quartz tube of 6 mm inner diameter, 25 mg of catalyst (40–60 mesh) and 75 mg of inert quartz sand were packed. Although maintaining the same composition and concentration of reaction gases as NH_3-SCR, the total flow rate was adjusted to 350 mL min^{-1}, thereby fixing the WHSV at 840,000 mL $g_{cat.}^{-1}$ h^{-1} and ensuring NO_x conversion rates remained below 18%. The low NO_x conversion and the absence of mass and heat transfer limitations confirm the occurrence of the reaction in the kinetic region. To further corroborate this, calculations of the Weisz-Prater criterion and the Mears criterion were undertaken[1,2], systematically excluding the influences of mass transport and heat transfer limitations, respectively. The determination of reaction rate (r, in mol $g_{cat.}^{-1}$ s^{-1}), reaction rate coefficient (k, in mol $g_{cat.}^{-1}$ s^{-1}) and apparent activation energy (E_a, in kJ mol^{-1}) for the NH_3-SCR kinetic reactions involves conducting experiments at varying temperatures to derive the NO_x conversion using the following formulas:

$$r = \frac{X_{NO_x} F_{NO_x}}{m_{cat.}} \tag{3}$$

$$k = -\frac{F_{NO_x}}{m_{cat.}} \times \ln\left(1 - X_{NO_x}\right) \tag{4}$$

$$\ln k = -\frac{E_a}{R_g T} + \ln A \tag{5}$$

Here, F_{NO_x} represents the gas flow rate (in mol s^{-1}) of NO_x, $m_{cat.}$ is the mass of the catalyst (in g), A is the pre-exponential factor, T is the reaction temperature (in K), R_g is the gas constant (in kJ mol^{-1} K^{-1}). The reaction orders for NO and NH_3 are

typically set as first and zero, respectively, and the E_a can be calculated from the Arrhenius plots of the reaction rate coefficient.

Catalyst characterization

X-ray diffraction (XRD) patterns were recorded on an intelligent X-ray diffractometer (SmartLab9KW) produced by Rigaku Corporation of Japan, with Cu Kα radiation (40 kV and 30 mA) from 5–80°. N_2 adsorption and desorption isotherms were obtained on Kubo X1000 high-performance pore size-specific surface area analyzer (Builder, Beijing) after pretreating at 300 °C for 5 h. X-ray photoelectron spectra (XPS) were carried out on Thermo ESCALAB 250Xi system with Al Kα radiation, and the spectra was calibrated against the standardized C 1s peak at 284.8 eV. Transmission electron microscopy (TEM) and elemental mapping images were obtained using a JEOL 3000F TEM working at 300 kV equipped with an energy dispersive spectroscopy (EDS) detector. Before conducting TEM investigation, the sample needs to be sonicated in ethanol for dispersion treatment. The H_2 temperature programmed reduction (H_2-TPR) experiments were conducted on a PCA-1200 (Builder, Beijing) instrument. Normally, 100 mg of the catalyst underwent pretreatment in a pure He atmosphere at 300 °C for 1.5 h, followed by cooling to room temperature. Subsequently, the sample was raised to 1000 °C in a 10% H_2/Ar atmosphere with a flow rate of 30 mL min^{-1} at a heating rate of 10 °C min^{-1}. The instrument used for temperature-programmed desorption of NH_3 (NH_3-TPD) is the same as that employed in the aforementioned catalytic activity tests, namely, the Antaris IGS gas analyzer. Prior to the NH_3-TPD

experiments, 100 mg catalyst was pretreated under N_2 protection (50 mL min^{-1}) at 300 °C for 1 h and then cooled to 30 °C. Then, the sample was exposed to 1000 ppm NH_3/N_2 (50 mL min^{-1}) for 1 h at 30 °C, the physical adsorption of ammonia was removed by N_2 purging for 1 h at the same temperature. Finally, the temperature was raised to 800 °C with a ramping rate of 2 °C min^{-1} in N_2 atmosphere (50 mL min^{-1}), and the desorbed NH_3 were detected by an Antaris IGS gas analyzer. The instrumentation and operational procedures employed for SO_2-TPD and NO-TPD characterizations were identical to those used for the aforementioned NH_3-TPD measurements. The sole difference was the replacement of the pre-adsorbed gas. The FTIR spectra that investigate the chemisorbed pyridine (Py-IR) were recorded on the FTIR spectrometer. Catalysts (20 mg) were pressed into a thin plate. The thin plates were heated to 350 °C for 1 h. Then, the cell was cooled to room temperature quickly by circulating water. The spectra measured at 260 °C were collected as references. When the temperature was cooled to 50 °C, the pyridine gas was filled into the cell for 30 min. The cell was pumped to vacuum for 1 h to remove the gaseous pyridine. Then, the cell was heated back to 260 °C and kept for 30 min. The FTIR spectra at this temperature are recorded. The *in situ* diffuse reflectance infrared Fourier transform spectroscopy (*in situ* DRIFTS) were acquired on an FTIR (Thermo Scientific Nicolet IS50) equipped with an MCT/A detector cooled by liquid nitrogen and an *in situ* DRIFTS reaction cell with ZnSe windows. Prior to each experiment, the sample was pretreated at 400 °C for 1.5 h with N_2 flow (50 mL min^{-1}). The reaction conditions were controlled as follows: 1000 ppm NH_3, 1000 ppm NO + 5 vol% O_2, N_2 balance with 50

mL min^{-1}. All spectra were recorded from 1000–4000 cm^{-1} in Kubelka-Munk format, accumulating 64 scans with a resolution of 4 cm^{-1}. X-ray absorption fine structure (XAFS) spectroscopy was carried out using the Rapid XAFS 2M (Anhui Absorption Spectroscopy Analysis Instrument Co., Ltd.) by transmission (or fluorescence) mode at 10 kV and 20 mA, and the Si (553) spherically bent crystal analyzer with a radius of curvature of 500 mm was used for Mn. X-ray absorption near-edge structure (XANES) and extended X-ray absorption fine structure (EXAFS) data reduction and analysis were processed by Athena and Artemis software. This instrument demonstrates its capability to provide precise structural parameters, including coordination environment and atomic distances. Prior to *in situ* EXAFS experiments, the catalyst was pretreated in O_2/N_2 at 400 °C for 30 min. After the sample cooled down to 246 °C under N_2 flow, 250 ppm SO_2 + 5 vol.% O_2 was introduced to the catalyst, and the spectra of the catalyst were collected before reaction and during the sulfation process. The total flow rate was 100 mL/min.

DFT calculation

In this study, Vienna Ab-initio Simulation Package (VASP) was adopted for the DFT calculation[3,4]. The projector augmented wave (PAW) method and the Perdew–Burke–Ernzerhof functional were used for calculation as exchange-correlation functional[5]. The cut-off energy was set to 500 eV, and for the strong electronic correlation of transition metals and their oxide systems, we used the DFT + U method to solve[6,7]. Hence, for the *d* orbitals of Mn, and Fe, a value of U = 4.5 and 4.0 eV was used[8,9],

respectively. For the $MnFeO_x$-ZSM-5 calculations, the energies are converged with (2 × 1 × 3) K points in a Monkhorst–Pack grid, (3 × 1 × 3) was adopted for $MnFeO_x$-Fe_2O_3. The lowest energy structure can be determined when the change in total energy and the force acting on each ion is less than 10^{-5} eV and 10^{-3} eV $Å^{-1}$, respectively. An at least 20 Å thick vacuum layer in the z–direction is added to simulate the surfaces to ensure the reaction will not be influenced by next layer.

The adsorption energies (E_{ads}) of reaction gas on the catalyst surface were calculated by using following formula:

$$E_{ads}=E_{gas\text{-}structure}-(E_{gas}+E_{structure}) \quad (6)$$

Where E_{ads}, $E_{structure}$ and E_{gas} is the total energy of adsorbed reaction gas over the catalyst surface, interacting catalyst surface, and the isolated gas molecules in vacuum, respectively. For $MnFeO_x$@YS-ZSM-5, $MnFeO_x$ composite metal oxide clusters are encapsulated on the (020) facets of ZSM-5 zeolite. As for $MnFeO_x$ structure, MnO_x species are loaded on the Fe_2O_3 (104) facets.

Supplementary Figures

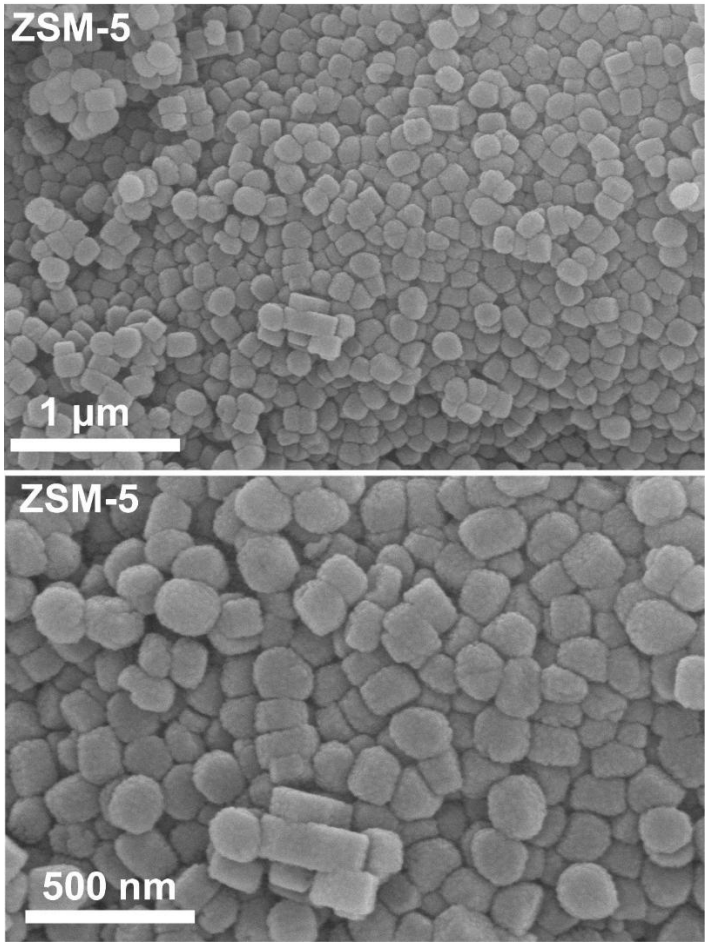

Figure S1. SEM images of the ZSM-5 zeolite.

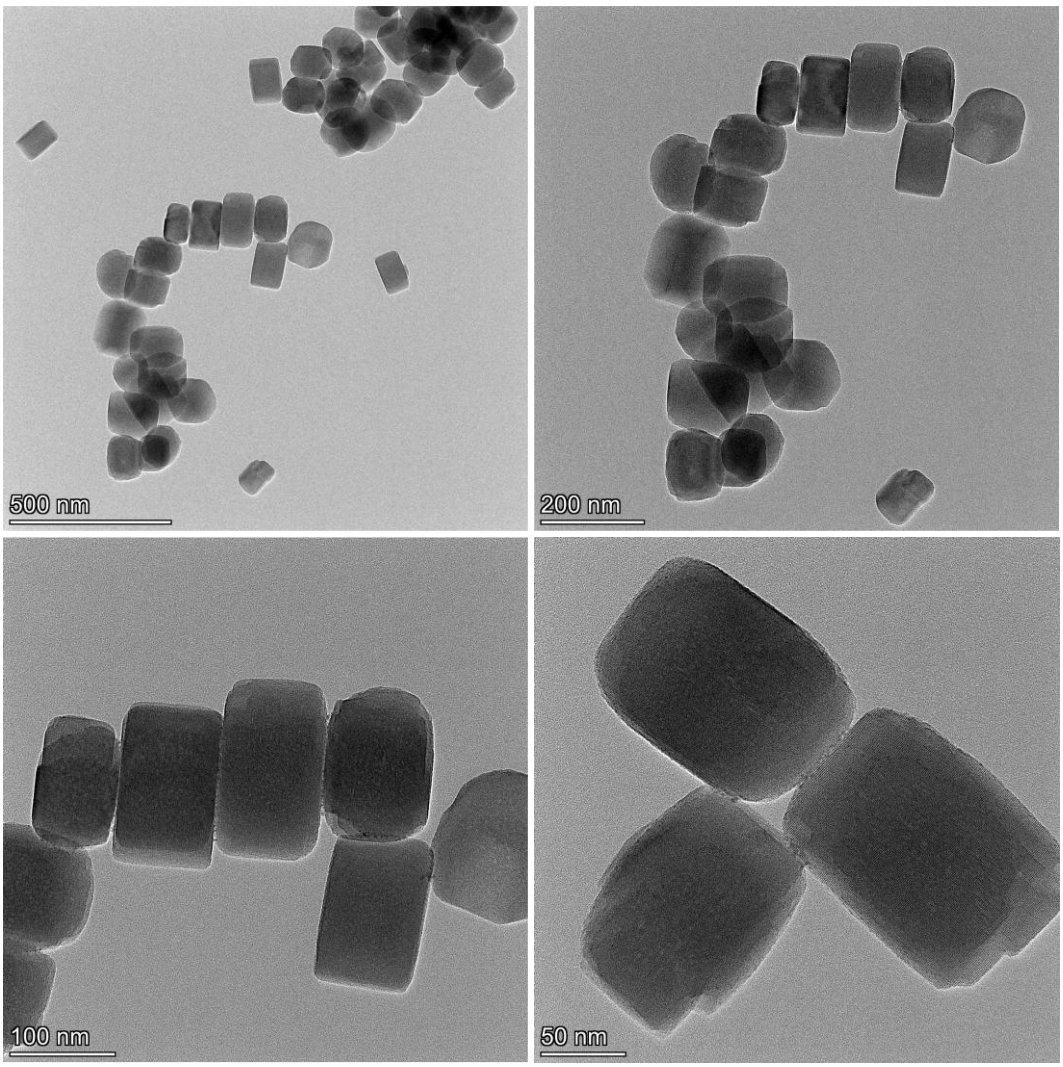

Figure S2. TEM images of the ZSM-5 zeolite.

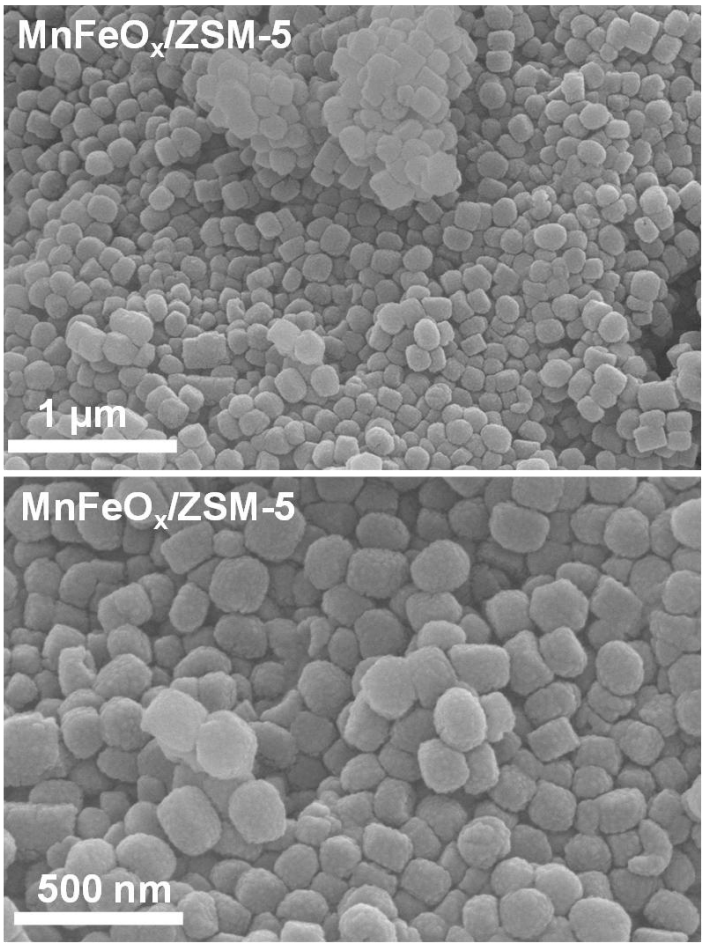

Figure S3. SEM images of the supported $MnFeO_x$/ZSM-5 sample.

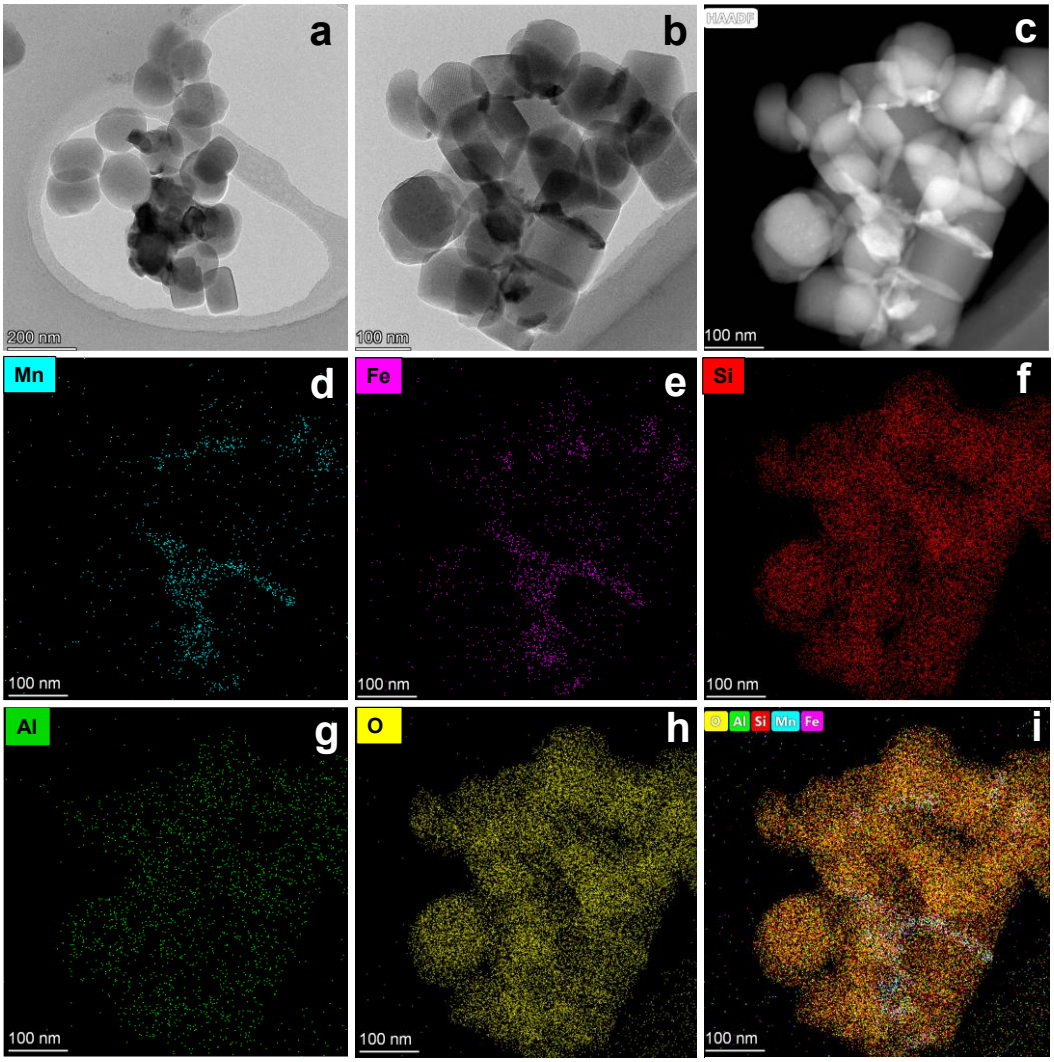

Figure S4. (a, b) TEM images, (c) HAADF-TEM image and (d–i) EDS elemental mappings of the supported $MnFeO_x$/ZSM-5 sample.

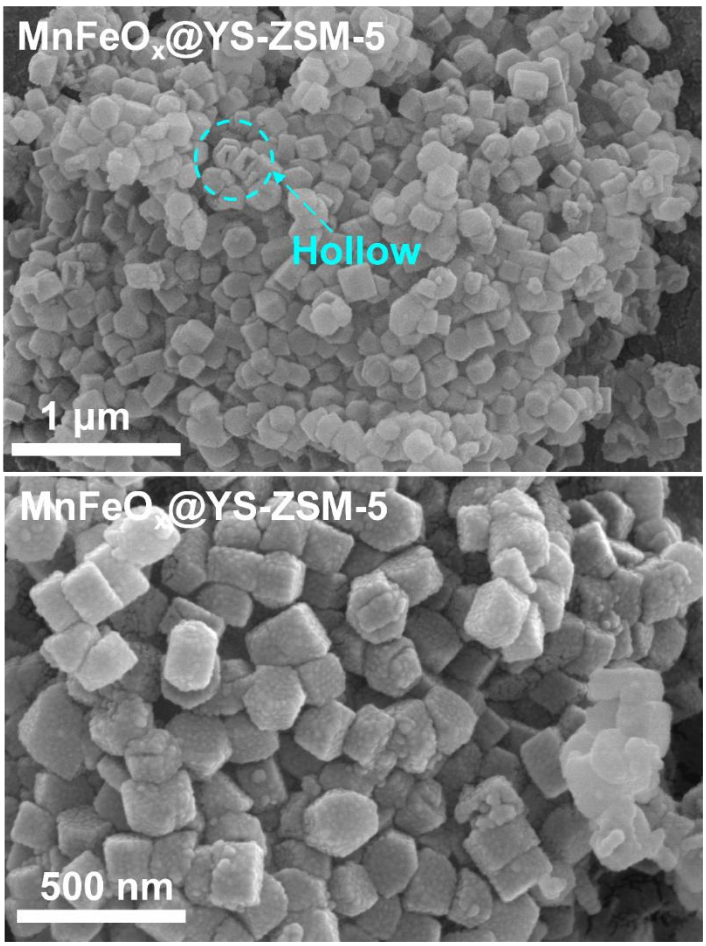

Figure S5. SEM images of the yolk-shell structured $MnFeO_x$@YS-ZSM-5 nanoreactor.

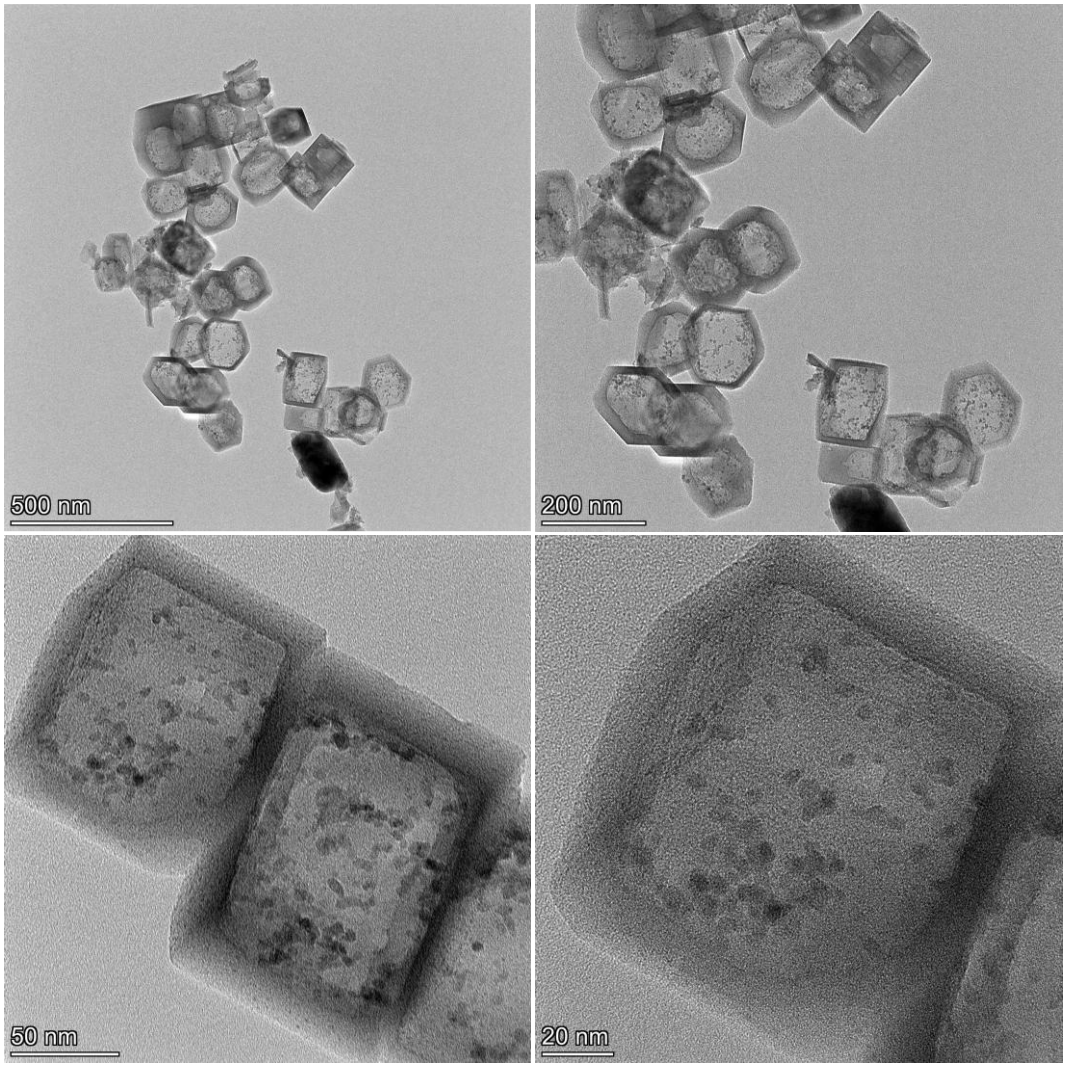

Figure S6. TEM images of the yolk-shell structured $MnFeO_x$@YS-ZSM-5 nanoreactor.

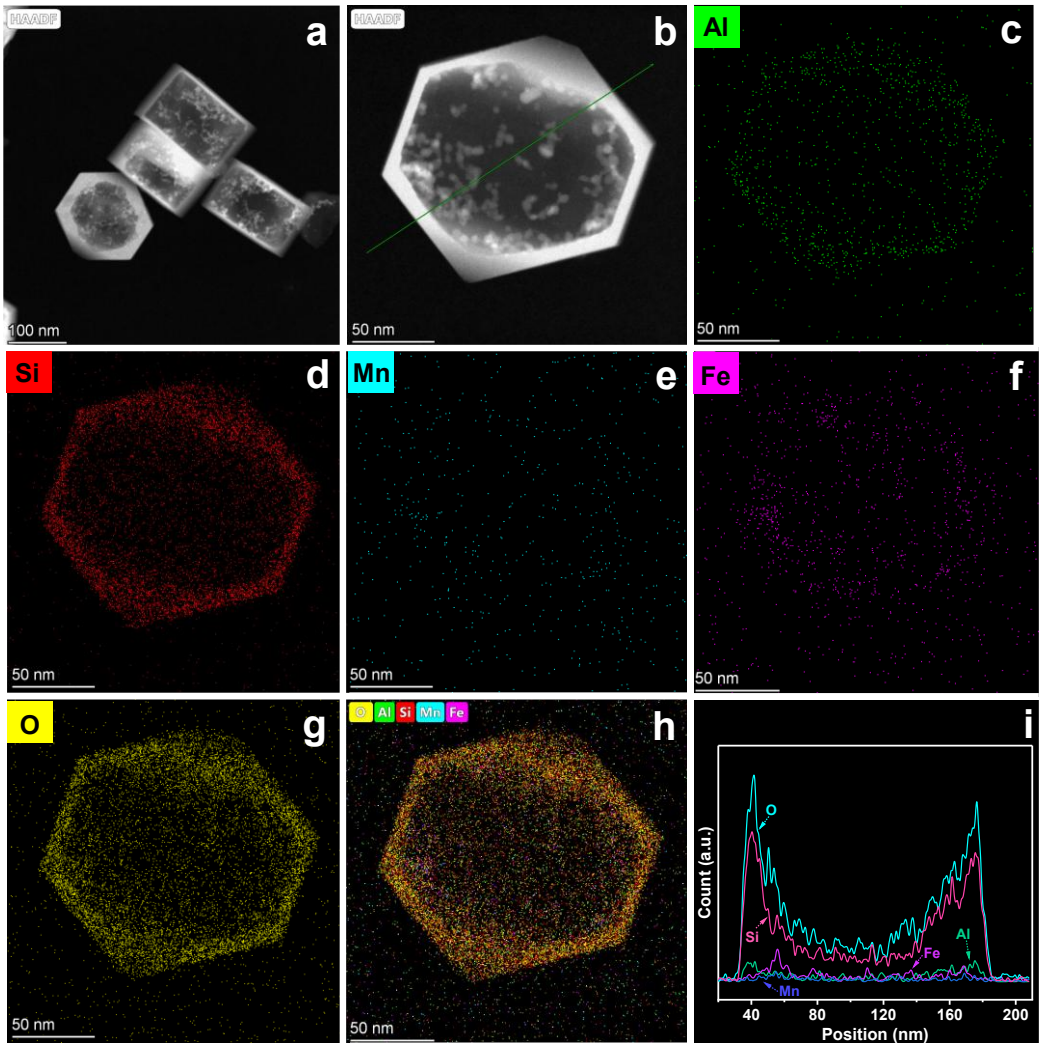

Figure S7. (a, b) HAADF-STEM, (c–h) EDS elemental mappings, and (i) line scan of the yolk-shell structured $MnFeO_x$@YS-ZSM-5 nanoreactor.

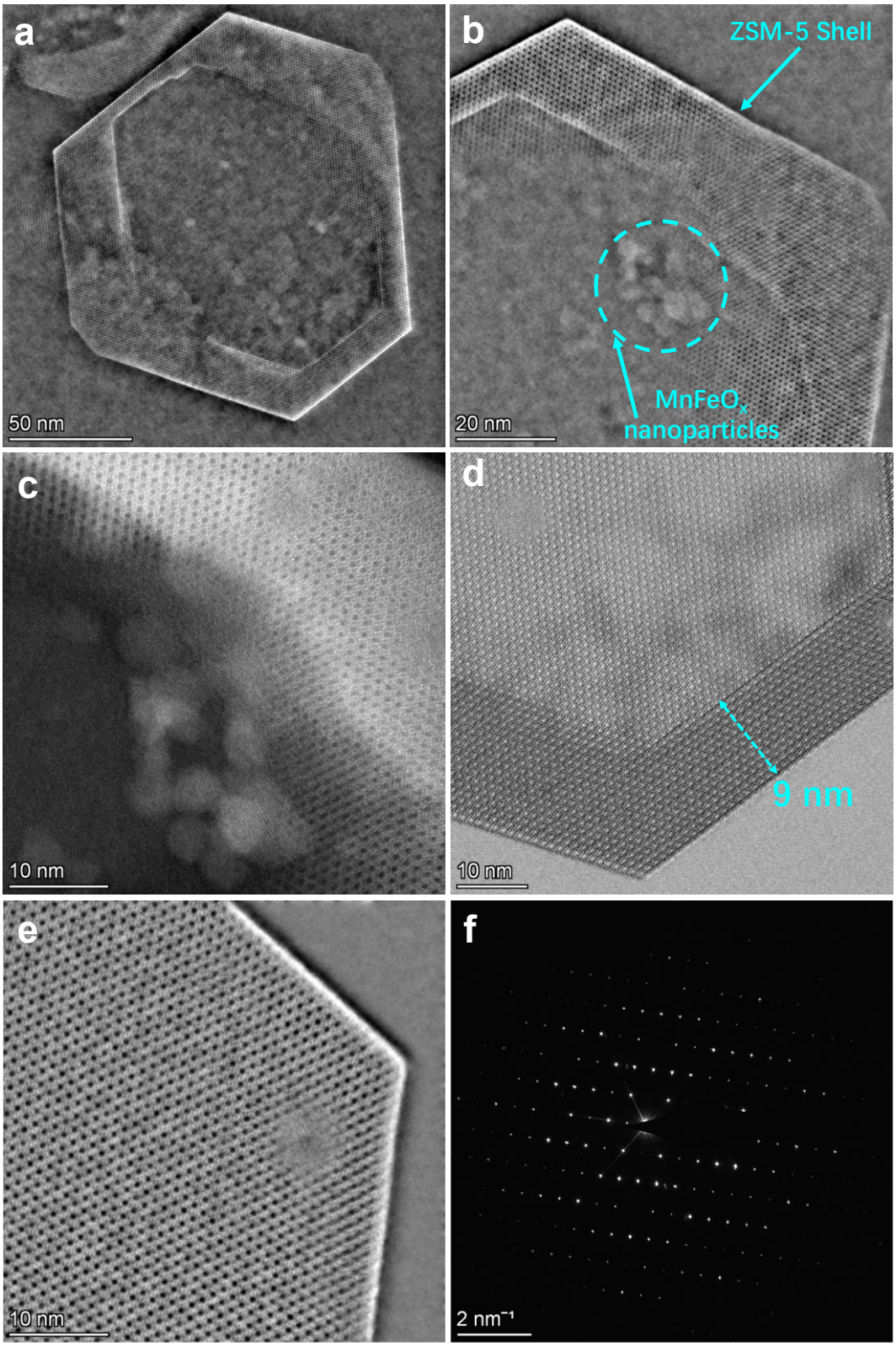

Figure S8. (a–e) IDPC-STEM images and (f) selected area electron diffraction (SAED) of the yolk-shell structured $MnFeO_x$@YS-ZSM-5 nanoreactor.

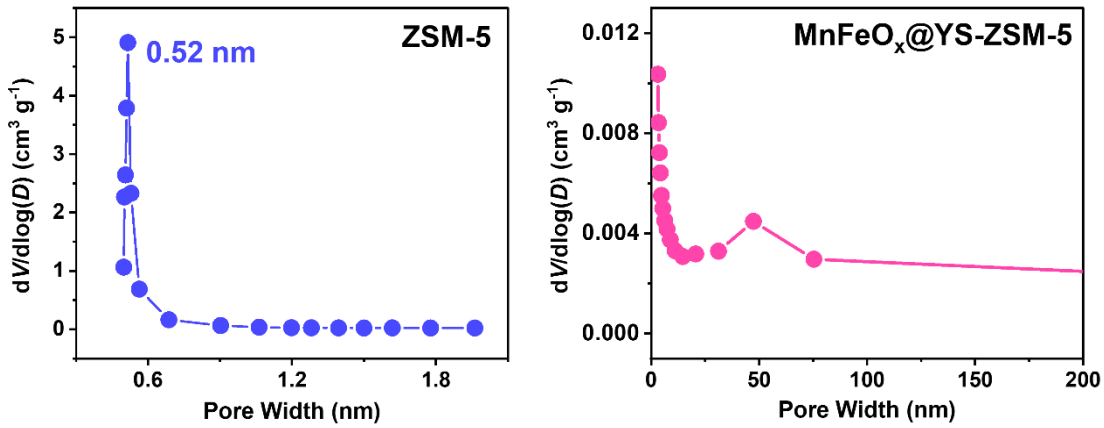

Figure S9. Pore-size distributions of ZSM-5 zeolite and yolk-shell structured $MnFeO_x$@YS-ZSM-5 samples derived from the isotherms.

Note: The pore-size distribution curves confirm the development of a large cavity inside the zeolite framework of $MnFeO_x$@YS-ZSM-5 nanoreactor.

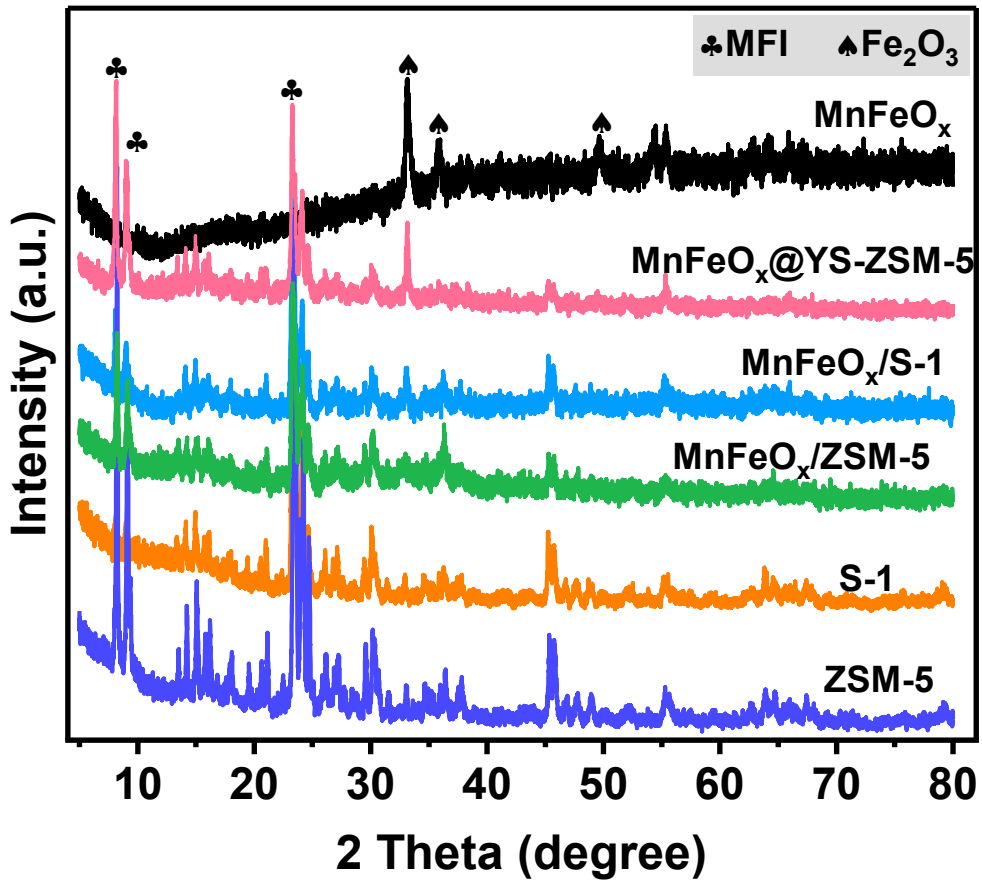

Figure S10. Powder XRD patterns of as-prepared ZSM-5, S-1, $MnFeO_x$, $MnFeO_x$/ZSM-5, $MnFeO_x$/S-1, and $MnFeO_x$@YS-ZSM-5 samples.

Note: XRD patterns show that both $MnFeO_x$/ZSM-5 and $MnFeO_x$@YS-ZSM-5 exhibit characteristic reflections, consistent with the MFI topology of ZSM-5 zeolite (JCPDS 44-0003). These above results confirm that the zeolite framework remains intact after $MnFeO_x$ encapsulation.

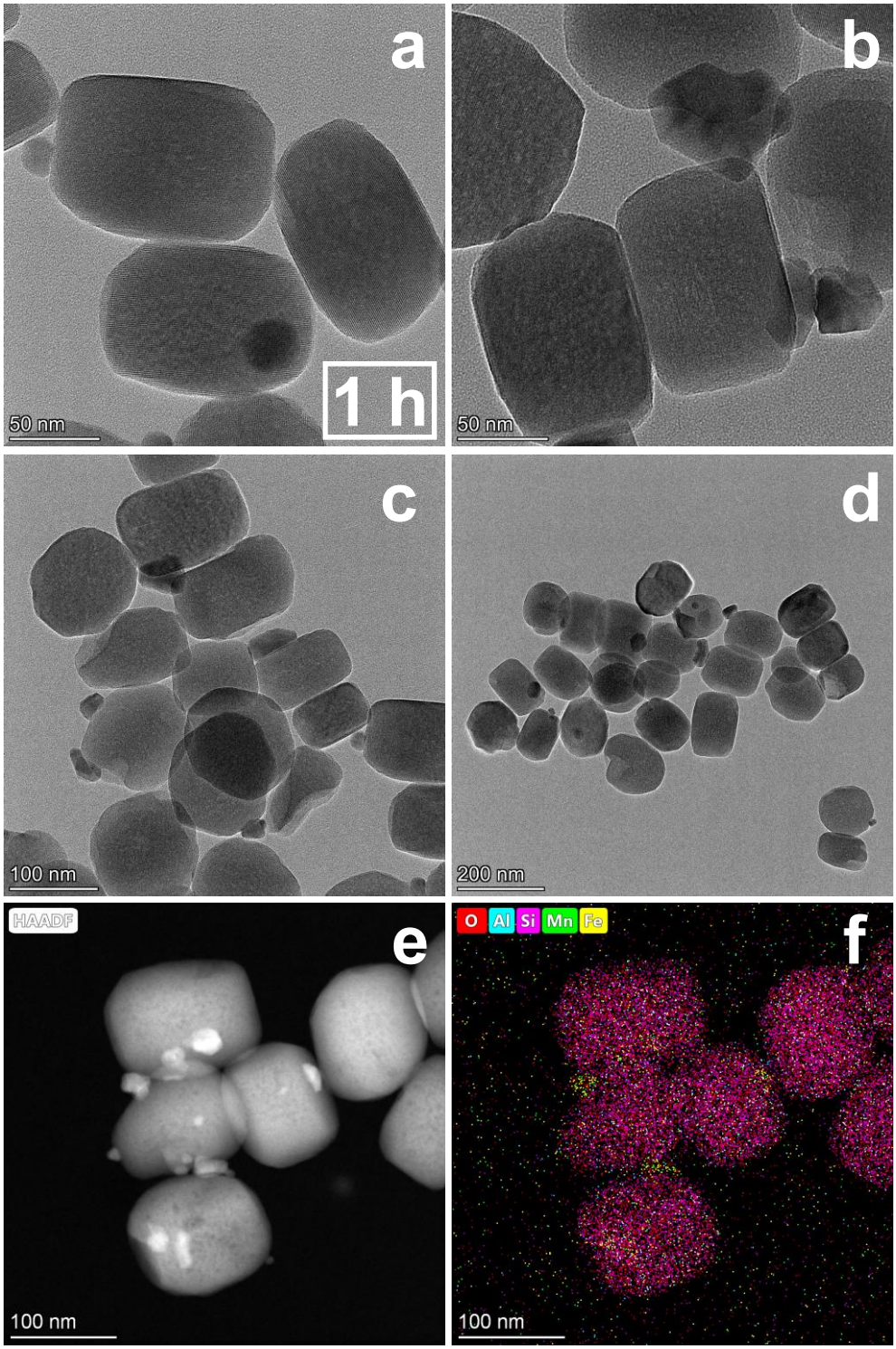

Figure S11. (a–d) TEM, (e) HAADF-STEM, and (f) EDS elemental mappings of $MnFeO_x$@YS-ZSM-5 sample obtained after being hydrothermally treated in TPAOH solution at 170 °C for 1 h.

Note: After 1 h of hydrothermal treatment, no visible changes are observed.

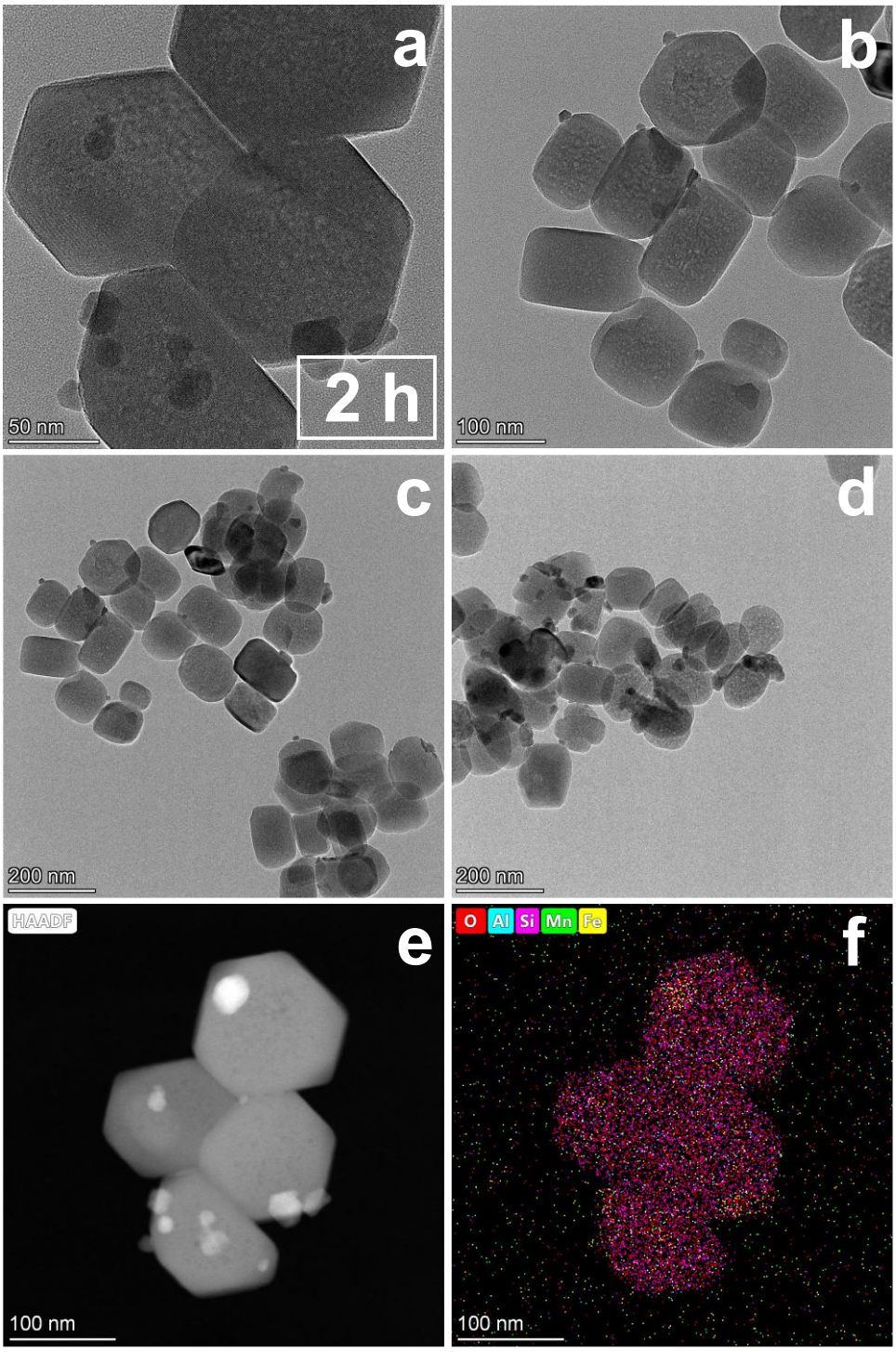

Figure S12. (a–d) TEM, (e) HAADF-STEM, and (f) EDS elemental mappings of the $MnFeO_x$@YS-ZSM-5 sample obtained after being hydrothermally treated in TPAOH solution at 170 °C for 2 h.

Note: After 2 h, small internal voids appeared at the center of the zeolite, indicating that dissolution initially occurs in the particle interior.

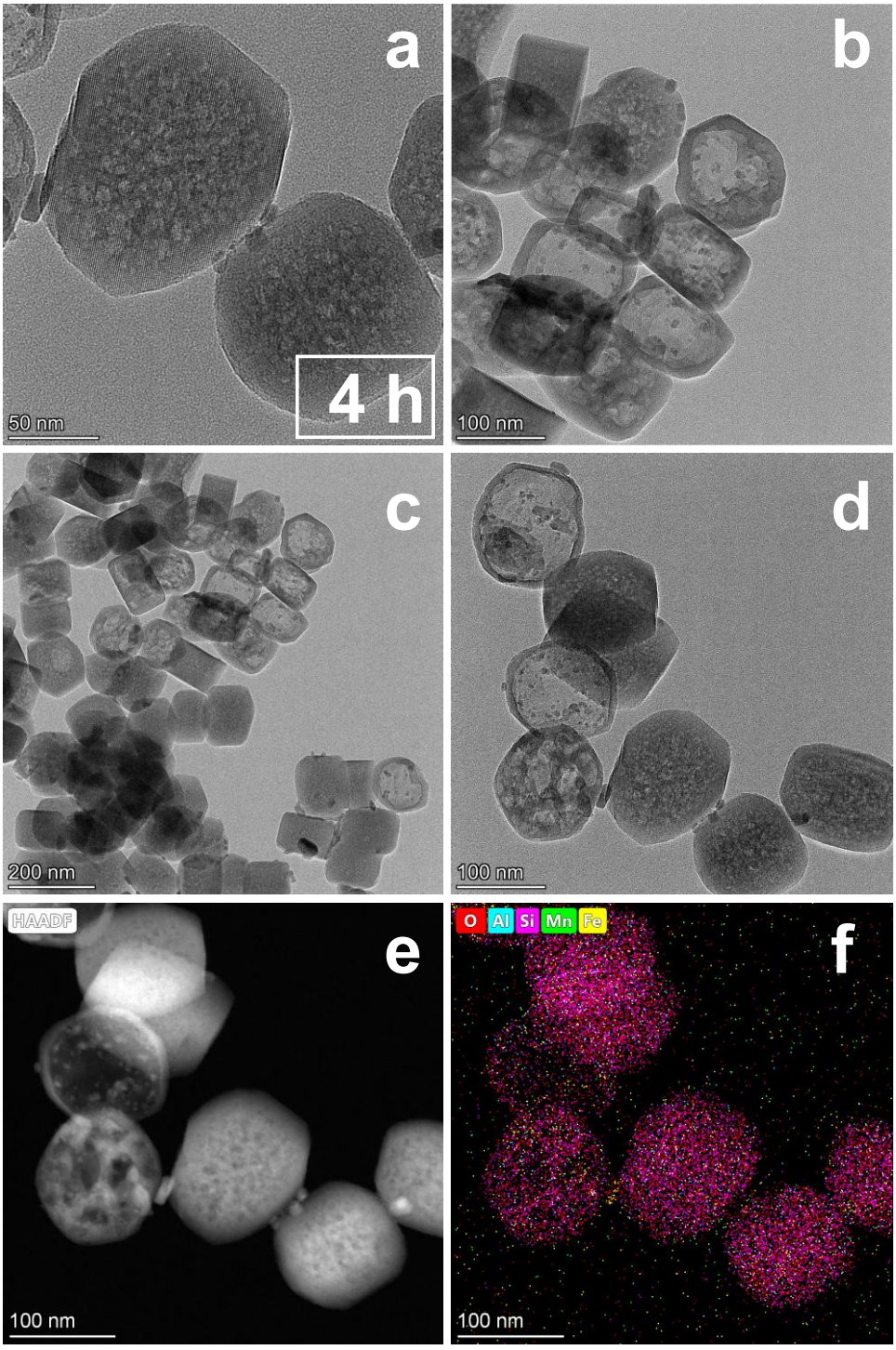

Figure S13. (a–d) TEM, (e) HAADF-STEM, and (f) EDS elemental mappings of the $MnFeO_x$@YS-ZSM-5 sample obtained after being hydrothermally treated in TPAOH solution at 170 °C for 4 h.

Note: At 4 h, voids expanded into vesicle-like cavities, while others remained small.

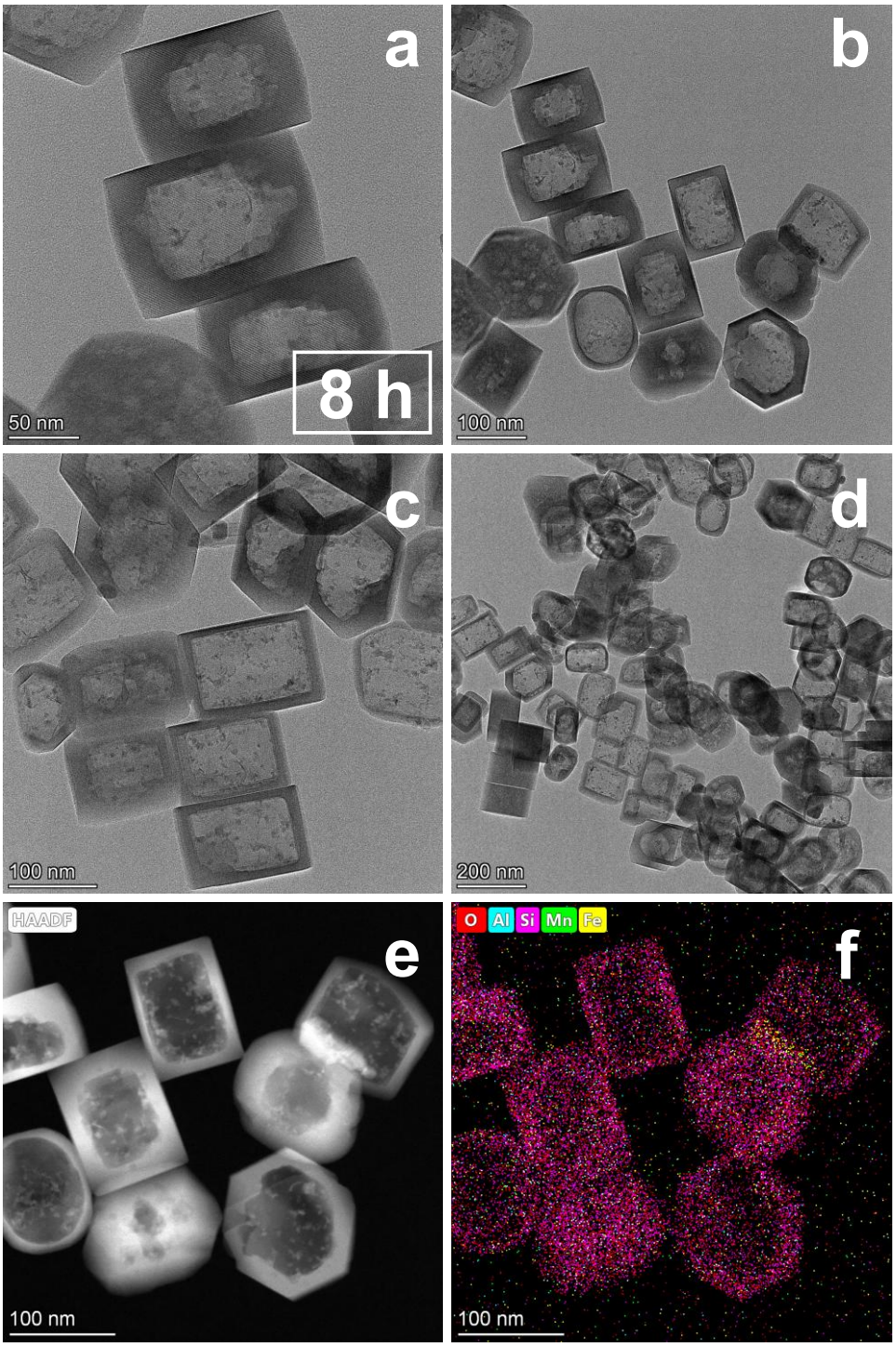

Figure S14. (a–d) TEM, (e) HAADF-STEM, and (f) EDS elemental mappings of the $MnFeO_x$@YS-ZSM-5 sample obtained after being hydrothermally treated in TPAOH solution at 170 °C for 8 h.

Note: After 8 h, a higher proportion of particles developed to form yolk-shell structures, though some retained solid interiors.

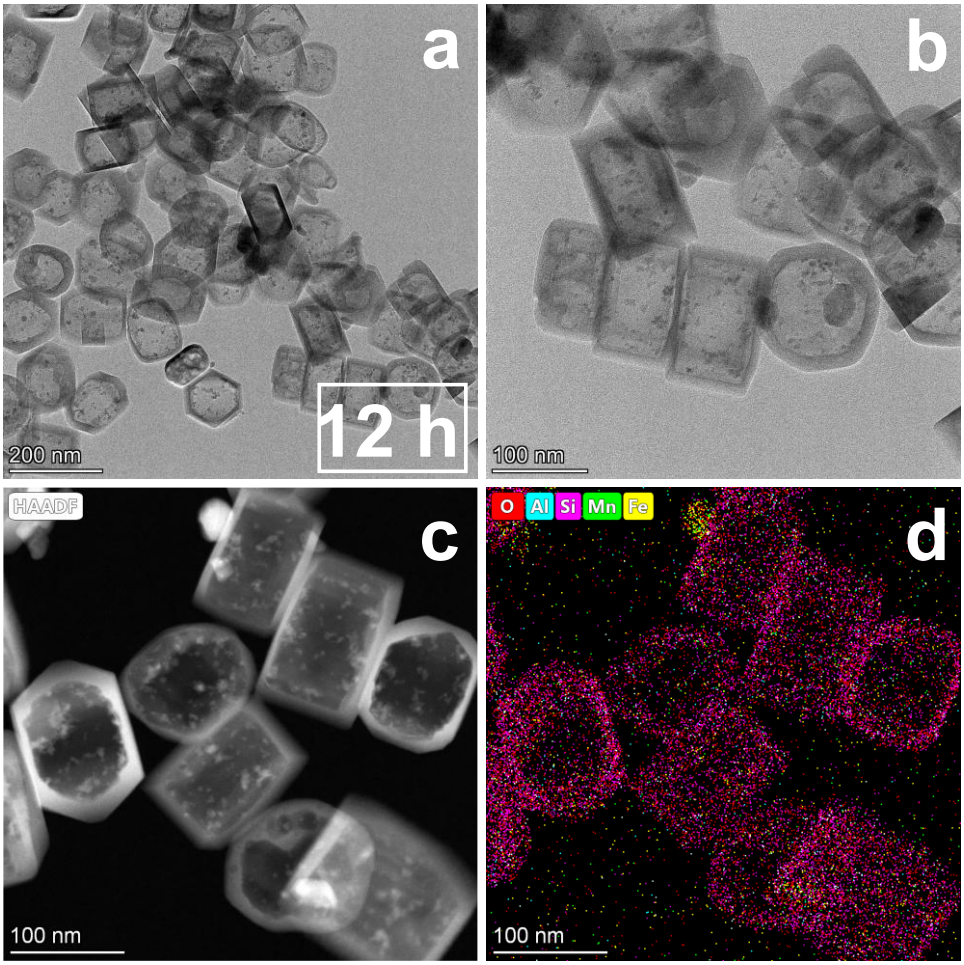

Figure S15. (a, b) TEM, (c) HAADF-STEM, and (d) EDS elemental mappings of the $MnFeO_x$@YS-ZSM-5 sample obtained after being hydrothermally treated in TPAOH solution at 170 °C for 12 h.

Note: With prolonged hydrothermal treatment for 12 h, an increasingly larger fraction of particles exhibited well-defined hollow interiors.

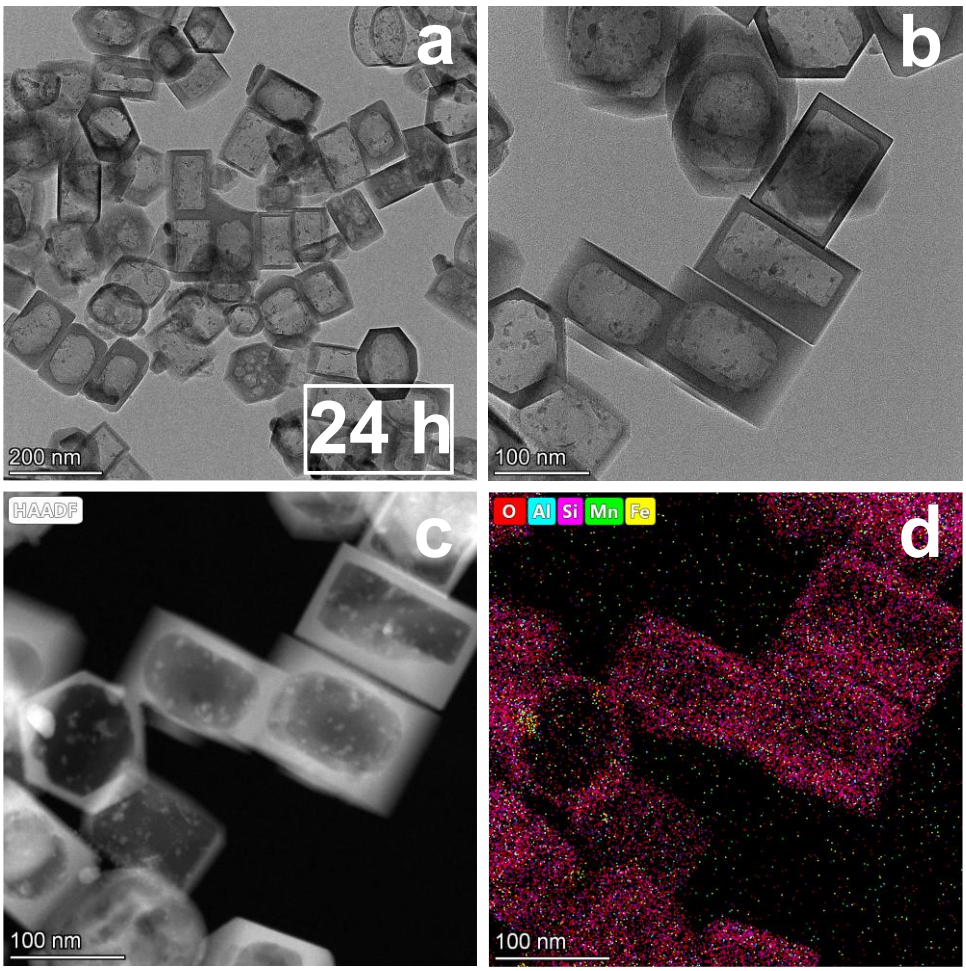

Figure S16. (a, b) TEM, (c) HAADF-STEM, and (d) EDS elemental mappings of the $MnFeO_x$@YS-ZSM-5 sample obtained after being hydrothermally treated in TPAOH solution at 170 °C for 24 h.

Note: With prolonged hydrothermal treatment for 24 h, an increasingly larger fraction of particles exhibited well-defined hollow interiors.

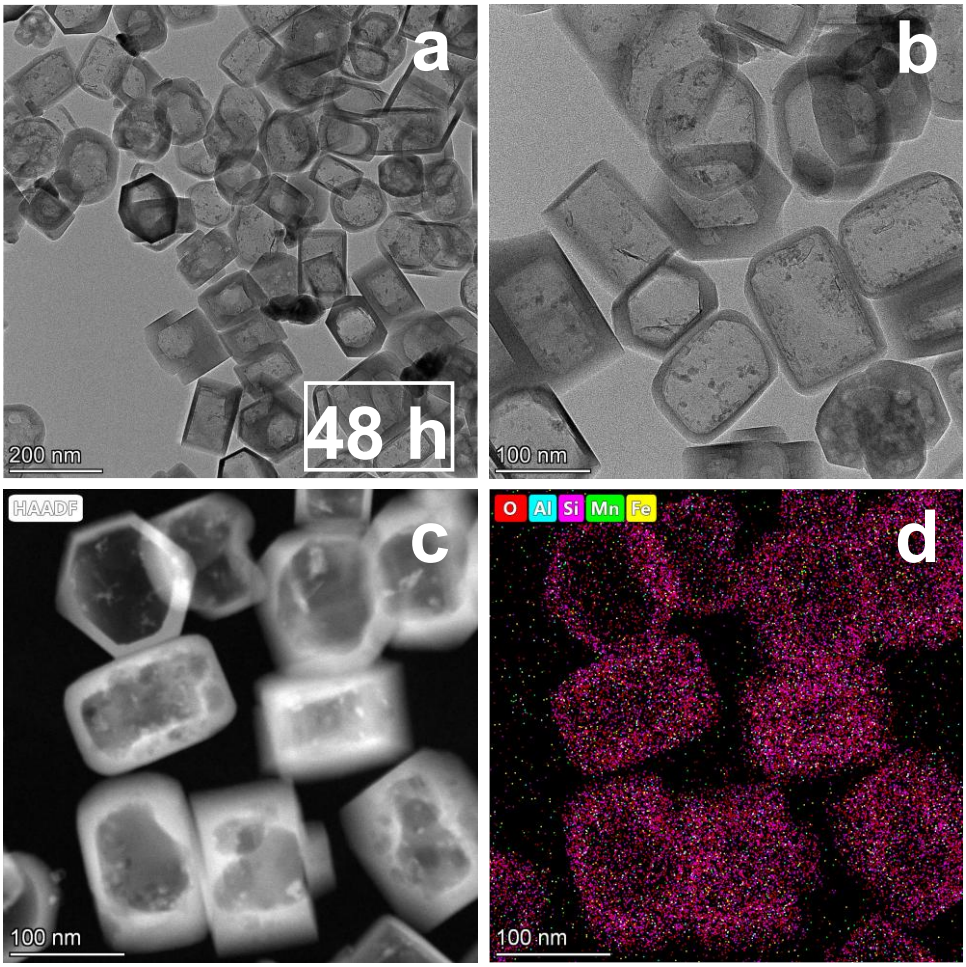

Figure S17. (a, b) TEM, (c) HAADF-STEM, and (d) EDS elemental mappings of the $MnFeO_x$@YS-ZSM-5 sample obtained after being hydrothermally treated in TPAOH solution at 170 °C for 48 h.

Note: With prolonged hydrothermal treatment for 48 h, an increasingly larger fraction of particles exhibited well-defined hollow interiors.

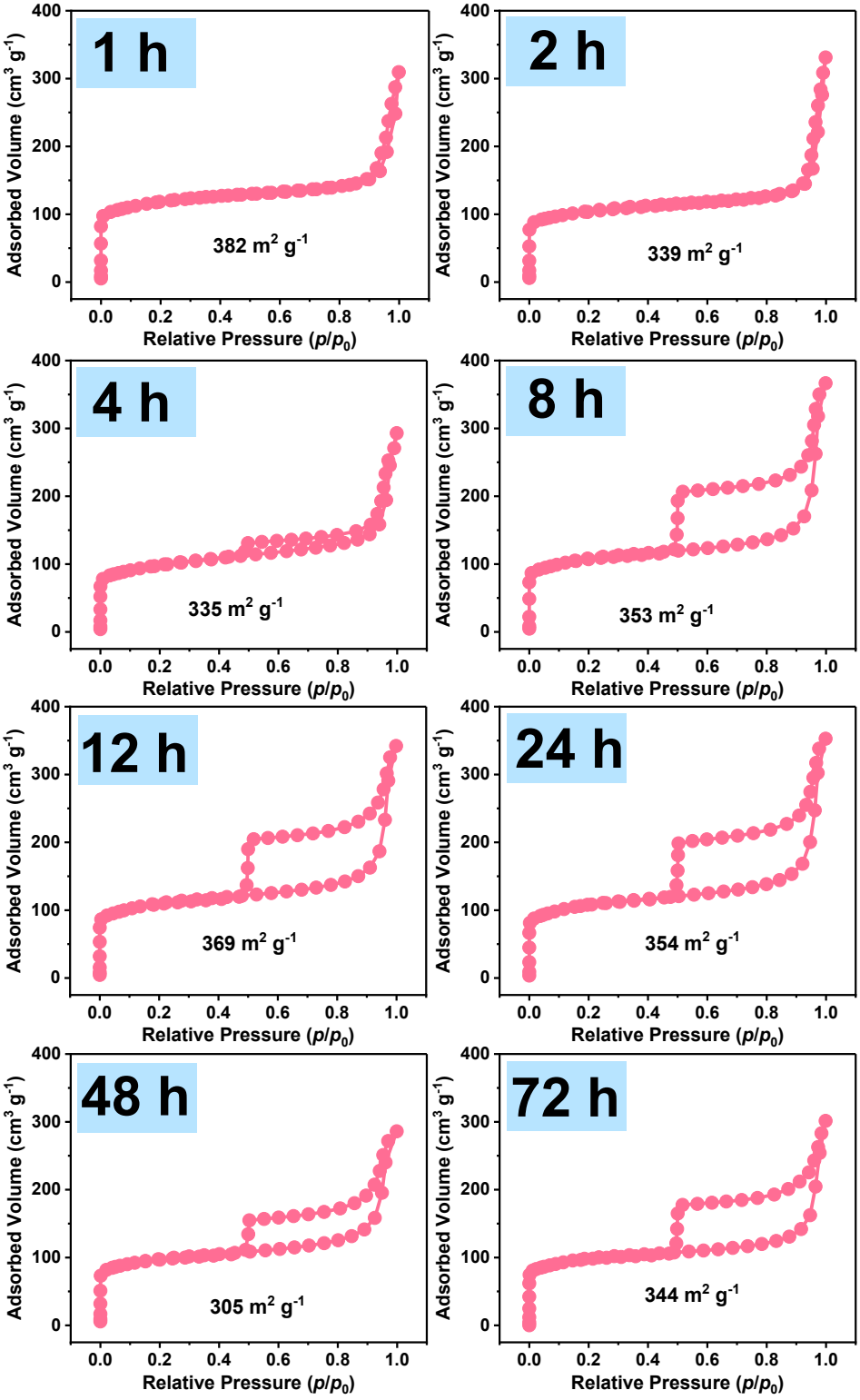

Figure S18. N_2 adsorption-desorption isotherms of $MnFeO_x$@YS-ZSM-5 obtained after being hydrothermally treated in TPAOH solution at 170 °C with varying durations.

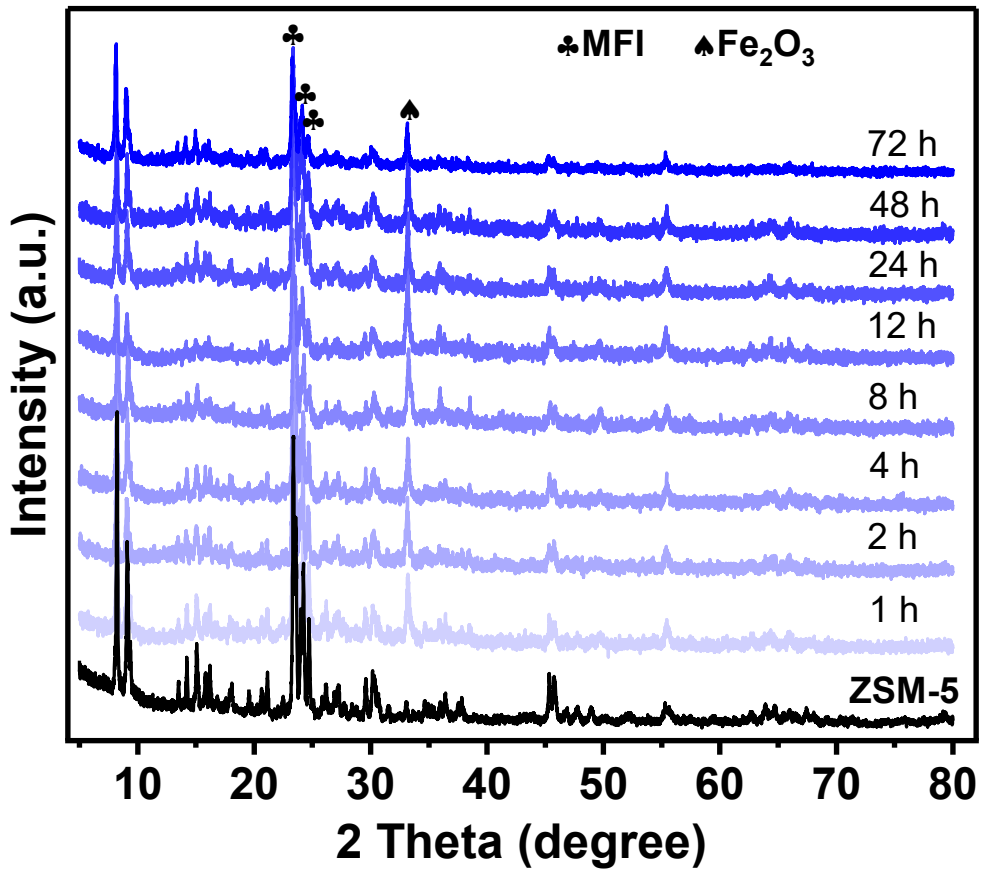

Figure S19. Powder XRD patterns of $MnFeO_x$@YS-ZSM-5 obtained after being hydrothermally treated in TPAOH solution at 170 °C with varying durations.

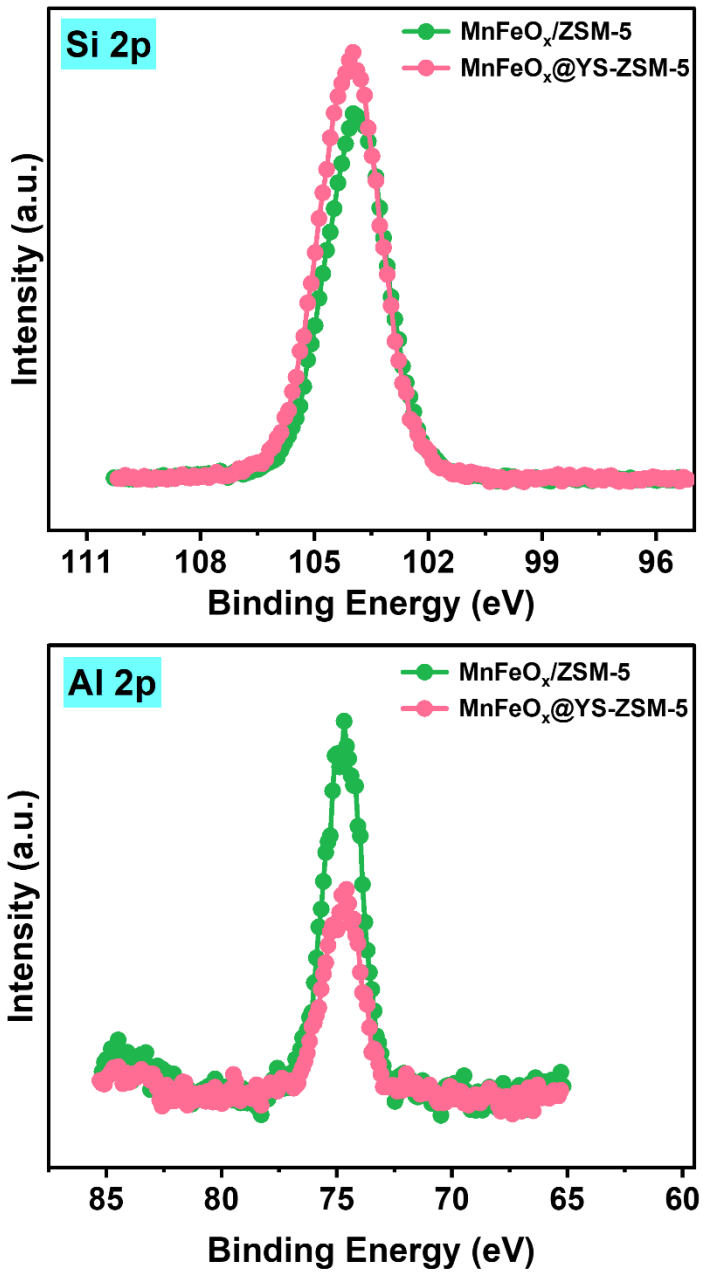

Figure S20. Si 2p and Al 2p XPS spectra of the supported $MnFeO_x$/ZSM-5 and yolk-shell structured $MnFeO_x$@YS-ZSM-5 samples.

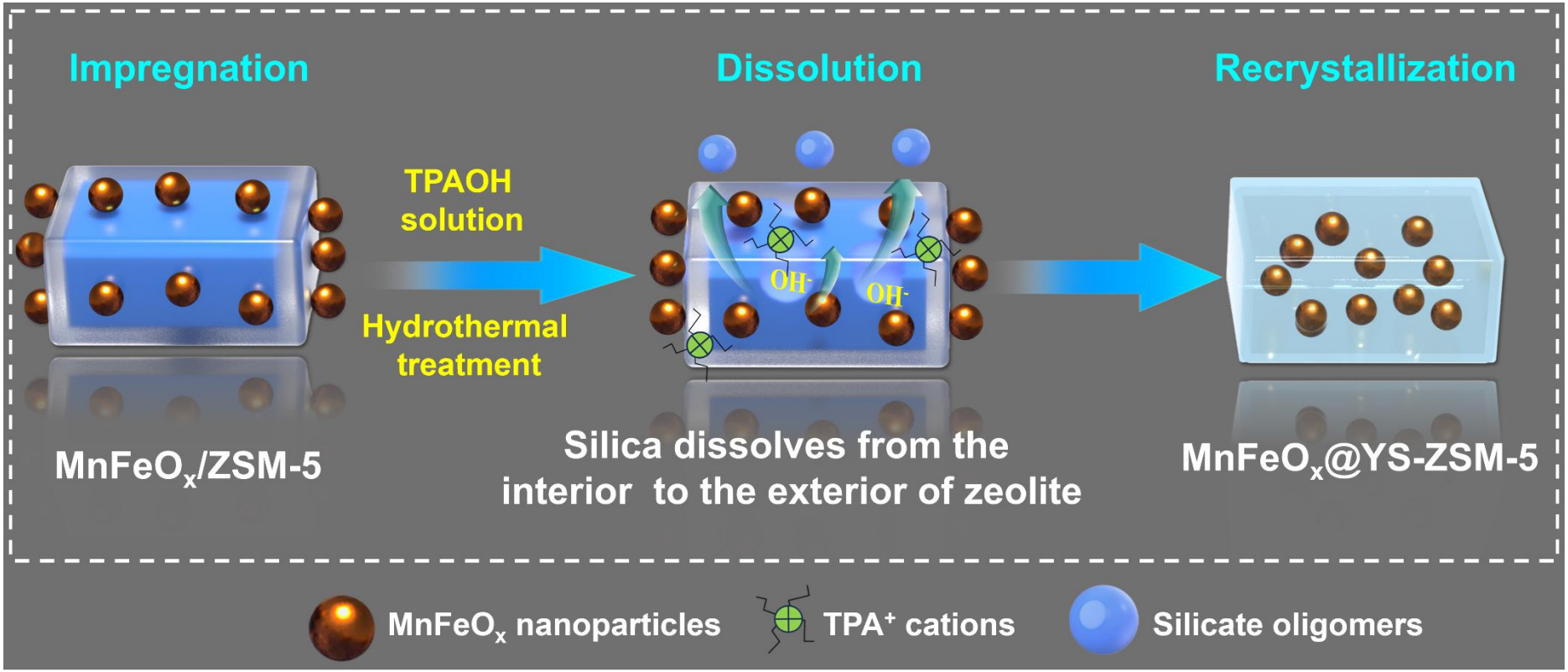

Figure S21. Formation mechanism of the yolk-shell structured $MnFeO_x$@YS-ZSM-5 nanoreactor.

Note: Pristine ZSM-5 single crystals typically exhibit a compositional gradient: Si is enriched in the interior, while Al is concentrated at the external surface. In $MnFeO_x$/ZSM-5, framework Al species exert a shielding effect on adjacent Si-O bonds, making neighboring Si-O moieties

less susceptible to alkaline etching. In addition, the internal region of the zeolite exhibits relatively lower crystallinity compared to the external surface, predisposing the particle interior to preferential dissolution. During alkaline treatment, hydroxide (OH^-) anions penetrate the micropores and diffuse into the interior of $MnFeO_x$/ZSM-5, promoting dissolution of silicon species. This dissolution progresses from the inside toward the outside. In contrast, the sterically bulky tetrapropylammonium (TPA^+) cations cannot pass through the microporous channels and instead adsorb on the external surface of the zeolite via electrostatic interactions. The dissolved silicate oligomers subsequently interact with surface-adsorbed TPA^+ and recrystallize outwardly. Through this coupled dissolution-recrystallization process, the zeolite interior undergoes selective etching, and the encapsulated $MnFeO_x$ nanoparticles become surrounded by newly crystallized zeolite layers. The metal oxide nanoparticles are in situ wrapped in the hollow zeolite cavity, resulting in Si enrichment and Al depletion on the external surface compared to the parent ZSM-5 zeolite.

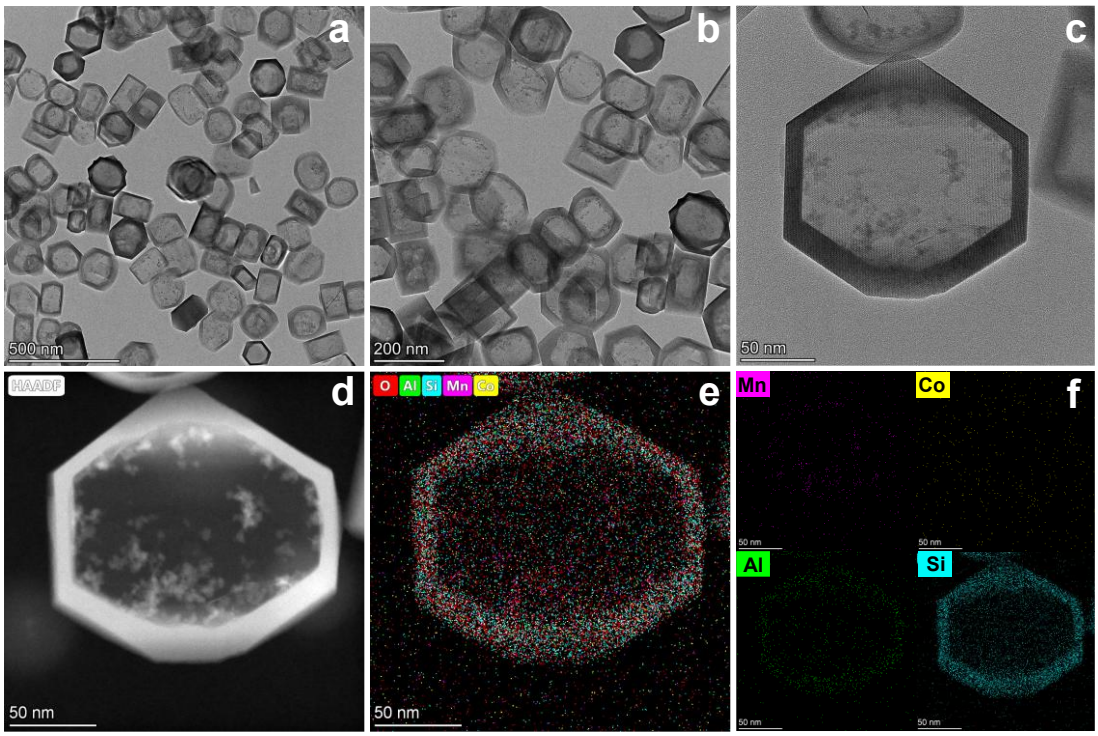

Figure S22. (a–c) TEM images, (d) HAADF-STEM, and (e, f) EDS elemental mappings of the yolk-shell structured $MnCoO_x$@YS-ZSM-5 nanoreactor.

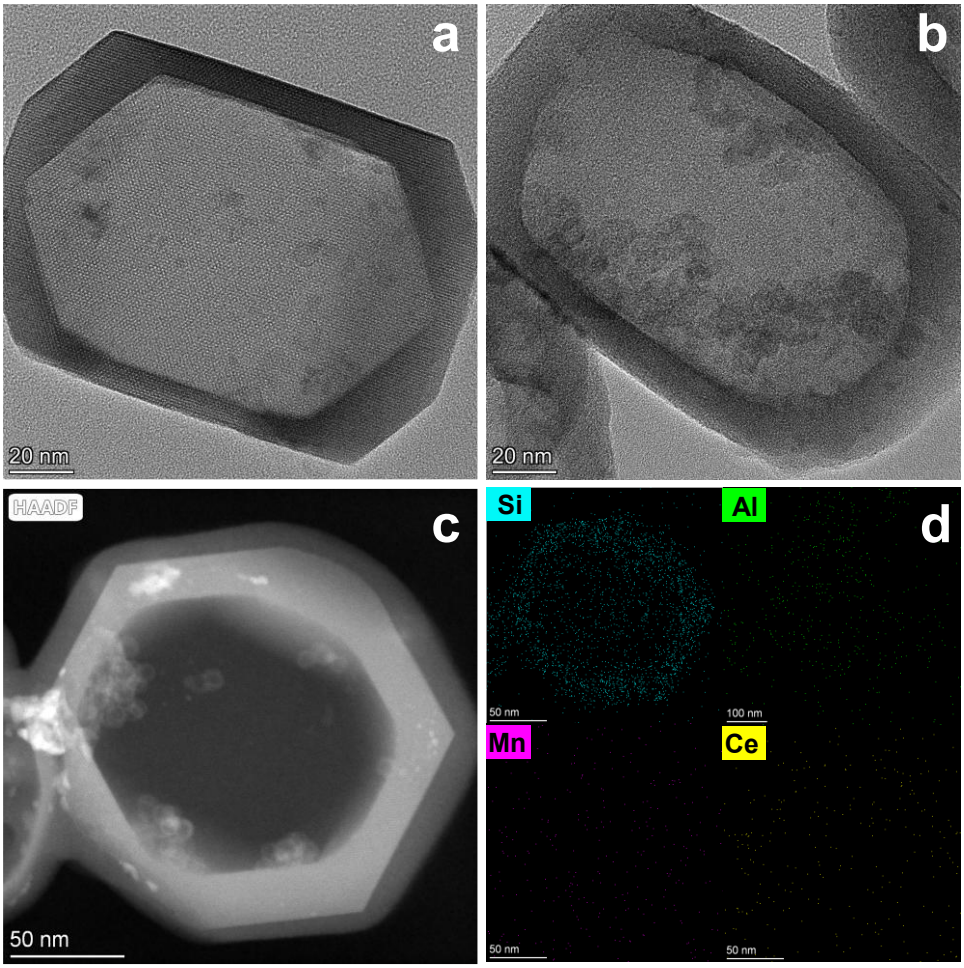

Figure S23. (a, b) TEM images, (c) HAADF-STEM, and (d) EDS elemental mappings of the yolk-shell structured $MnCeO_x$@YS-ZSM-5 nanoreactor.

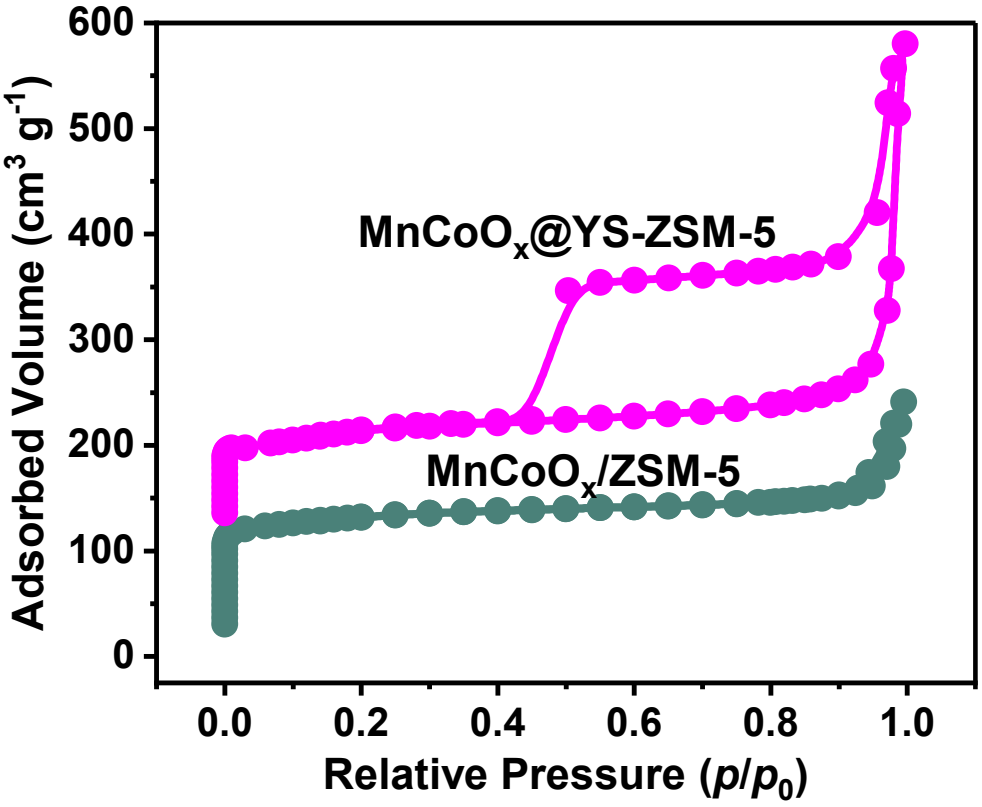

Figure S24. N_2 adsorption-desorption isotherms of supported $MnCoO_x$/ZSM-5 and yolk-shell structured $MnCoO_x$@YS-ZSM-5 nanoreactor.

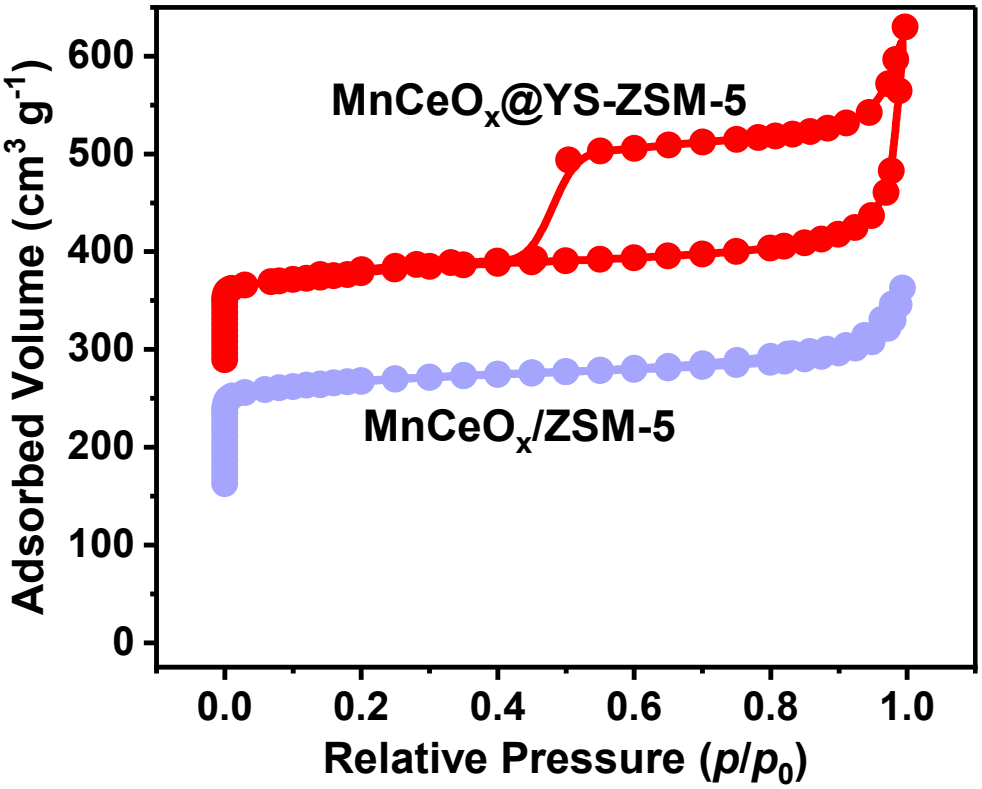

Figure S25. N_2 adsorption-desorption isotherms of supported $MnCeO_x$/ZSM-5 and yolk-shell structured $MnCeO_x$@YS-ZSM-5 nanoreactor.

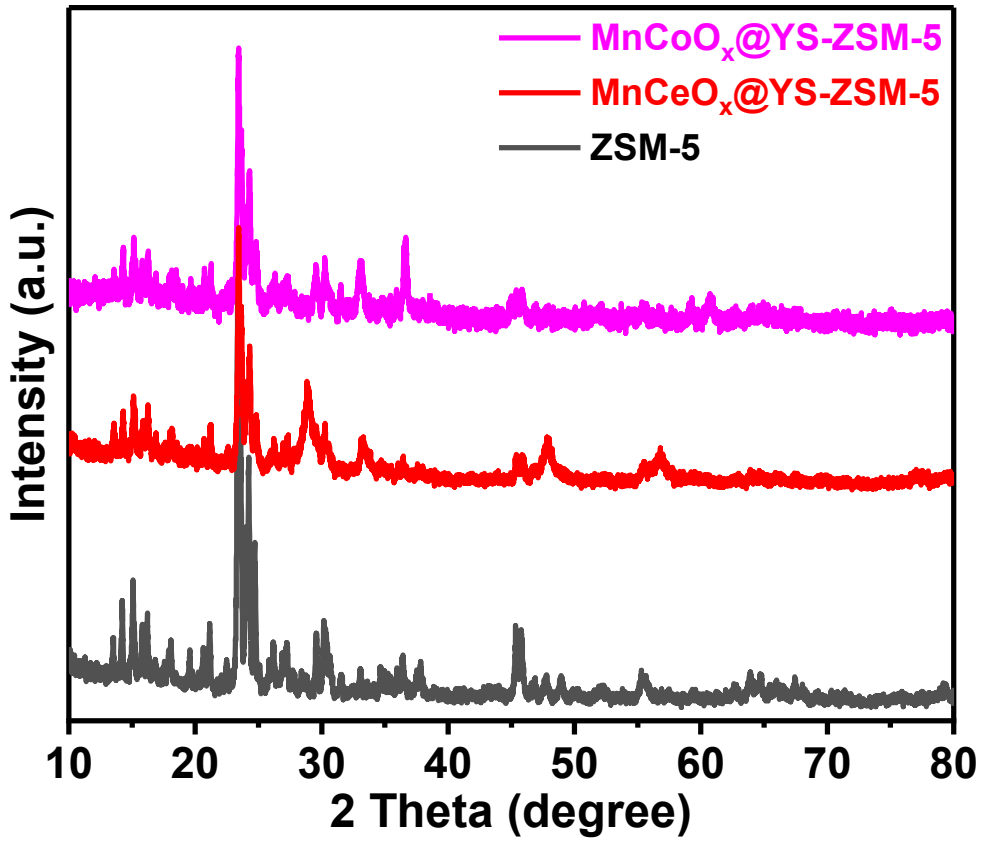

Figure S26. Powder XRD patterns of yolk-shell structured $MnCoO_x$@YS-ZSM-5 and $MnCeO_x$@ZSM-5 nanoreactors.

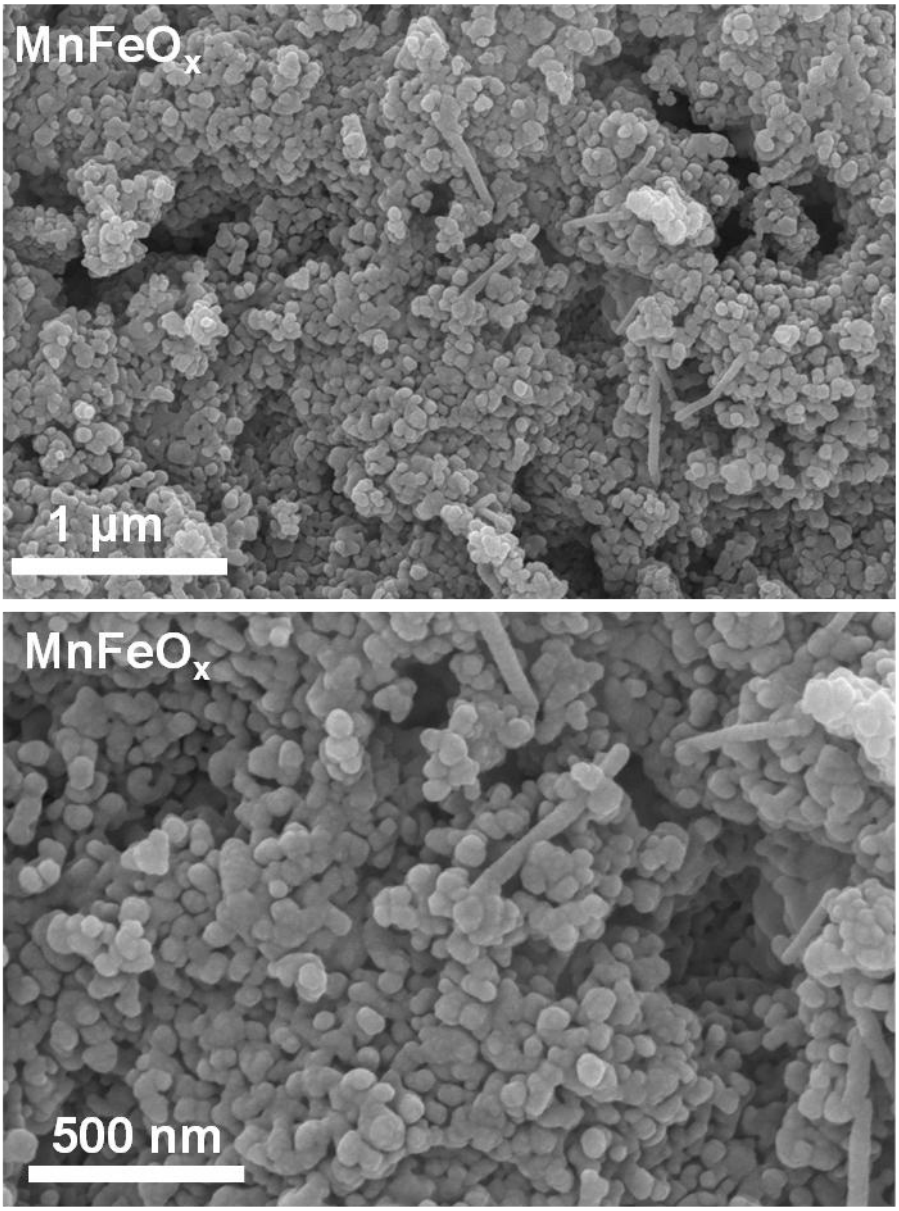

Figure S27. SEM images of the pure $MnFeO_x$ metal oxides sample.

Note: Pure $MnFeO_x$ sample prepared via the co-precipitation method is composed of stacked nanoparticles.

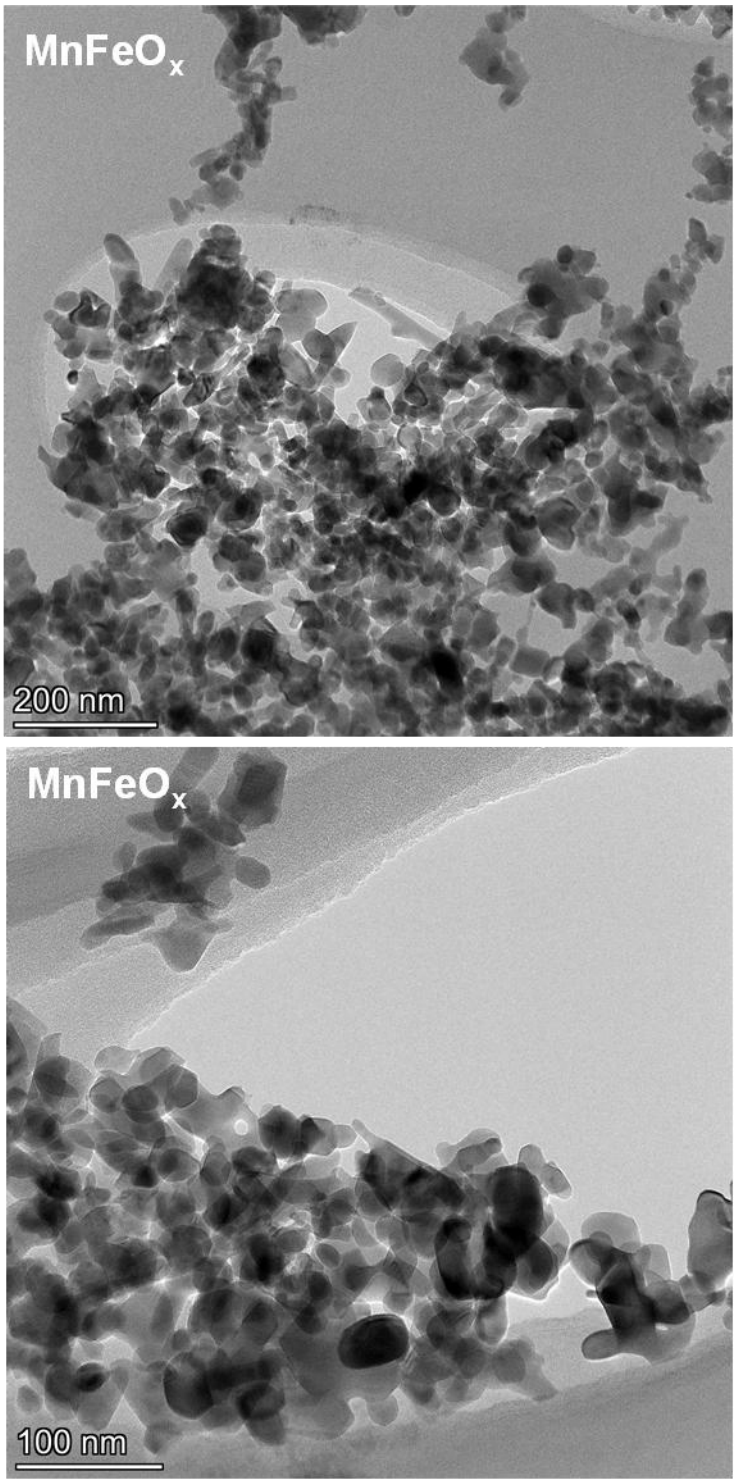

Figure S28. TEM images of the pure $MnFeO_x$ metal oxides sample.

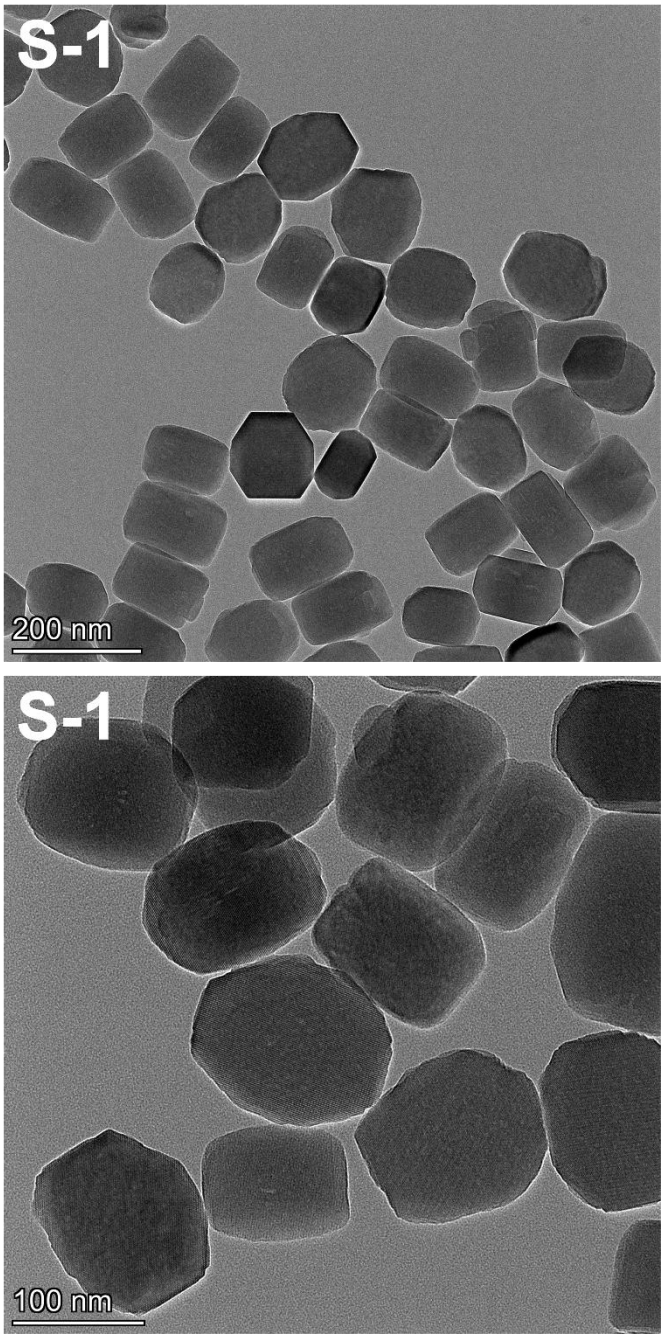

Figure S29. TEM images of the S-1 zeolite.

Note: S-1 zeolite exhibits a morphology similar to ZSM-5, with a clean surface and a primarily rod-shaped structure.

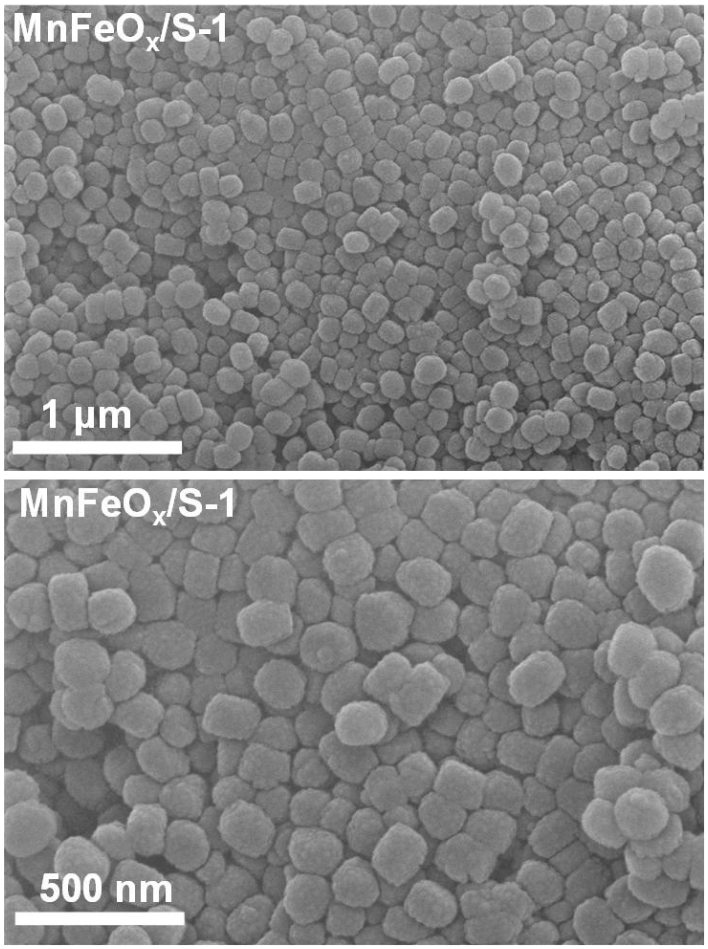

Figure S30. TEM images of the supported $MnFeO_x$/S-1 sample.

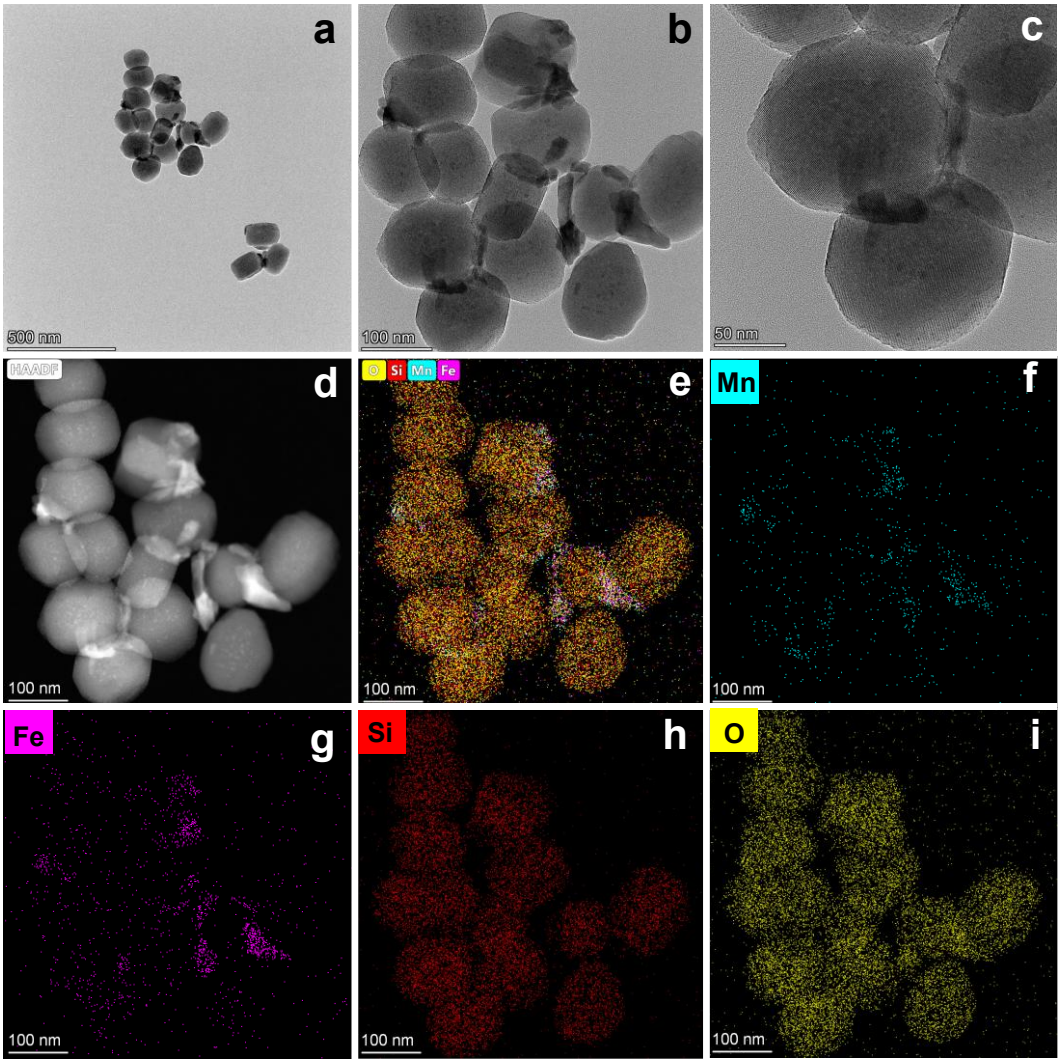

Figure S31. (a–c) TEM images, (d) HAADF-STEM, and (e–i) EDS elemental mappings of the supported $MnFeO_x$/S-1 sample.

Note: In the $MnFeO_x$/S-1 catalyst, $MnFeO_x$ metal oxides aggregates are observed stacked on the surface of the S-1 support.

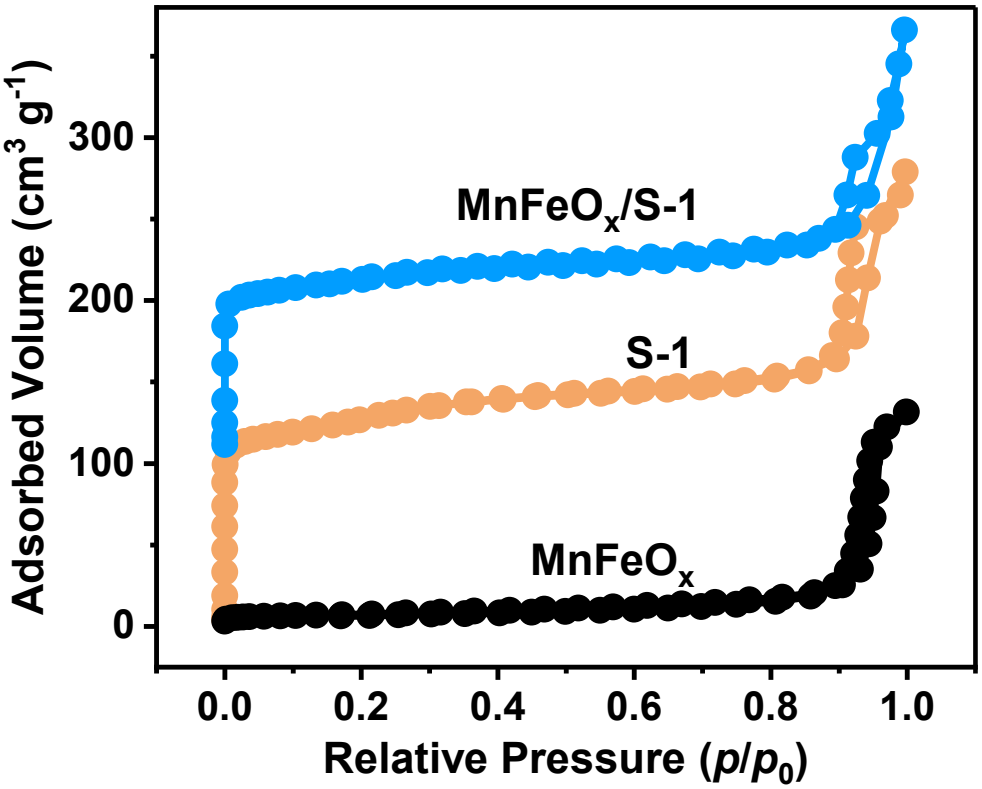

Figure S32. N_2 adsorption-desorption isotherms of the pure $MnFeO_x$, S-1 zeolite, and supported $MnFeO_x$/S-1 samples.

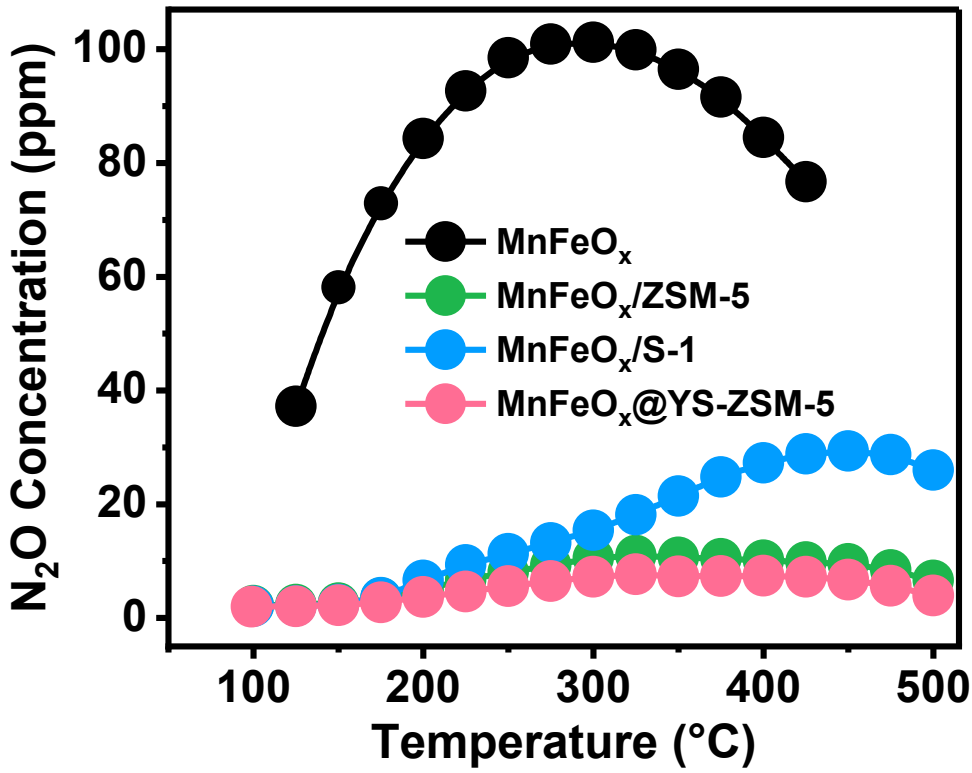

Figure S33. N_2O concentration as a function of temperature in NH_3-SCR reaction over the $MnFeO_x$, $MnFeO_x$/ZSM-5, $MnFeO_x$/S-1 and yolk-shell structured $MnFeO_x$@YS-ZSM-5 catalysts. Reaction conditions: 500 ppm NO, 500 ppm NH_3, 5 vol.% O_2, 5 vol.% H_2O, balanced with N_2, WHSV = 60,000 mL $g_{cat.}^{-1}$ h^{-1}.

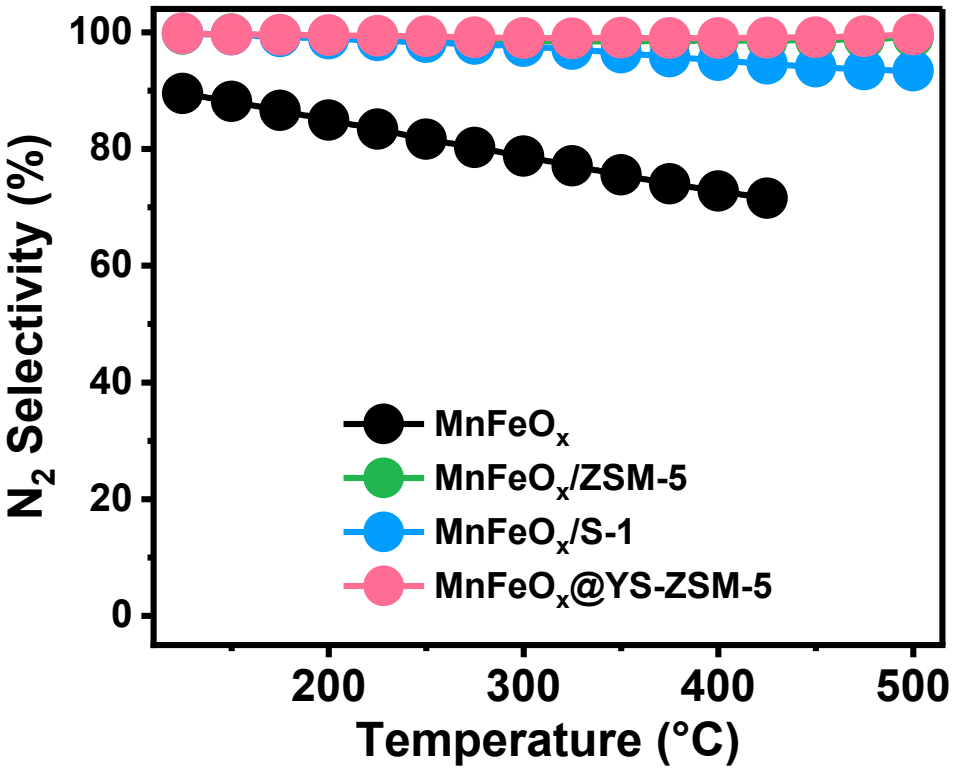

Figure S34. N_2 selectivity as a function of temperature in NH_3-SCR reaction over the $MnFeO_x$, $MnFeO_x$/ZSM-5, $MnFeO_x$/S-1 and yolk-shell structured $MnFeO_x$@YS-ZSM-5 catalysts. Reaction conditions: 500 ppm NO, 500 ppm NH_3, 5 vol.% O_2, 5 vol.% H_2O, balanced with N_2, WHSV = 60,000 mL $g_{cat.}^{-1}$ h^{-1}.

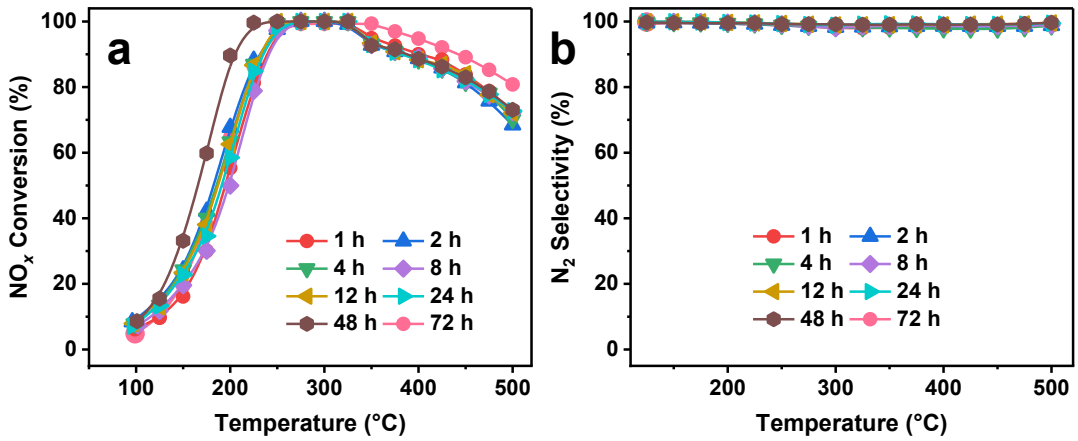

Figure S35. (a) NO_x conversion and (b) N_2 selectivity as a function of temperature in NH_3-SCR reaction over the $MnFeO_x$@YS-ZSM-5 obtained after being hydrothermally treated in TPAOH solution at 170 °C with varying durations. Reaction conditions: 500 ppm NO, 500 ppm NH_3, 5 vol.% O_2, 5 vol.% H_2O, balanced with N_2, WHSV = 60,000 mL $g_{cat.}^{-1}$ h^{-1}.

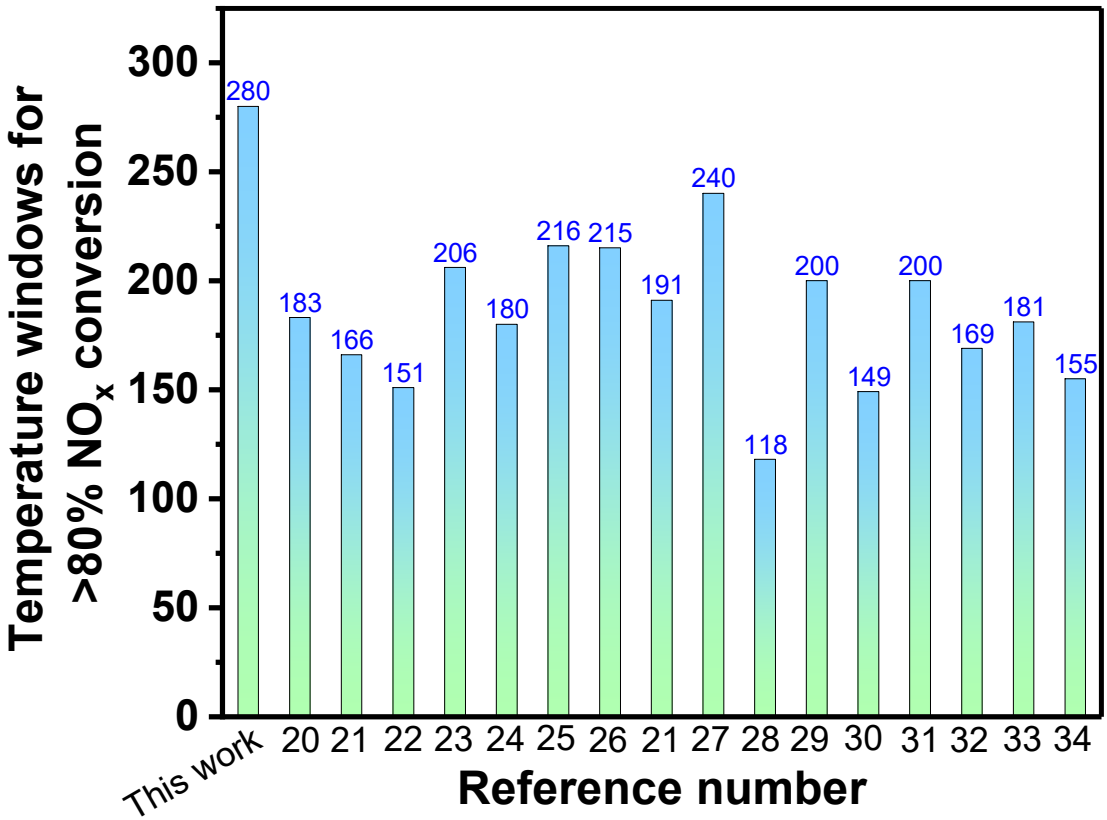

Figure S36. The active temperature windows (NO_x conversion higher than 80%) of the $MnFeO_x$-based NH_3-SCR catalysts reported in the literature.

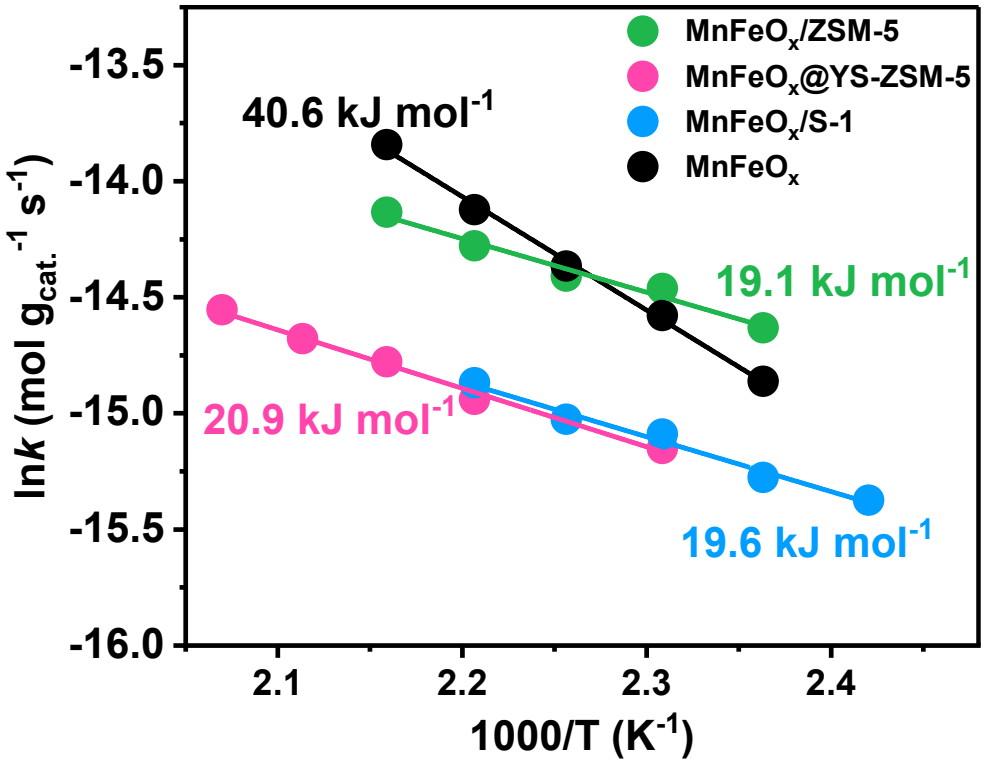

Figure S37. Arrhenius plots of NO_x conversions in SCR over the over the $MnFeO_x$, $MnFeO_x$/ZSM-5, $MnFeO_x$/S-1, and $MnFeO_x$@YS-ZSM-5 catalysts. Reaction conditions: 500 ppm NO, 500 ppm NH_3, 5 vol.% O_2, 5 vol.% H_2O, balanced with N_2, WHSV = 840,000 mL $g_{cat.}^{-1}$ h^{-1}.

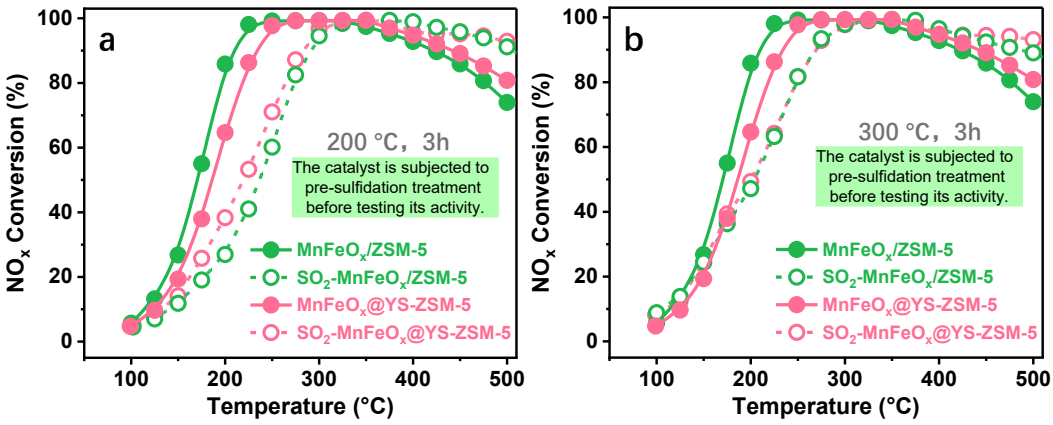

Figure S38. NO_x conversion as a function of temperature in NH_3-SCR reaction over SO_2-pretreated $MnFeO_x$/ZSM-5 and $MnFeO_x$@YS-ZSM-5 catalysts. (a) Samples pre-sulfided at 200 °C for 3 h; (b) Samples pre-sulfided at 300 °C for 3 h. Pre-sulfidation conditions: 50 ppm SO_2, 500 ppm NO, 500 ppm NH_3, 5 vol.% O_2, 5 vol.% H_2O, balanced with N_2, WHSV = 60,000 mL $g_{cat.}^{-1}$ h^{-1}. Reaction conditions: 500 ppm NO, 500 ppm NH_3, 5 vol.% O_2, 5 vol.% H_2O, balanced with N_2, WHSV = 60,000 mL $g_{cat.}^{-1}$ h^{-1}.

Note: SO_2 pre-sulfation experiments were conducted at both 200 and 300 °C, with consistent activity variation trends observed. The activity of $MnFeO_x$/ZSM-5 decreases significantly after pre-sulfation: its low-temperature activity is slightly superior to that of the yolk-shell structured $MnFeO_x$@YS-ZSM-5 nanoreactor before sulfation, but drops to a lower level than SO_2-$MnFeO_x$@YS-ZSM-5 after sulfation. The 300 °C pre-sulfation experiment eliminates the interference of ammonium bisulfate deposition[10], and consistently shows a more pronounced activity decline for the supported catalyst, verifying that the yolk-shell architecture enhances resistance to SO_2 chemical poisoning. Notably, both pre-sulfided catalysts exhibit moderately improved high-temperature

activity relative to the fresh samples. This is attributed to the formation of sulfate (SO_4^{2-}) species on the $MnFeO_x$ surface[11,12], which act as strong Brønsted acid sites in intimate spatial proximity to redox sites and enable more efficient acid-redox synergy than zeolitic framework Brønsted acid sites. Meanwhile, these sulfate-derived acid sites serve as NH_3 reservoirs, and the adsorbed NH_3 can migrate from Brønsted to Lewis acid sites on $MnFeO_x$, an elemental reaction step that has been systematically demonstrated in previous work[13]. This migration process partially suppresses non-selective NH_3 over-oxidation at elevated temperatures and contributes to the enhanced high-temperature performance. The supported $MnFeO_x$/ZSM-5 catalyst suffers from more extensive sulfation due to fully exposed oxide active sites, leading to much more severe low-temperature activity loss despite the same high-temperature promotion effect.

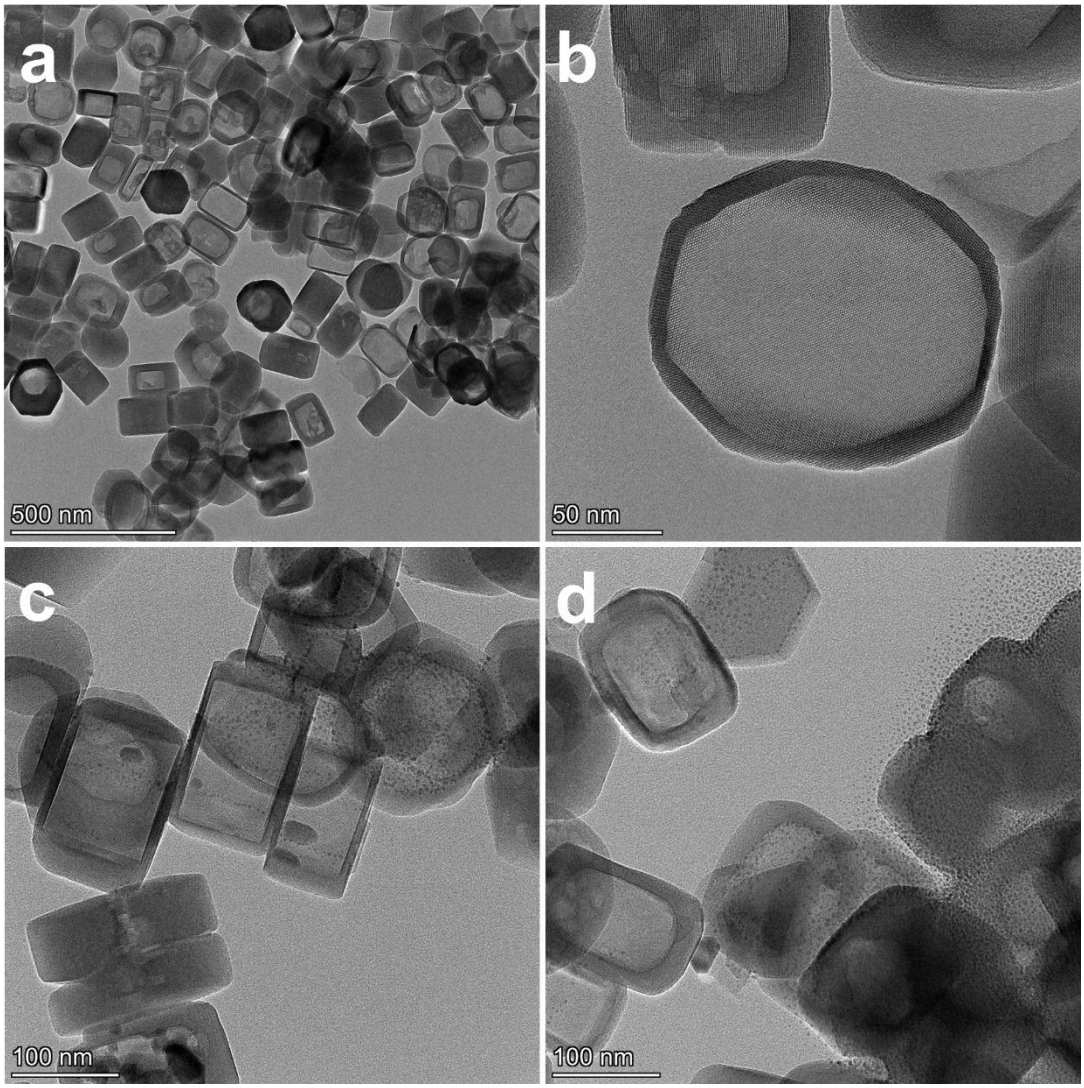

Figure S39. TEM images of the (a, b) Hollow-ZSM-5 zeolite and (c, d) supported $MnFeO_x$/Hollow-ZSM-5 sample.

Note: Hydrothermal treatment of ZSM-5 zeolite with TPAOH successfully yields Hollow-ZSM-5 zeolite with a hollow structure. In the $MnFeO_x$/Hollow-ZSM-5 supported catalyst, $MnFeO_x$ metal oxide nanoparticles are dispersed on the surface of the Hollow-ZSM-5 zeolite.

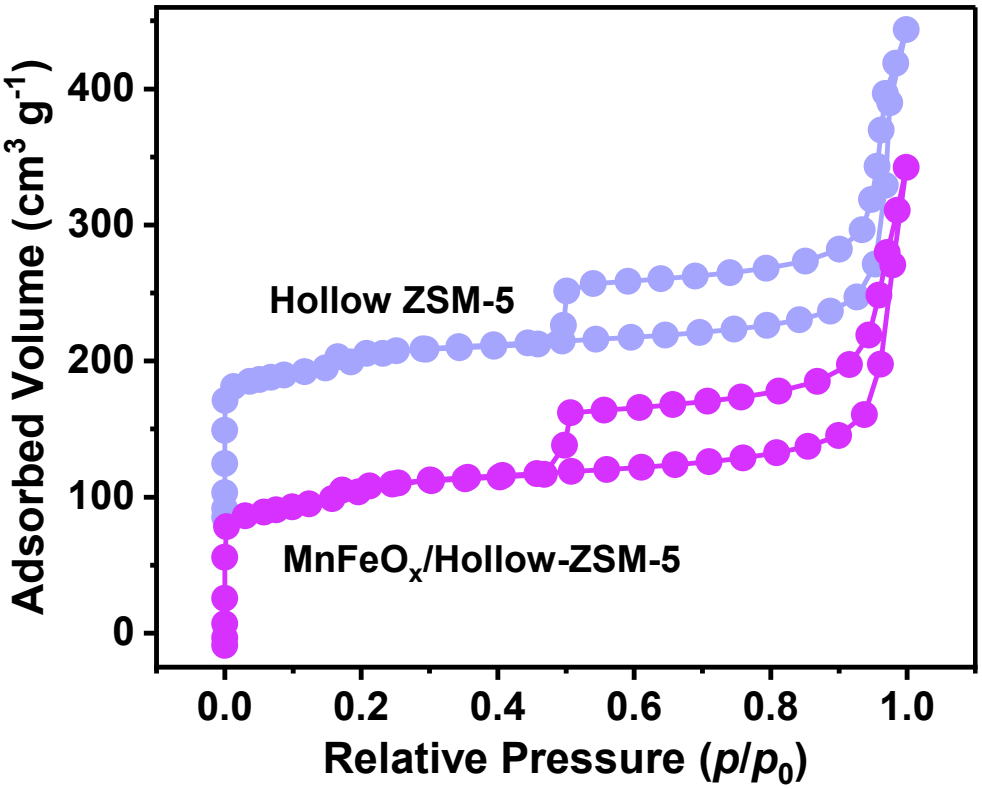

Figure S40. N_2 adsorption-desorption isotherms of the Hollow-ZSM-5 zeolite and supported $MnFeO_x$/Hollow-ZSM-5 samples.

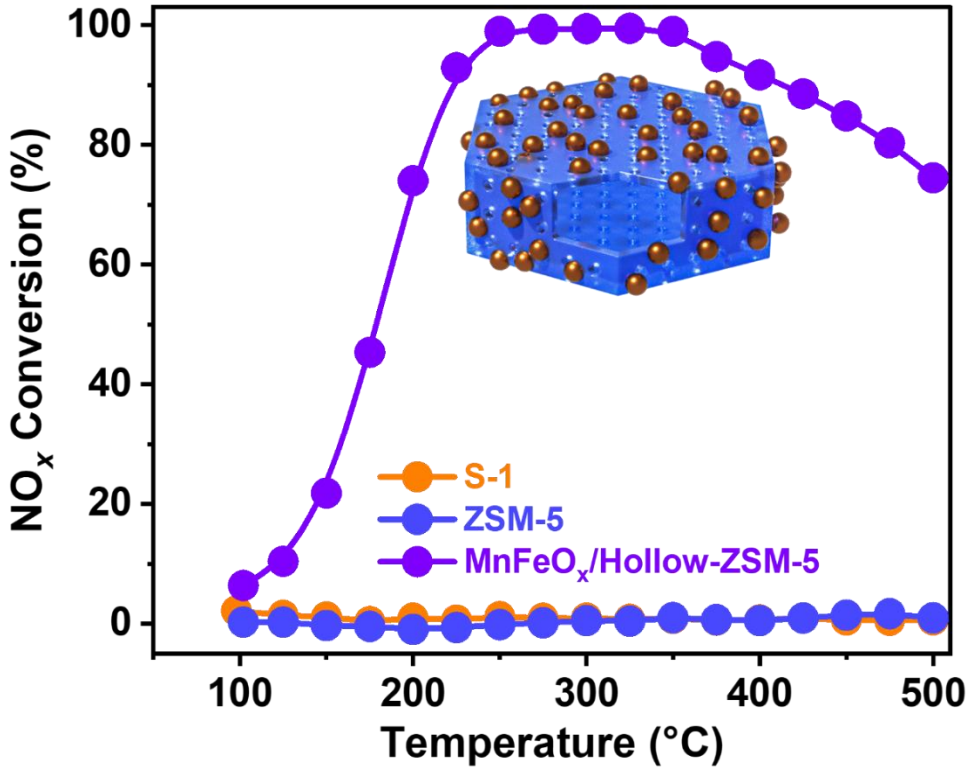

Figure S41. NO_x conversion as a function of temperature in NH_3-SCR reaction over the S-1 zeolite, ZSM-5 zeolite, and supported $MnFeO_x$/Hollow-ZSM-5 samples. Reaction conditions: 500 ppm NO, 500 ppm NH_3, 5 vol.% O_2, 5 vol.% H_2O, balanced with N_2, WHSV = 60,000 mL $g_{cat.}^{-1}$ h^{-1}.

Note: $MnFeO_x$/Hollow-ZSM-5 exhibits NH_3-SCR activity comparable to that of the yolk-shell structured $MnFeO_x$@YS-ZSM-5 nanoreactor.

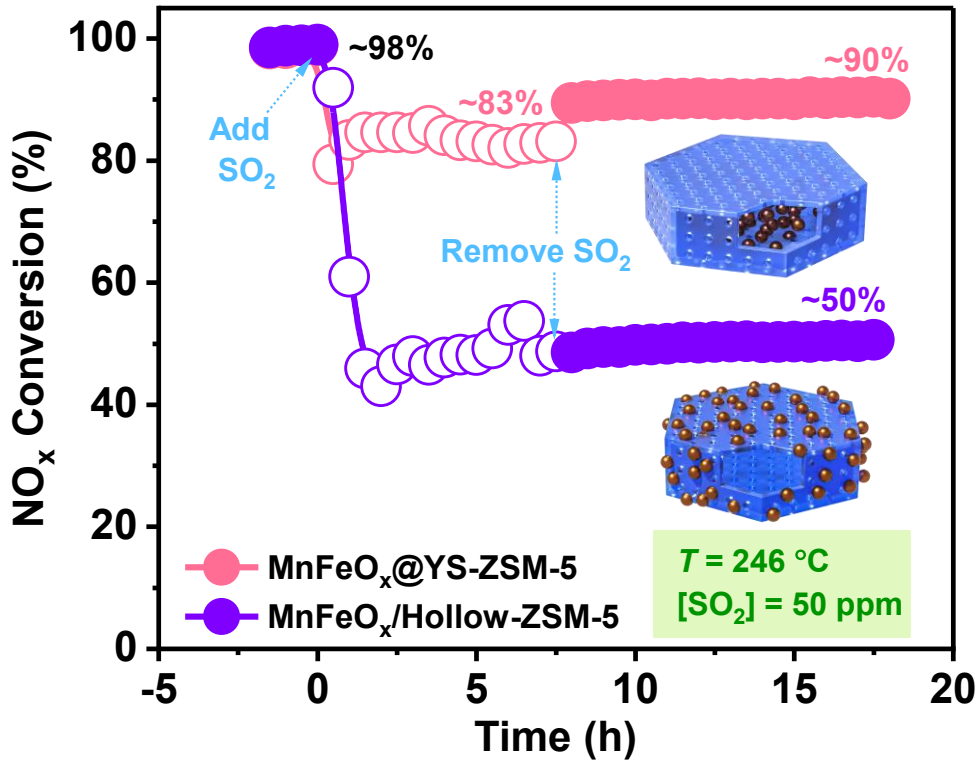

Figure S42. SO_2 resistance performance over the supported $MnFeO_x$/Hollow-ZSM-5 and yolk-shell structured $MnFeO_x$@YS-ZSM-5 catalysts at 246 °C. Reaction conditions: 500 ppm NO, 500 ppm NH_3, 5 vol.% O_2, 5 vol.% H_2O, 50 ppm SO_2 (when used), balanced with N_2, WHSV = 60,000 mL $g_{cat.}^{-1}$ h^{-1}.

Note: The SO_2 poisoning resistance over the supported $MnFeO_x$/Hollow-ZSM-5 catalyst is significantly lower than that of the yolk-shell structured $MnFeO_x$@YS-ZSM-5 catalyst. Upon introduction of 50 ppm SO_2 at 246 °C for 2 h, the NO_x conversion over $MnFeO_x$/Hollow-ZSM-5 decreased from an initial 98% to ~43%, and remained consistently around 48% over the subsequent 5.5 h. After terminating SO_2 supply, the NO_x conversion efficiency only slightly increased to approximately 50%.

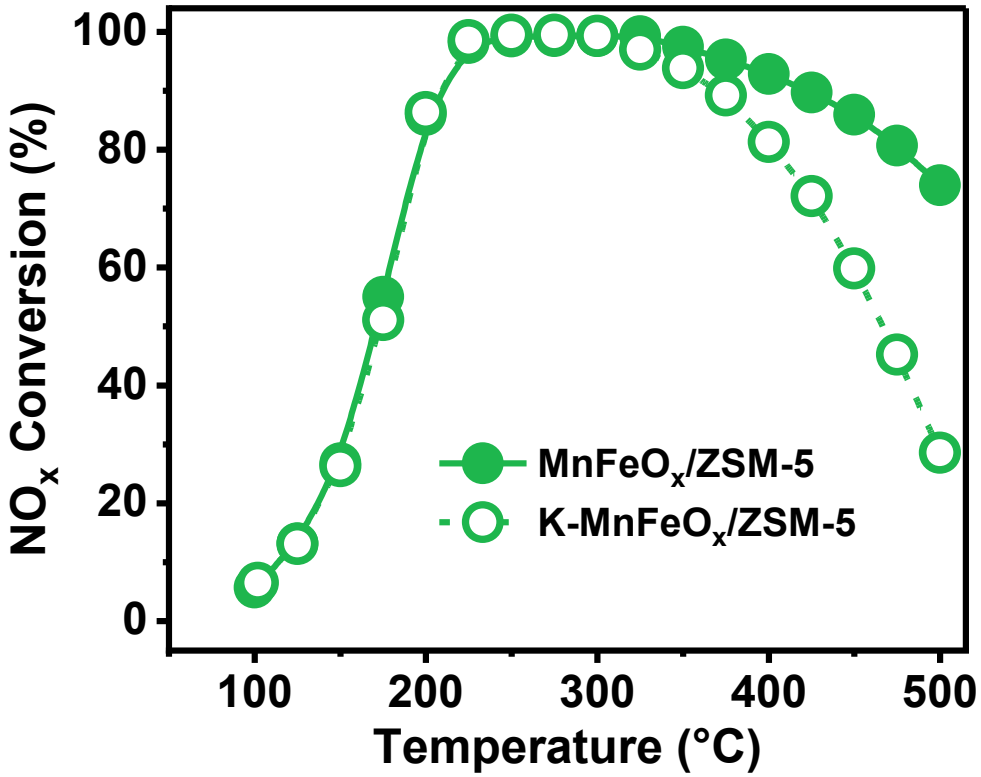

Figure S43. NO_x conversion as a function of temperature in NH_3-SCR reaction over the K-$MnFeO_x$/ZSM-5 and $MnFeO_x$/ZSM-5 catalysts. Reaction conditions: 500 ppm NO, 500 ppm NH_3, 5 vol.% O_2, 5 vol.% H_2O, balanced with N_2, WHSV = 60,000 mL $g_{cat.}^{-1}$ h^{-1}.

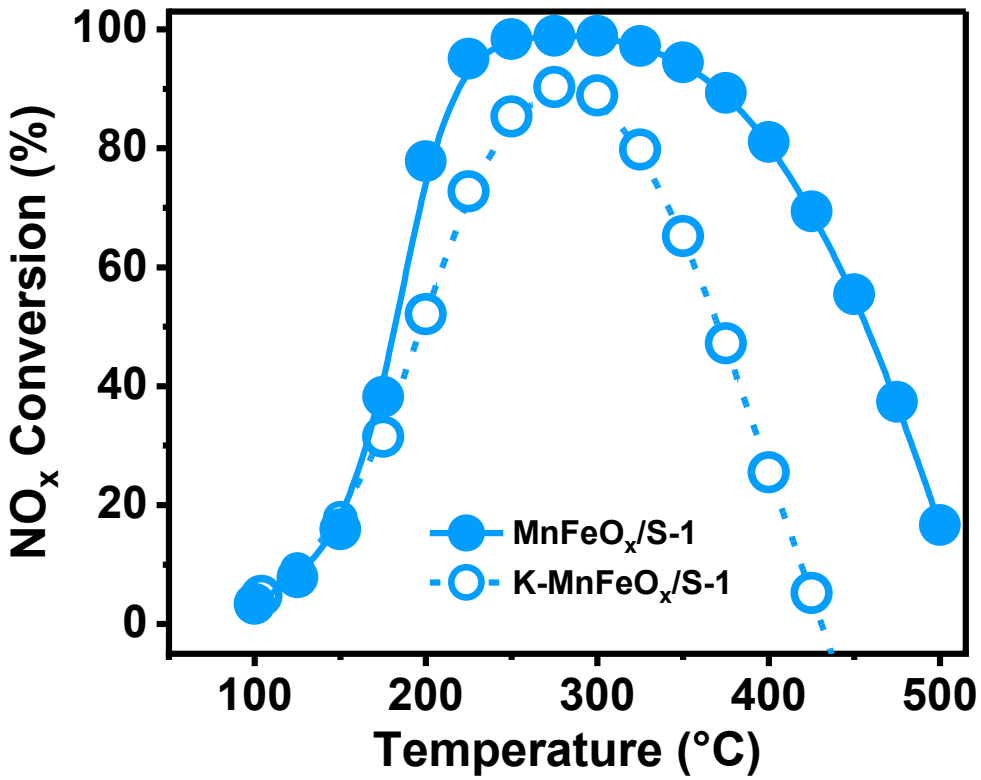

Figure S44. NO_x conversion as a function of temperature in NH_3-SCR reaction over the K-$MnFeO_x$/S-1 and $MnFeO_x$/S-1 catalysts. Reaction conditions: 500 ppm NO, 500 ppm NH_3, 5 vol.% O_2, 5 vol.% H_2O, balanced with N_2, WHSV = 60,000 mL $g_{cat.}^{-1}$ h^{-1}.

Note: The low-temperature activity of the alkali metal-poisoned K-$MnFeO_x$/S-1 catalyst decreases significantly; its activity in the medium-to-high temperature range drops even more sharply, and the active temperature window narrows drastically. This is primarily attributed to the weaker surface acidity of S-1 zeolite compared to ZSM-5 zeolite, which results in its inferior ability to resist K poisoning.

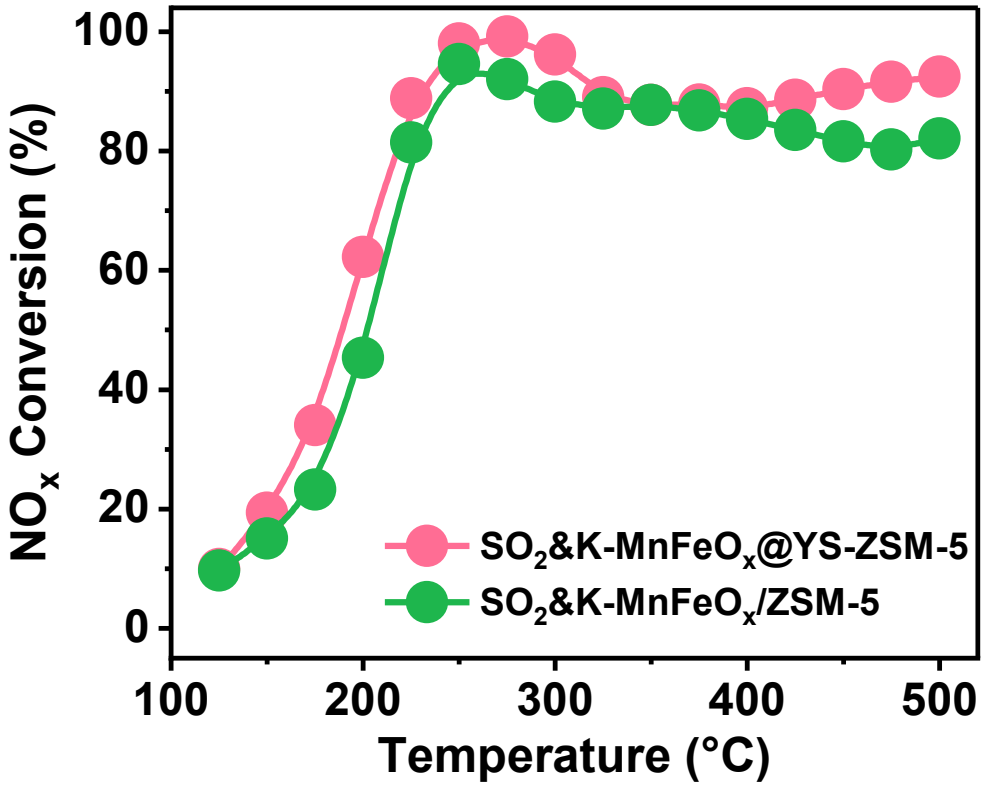

Figure S45. NO_x conversion as a function of temperature in NH_3-SCR reaction over the K-$MnFeO_x$/ZSM-5 and K-$MnFeO_x$@YS-ZSM-5 catalysts under the 50 ppm SO_2 atmosphere. Reaction conditions: 50 ppm SO_2, 500 ppm NO, 500 ppm NH_3, 5 vol.% O_2, 5 vol.% H_2O, balanced with N_2, WHSV = 60,000 mL $g_{cat.}^{-1}$ h^{-1}.

Note: It presents the performance results for SO_2/alkali metal co-poisoning resistance of the $MnFeO_x$/ZSM-5 and $MnFeO_x$@YS-ZSM-5 catalysts, specifically, the catalysts were first subjected to K poisoning, followed by NH_3-SCR performance testing with 50 ppm SO_2 in the reaction gas. From the figure, the yolk-shell structured $MnFeO_x$@YS-ZSM-5 nanoreactor exhibits excellent resistance to SO_2/alkali metal co-poisoning and shows higher low-temperature activity than the supported $MnFeO_x$/ZSM-5 catalyst.

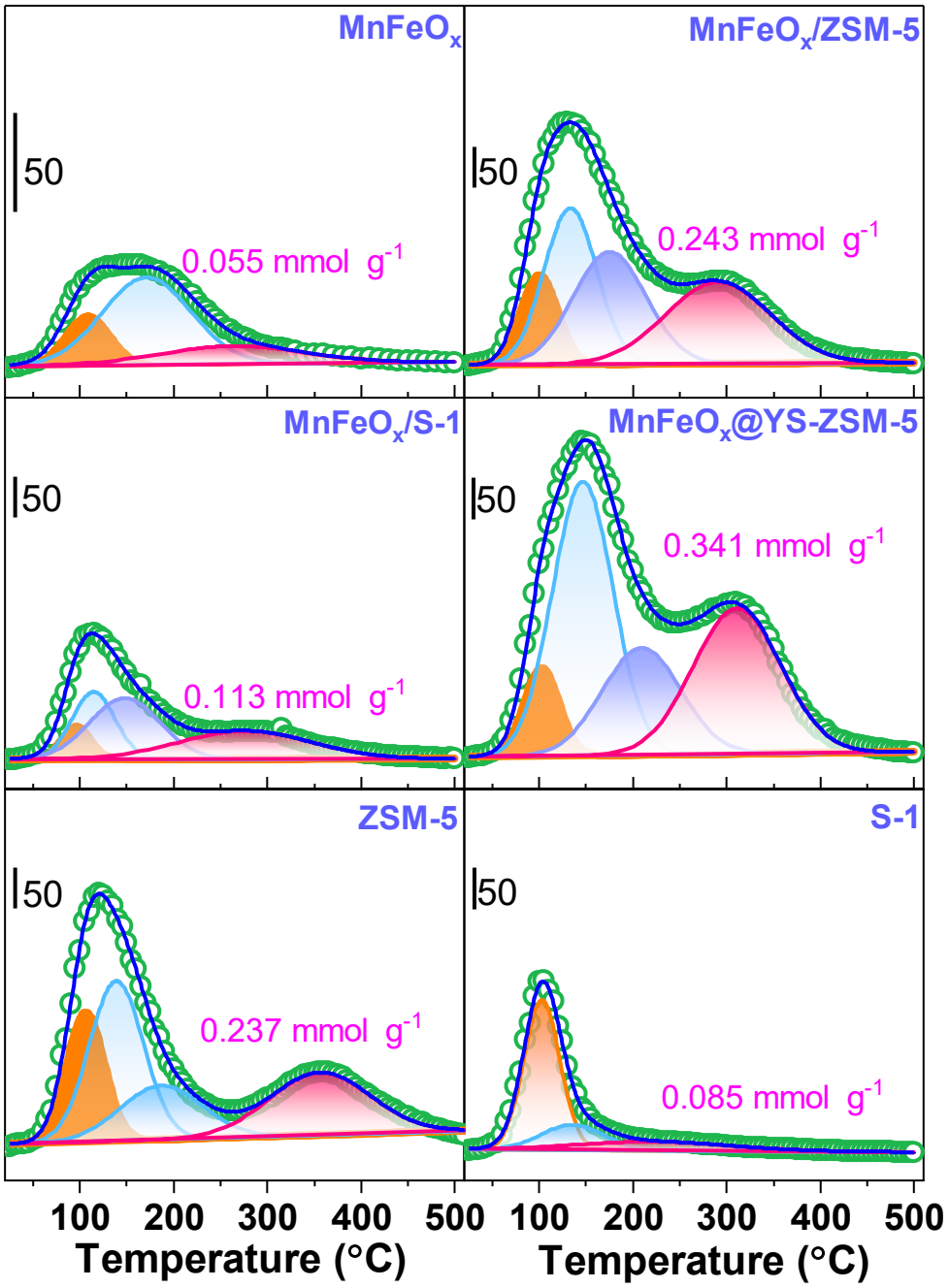

Figure S46. NH_3-TPD curves over the fresh S-1 zeolite, ZSM-5 zeolite, pure $MnFeO_x$, $MnFeO_x$/ZSM-5, $MnFeO_x$/S-1, and yolk-shell structured $MnFeO_x$@YS-ZSM-5 samples.

Note: It is generally accepted that NH_3 desorption peaks below 200 °C are attributed to NH_3 desorption from weak acid sites, those in the range of 200–350 °C correspond to

NH_3 desorption from medium-strong acid sites, and those peaks above 350 °C are ascribed to NH_3 desorption from strong acid sites[14]. The pure $MnFeO_x$ catalyst exhibits the weakest surface acidity and the lowest acid amount, which are far lower than those of the other three oxides-zeolite coupled catalysts ($MnFeO_x$/ZSM-5, $MnFeO_x$/S-1, and $MnFeO_x$@YS-ZSM-5). In contrast, the yolk-shell structured $MnFeO_x$@YS-ZSM-5 catalyst not only exhibits the highest total acid amount but also has the largest fraction of medium-strong acid sites.

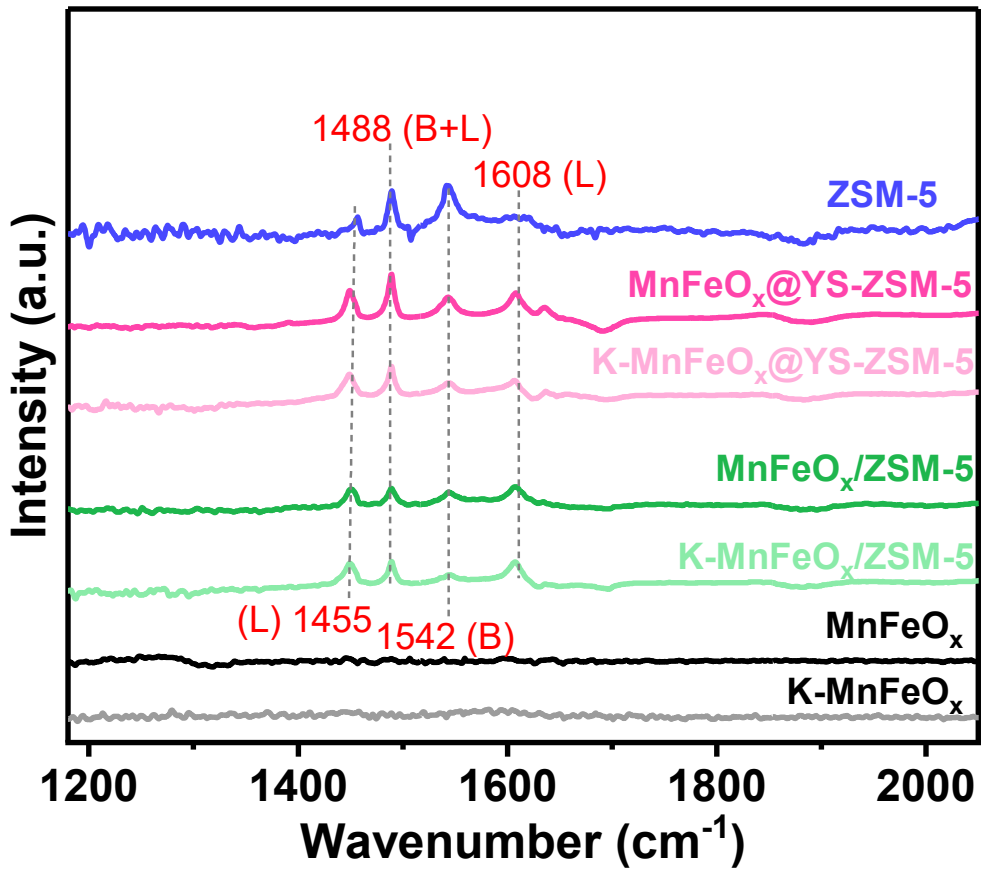

Figure S47. Py-IR spectra over the fresh ZSM-5 zeolite, supported $MnFeO_x$/ZSM-5, yolk-shell structured $MnFeO_x$@YS-ZSM-5, and related K-poisoned samples at 260 °C.

Note: The infrared vibration peaks at wavenumbers of 1608 and 1455 cm^{-1} are attributed to the adsorption of NH_3 on Lewis acid sites, the peak at 1542 cm^{-1} to the adsorption of NH_3 on Brønsted acid sites, and the peak at 1488 cm^{-1} to the co-adsorption of NH_3 on both Lewis and Brønsted acid sites[15]. The Py-IR spectrum of the fresh $MnFeO_x$ catalyst is almost a flat line, indicating extremely weak acidity. All oxides-zeolite coupled samples exhibit abundant and intense Lewis and Brønsted acid sites. The results of the Py-IR characterization corroborate those of the NH_3-TPD analysis; the abundant presence of medium-strong acid sites is conducive to enhancing the medium-to-high temperature NH_3-SCR activity of the catalysts.

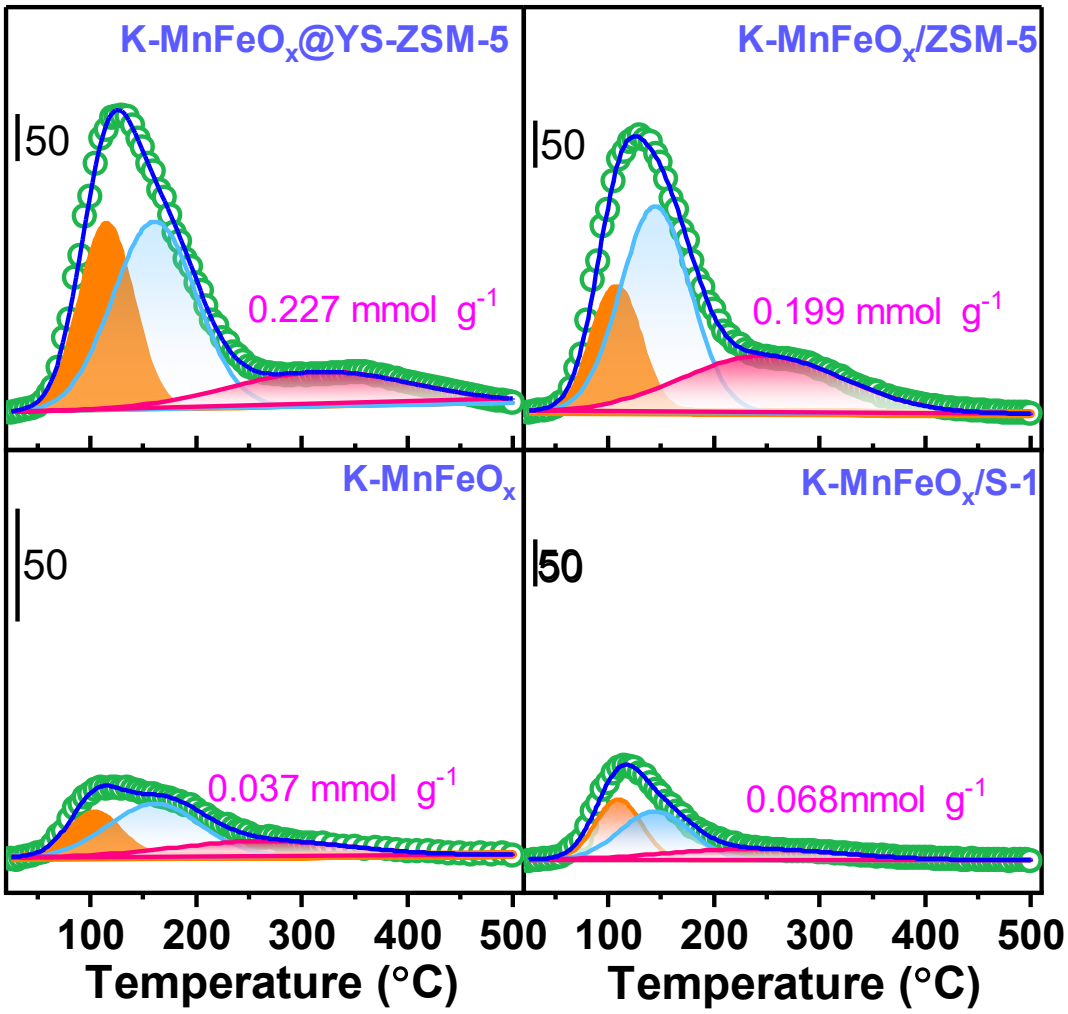

Figure S48. NH_3-TPD curves of the K-poisoned catalysts.

Note: The total acid amount of the K-$MnFeO_x$ catalyst decreases by 33% compared to the fresh $MnFeO_x$ catalyst, whereas K-$MnFeO_x$/ZSM-5 and K-$MnFeO_x$@YS-ZSM-5 exhibit significantly smaller reductions in total acid amount. After K poisoning, the K-$MnFeO_x$@YS-ZSM-5 catalyst maintains the highest total acid amount—which is the key reason for its much better NH_3-SCR performance after K poisoning.

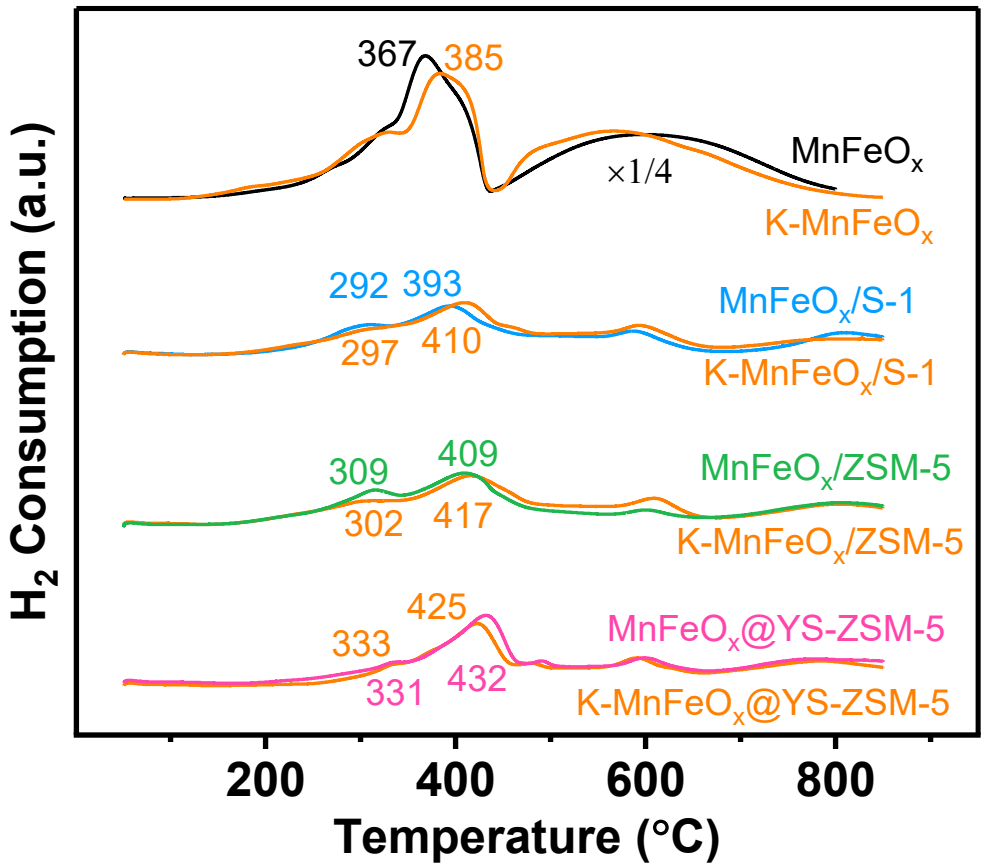

Figure S49. H_2-TPR profiles over the fresh and K-poisoned catalysts.

Note: Compared with the fresh catalyst, the reduction peaks of the K-$MnFeO_x$ catalyst exhibit the largest shift toward higher temperatures. In contrast, the other K-poisoned catalysts show negligible changes in their reduction peak temperatures; thus, their oxidation capacity is maintained. The alkali metal K exerts a significant poisoning effect on the pure $MnFeO_x$ metal oxide catalyst, and K poisoning impairs the oxidation performance of K-$MnFeO_x$ catalyst.

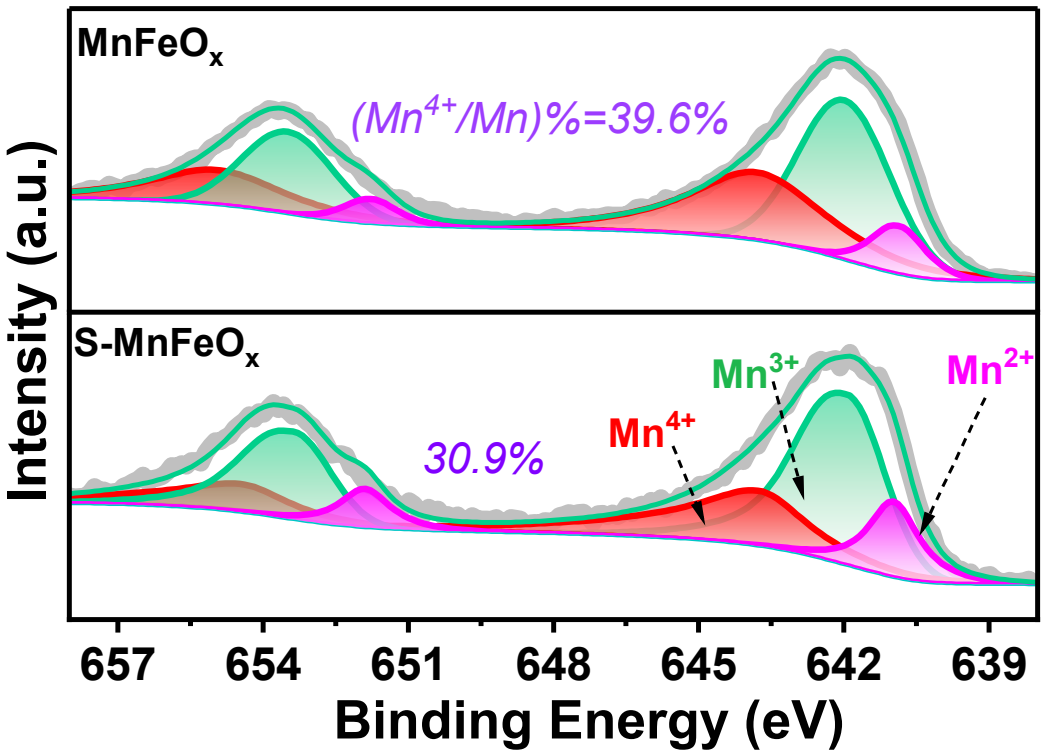

Figure S50. Mn 2p XPS spectra of pure $MnFeO_x$ and S-$MnFeO_x$ samples.

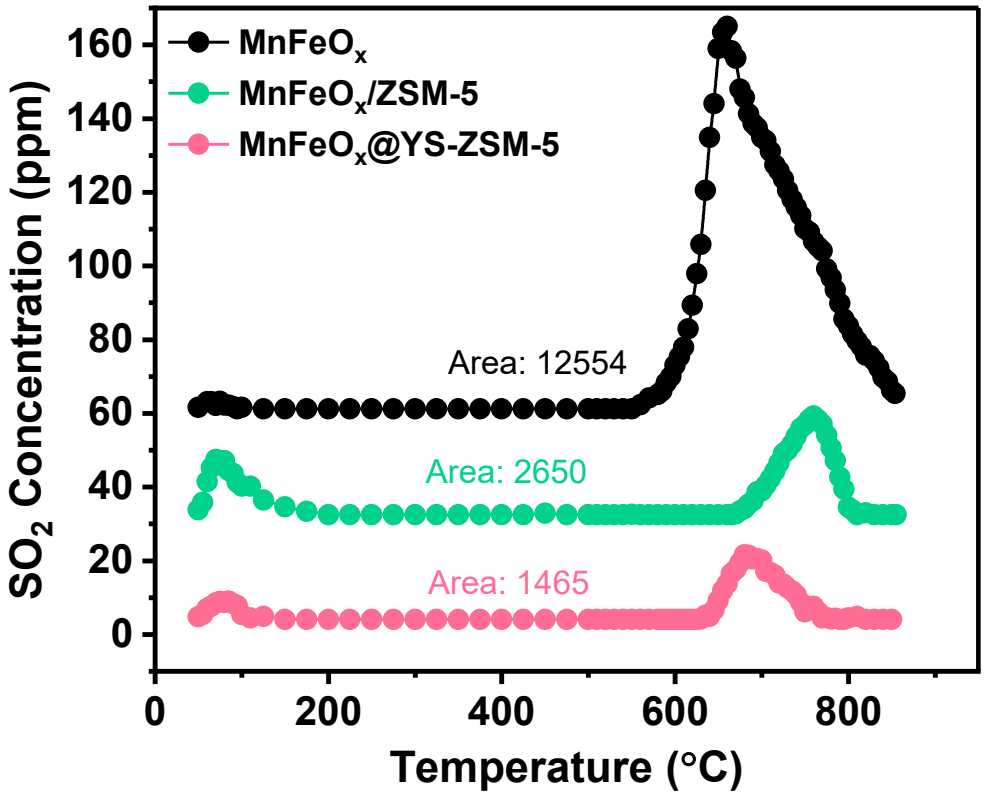

Figure S51. SO_2-TPD curves over the $MnFeO_x$, $MnFeO_x$/ZSM-5, and yolk-shell structured $MnFeO_x$@YS-ZSM-5 samples.

Note: The yolk-shell structured $MnFeO_x$@YS-ZSM-5 exhibits the smallest total SO_2 desorption peak area, indicating reduced sulfate formation on $MnFeO_x$@YS-ZSM-5 nanoreactor.

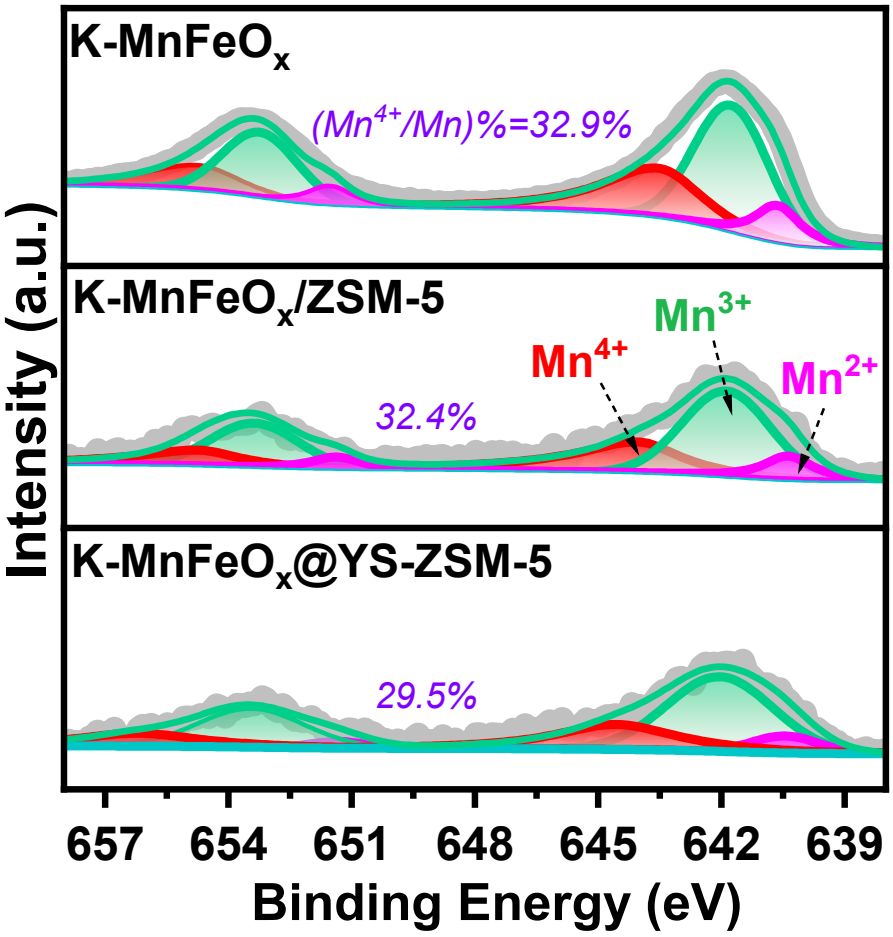

Figure S52. Mn 2p XPS spectra of the K-poisoned catalysts.

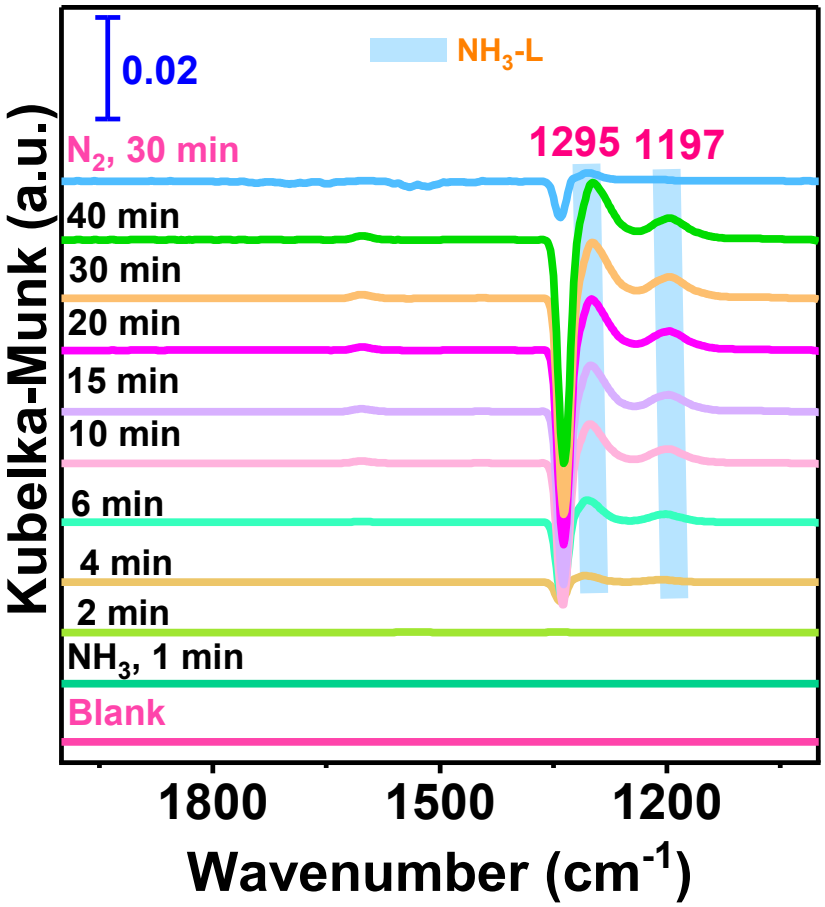

Figure S53. *In situ* DRIFT spectra of NH_3 adsorption over the pure $MnFeO_x$ catalyst at 200 °C.

Note: At 4 min of NH_3 adsorption, characteristic peaks at 1197 and 1295 cm^{-1} are observed, both absorption peaks are attributed to NH_3 species adsorbed on Lewis acid sites (NH_3-L) over the catalyst surface[16,17]. With increasing adsorption time, the intensities of these two characteristic peaks increase slowly and eventually reach saturation. After 40 min of adsorption, followed by N_2 purging for 30 min, a significant decrease in the peak intensities is observed, indicating weak acidity of the Lewis acid sites on the catalyst surface and their poor ability to adsorb NH_3.

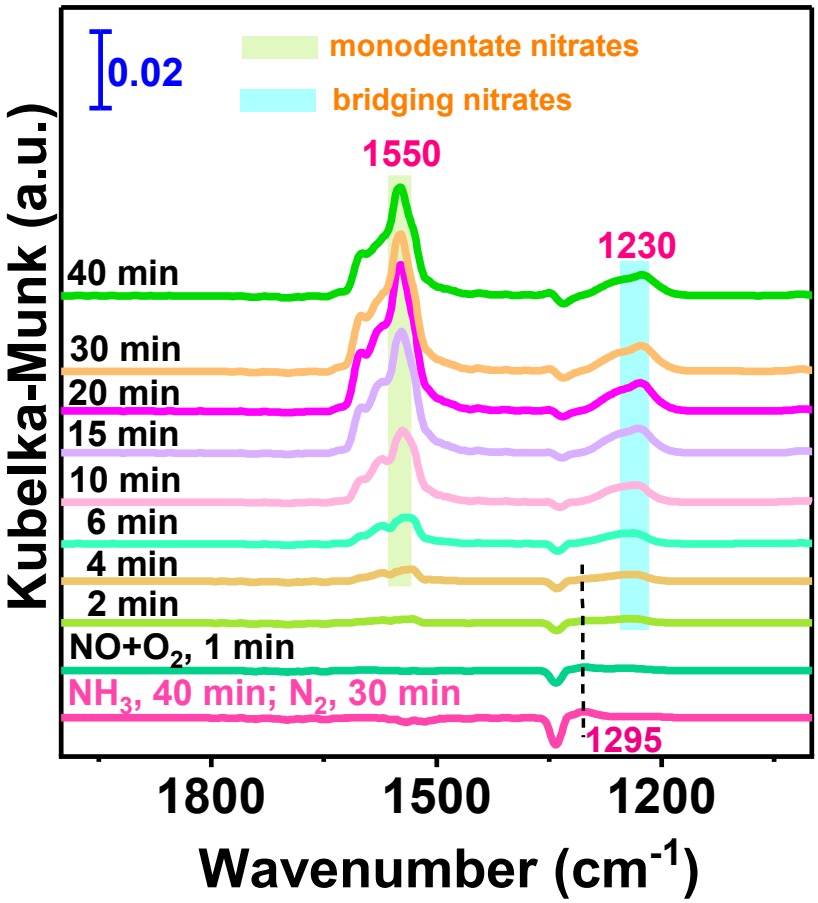

Figure S54. *In situ* DRIFT spectra of pre-adsorbed NH_3 species reacted with NO + O_2 over the pure $MnFeO_x$ catalyst at 200 °C.

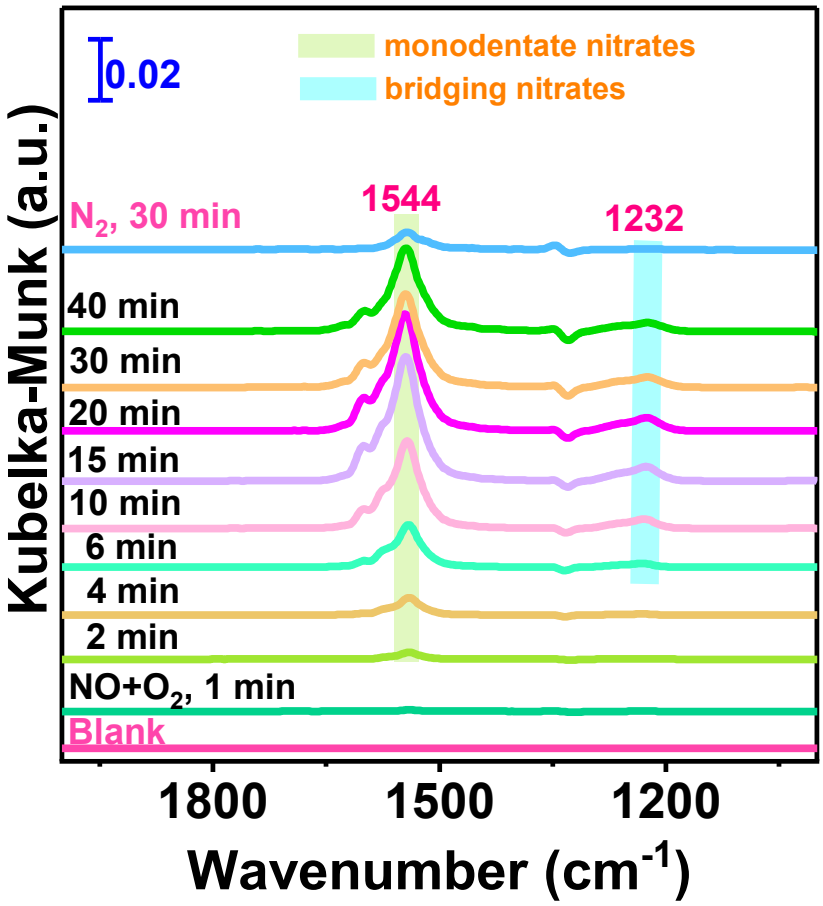

Figure S55. *In situ* DRIFT spectra of NO + O_2 adsorption over the pure $MnFeO_x$ catalyst at 200 °C.

Note: After adsorption of NO + O_2 on pure $MnFeO_x$, infrared characteristic peaks of monodentate nitrates (1544 cm^{-1}) and bridging nitrates (1232 cm^{-1}) rapidly form on its surface[18,19], and the intensities of these peaks increase rapidly with prolonged adsorption time.

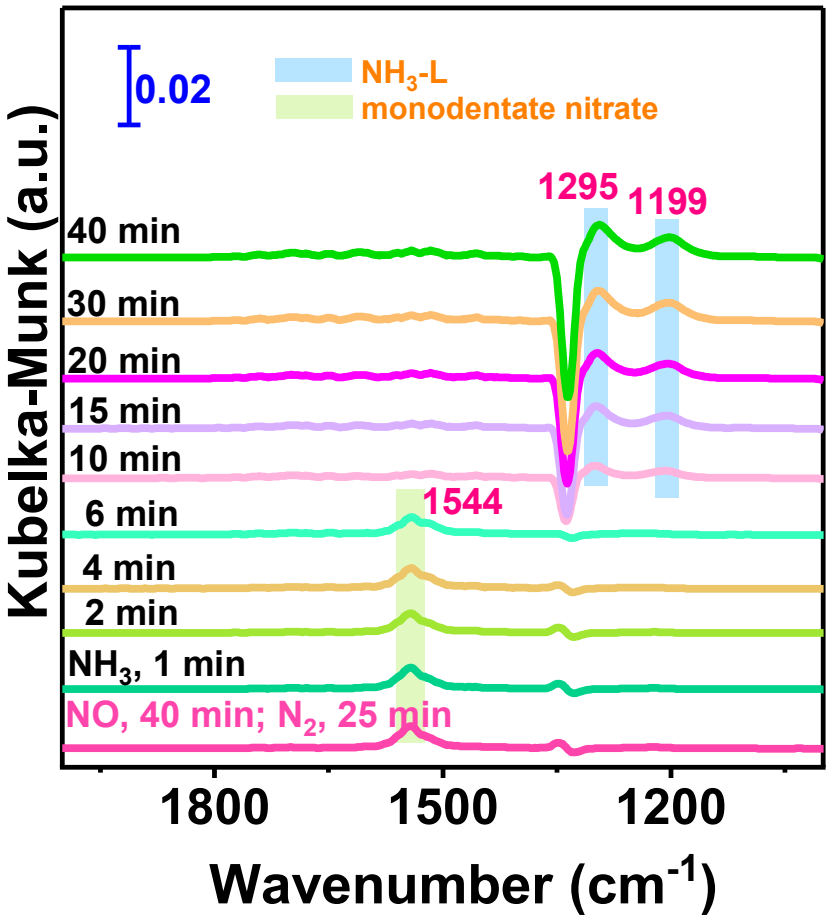

Figure S56. *In situ* DRIFT spectra of pre-adsorbed NO + O_2 species reacted with NH_3 over the pure $MnFeO_x$ catalyst at 200 °C.

Note: Upon introduction of NH_3, the intensity of the vibrational peaks corresponding to monodentate nitrates on the catalyst surface gradually decreases, and the peaks disappear completely after 10 min. Subsequently, NH_3-L species emerge on the catalyst surface. Thus, the reaction follows the typical Langmuir-Hinshelwood mechanism, wherein adsorbed NO species react with adsorbed NH_3 species.

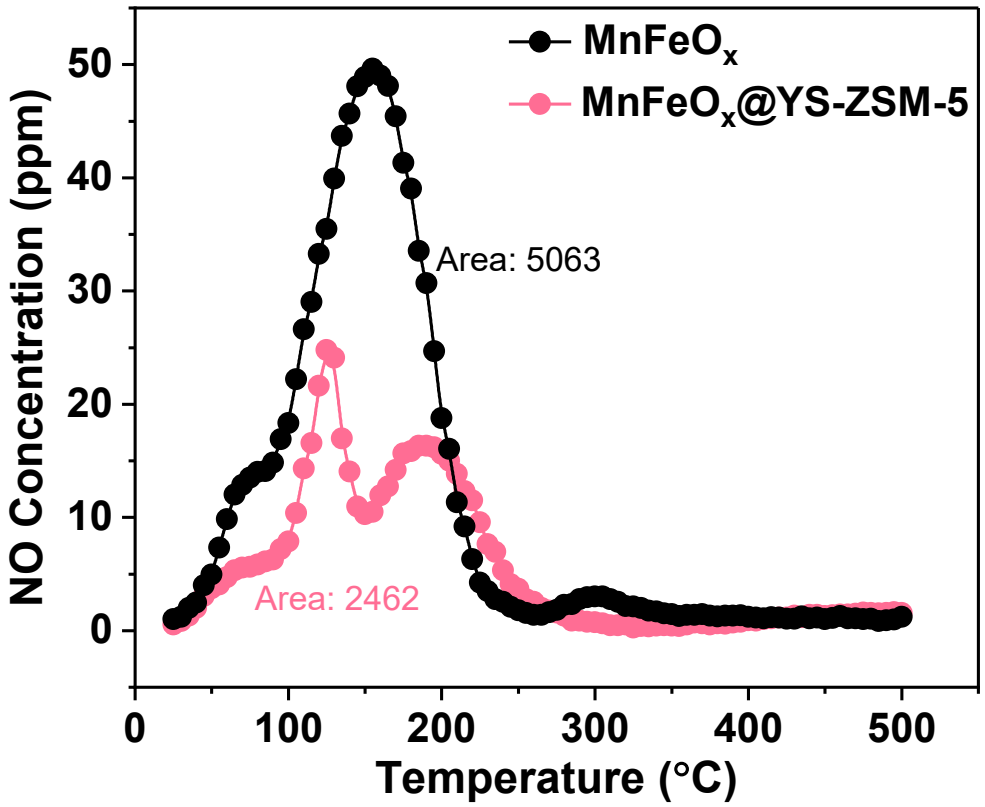

Figure S57. NO-TPD curves of the pure $MnFeO_x$ and yolk-shell structured $MnFeO_x$@YS-ZSM-5 samples.

Note: Pure $MnFeO_x$ exhibits a larger NO desorption peak area, indicating that more NO is adsorbed onto the surface.

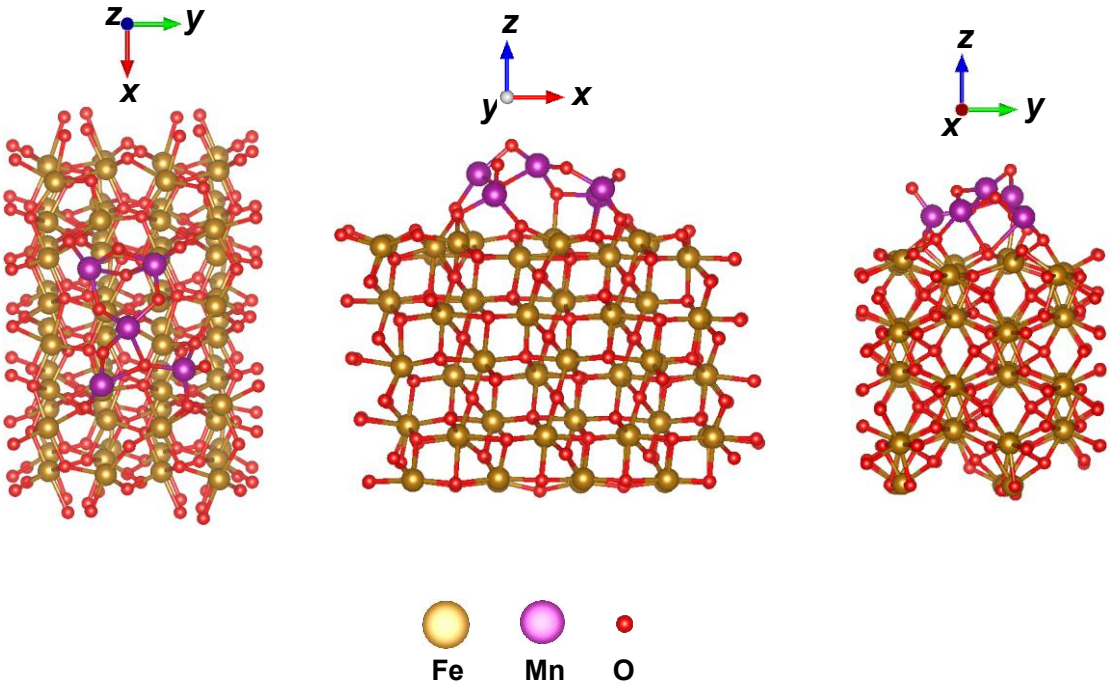

Figure S58. Top view and side view of optimized $MnFeO_x$ structure.

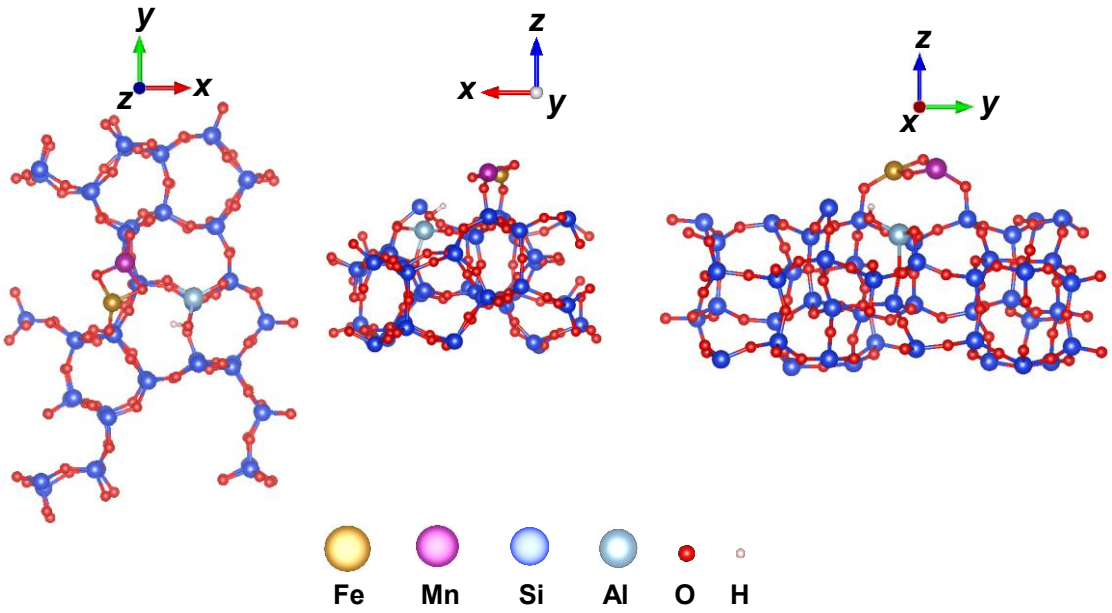

Figure S59. Top view and side view of optimized $MnFeO_x$@YS-ZSM-5 structure.

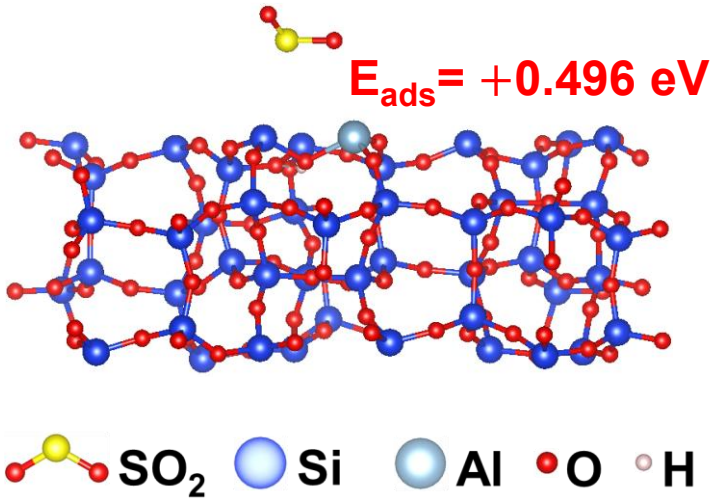

Figure S60. Optimized adsorption configurations of SO_2 molecules on Brønsted acid sites in ZSM-5 zeolite structure.

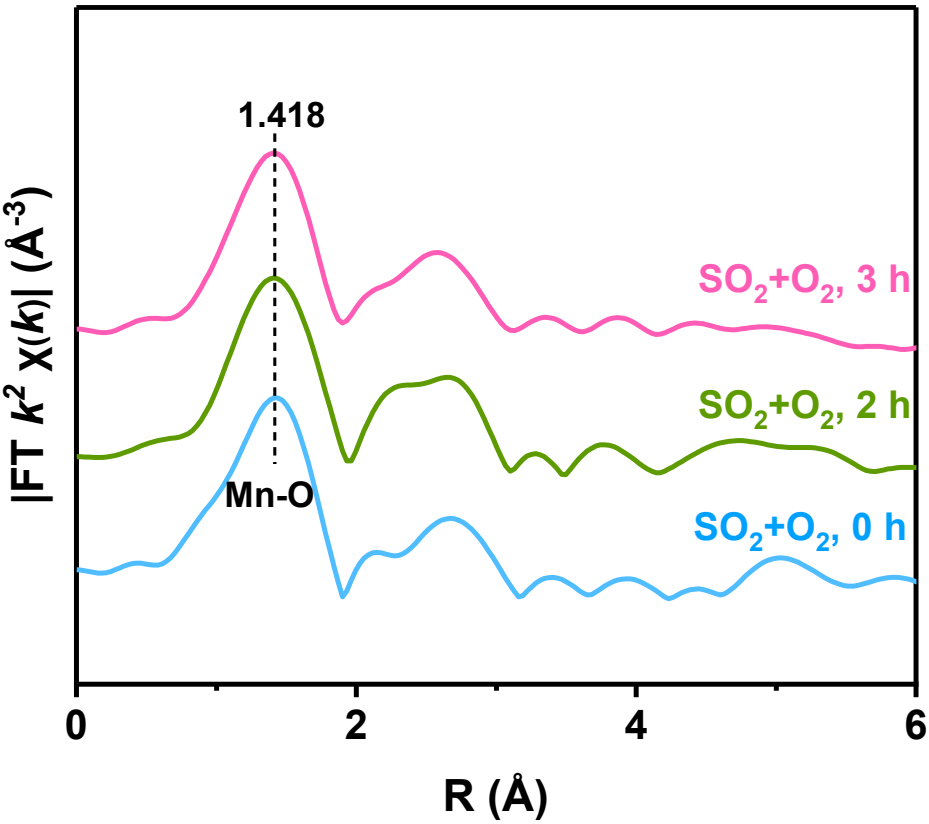

Figure S61. *In situ* Mn *K*-edge EXAFS spectra for the transient reaction over yolk-shell structured $MnFeO_x$@YS-ZSM-5 nanoreactor after treatment for 0, 2, and 3 h at 246 °C in a 250 ppm SO_2 + 5 vol.% O_2 atmosphere.

Supplementary Tables

Table S1. Specific surface area and pore volume of the samples.

Samples	S_{BET} [a] ($m^2\ g^{-1}$)	V_{total} [b] ($cm^3\ g^{-1}$)
ZSM-5	461	0.29
$MnFeO_x$/ZSM-5	341	0.33
$MnFeO_x$@YS-ZSM-5	344	0.41
$MnFeO_x$	25	0.20
$MnFeO_x$/S-1	285	0.25
S-1	339	0.27

[a] Calculated by BET method.

[b] Determined by BJH method.

Note: The Brunauer-Emmett-Teller (BET) surface area remained nearly unchanged after the TPAOH hydrothermal treatment, whereas the total pore volume increased from 0.33 $cm^3\ g^{-1}$ for $MnFeO_x$/ZSM-5 to 0.41 $cm^3\ g^{-1}$ for $MnFeO_x$@YS-ZSM-5 nanoreactor. This increase can be attributed to the cavity formation during the hollowing of the ZSM-5 zeolite.

Table S2. Comparison with literature about the performances of $MnFeO_x$-based catalysts for NH_3-SCR.

Catalysts	Temperature window for >80% NO_x conversion	References
$MnFeO_x$@YS-ZSM-5	280 °C	This work
MnFe-AC	183 °C	[20]
MnFe	166 °C	[21]
MnFe	151 °C	[22]
$MnFeO_x$	206 °C	[23]
$MnFeO_x$	180 °C	[24]
MnO_x-FeO_x nanoneedles	216 °C	[25]
Mn-Fe	215 °C	[26]
SmMnFe-0.1	191 °C	[21]
Mn10Fe10/W5Ti	240 °C	[27]
MnFeCe	118 °C	[28]
MnFe-TOS	200 °C	[29]
MnFeCeAl-Nb	149 °C	[30]
5Fe–3Mn–S/TiO_2	200 °C	[31]
11.2Fe11Mn/SBA-15	169 °C	[32]
Fe-Mn/CeO_2	181 °C	[33]
Mn–Fe/TS-1(R-2)	155 °C	[34]

Mass and Heat Transfer Calculations for NH_3-SCR upon different catalyst

For PBR reaction mode (0.05% NO/ 0.05% NH_3 / 5% O_2/ 94.9% N_2)

Mears Criterion for External Diffusion

The absence of mass transport resistances was checked by Mears' criterion (C_M) for external diffusion:

$$C_M = \frac{r\rho_b R_p n}{k_c C_{Ab}} < 0.15$$

where $r = \frac{X_{NO_{x,m}} F_{NO_x}}{m_{cat.}}$, mol $kg_{cat.}^{-1}$ s^{-1};

F_{NO_x} = gas flow rate of NO_x, mol s^{-1};

$m_{cat.}$ = mass weight of the sample = 0.0250 g;

T_m = the maximum temperatures during NH_3-SCR kinetic measurements, K;

$X_{NO_{x,m}}$ = the NO_x conversion at maximum temperatures;

n = reaction order = 1;

R_p = catalyst particle radius = 1.35×10^{-4} m;

ρ_c = solid catalyst density, kg m^{-3};

ρ_b = bulk density of catalyst bed, kg m^{-3};

$\rho_c \approx \rho_b \approx \rho_{cat.}$;

k_c = external mass transfer coefficient = 0.1 m s^{-1};

C_{Ab} = bulk gas concentration of NO_x at maximum temperatures, mol m^{-3}.

For the kinetic measurements, a total gas flow rate of 350 mL min^{-1} and a catalyst particle size of 0.27 mm were employed. And the highest concentration of NO_x employed in the feed was 0.05%.

Table S3. The C_M over the various catalysts in NH_3-SCR performance.

Catalysts	ρ_b	T_m	r	$X_{NO_{x,m}}$	C_{Ab}	C_M
$MnFeO_x$	2027	463.15	8.88×10^{-4}	17.0%	0.0185	0.1313
$MnFeO_x$/ZSM-5	748	463.15	6.79×10^{-4}	13.0%	0.0194	0.0353
$MnFeO_x$/S-1	782	433.15	3.40×10^{-4}	6.5%	0.0208	0.0172
$MnFeO_x$@YS-ZSM-5	733	473.15	4.56×10^{-4}	8.7%	0.0203	0.0221

$C_M < 0.15$, therefore, external mass transfer effects can be neglected.

Weisz-Prater Criterion for Internal Diffusion

The absence of mass transport resistances was checked by Weisz-Prater criterion (C_{WP}) for internal diffusion:

$$C_{WP} = \frac{r_{obs}\rho_c R_p^2}{D_{eff} C_{As}} < 1$$

where r_{obs} = observed reaction rate ≈ $r = \frac{X_{NO_{x,m}} F_{NO_x}}{m_{cat.}}$, mol $kg_{cat.}^{-1}$ s^{-1};

F_{NO_x} = gas flow rate of NO_x, mol s^{-1};

$m_{cat.}$ = mass weight of the sample = 0.0250 g;

T_m = the maximum temperatures during NH_3-SCR kinetic measurements, K;

$X_{NO_{x,m}}$ = the NO_x conversion at maximum temperatures;

n = reaction order = 1;

R_p = catalyst particle radius = 1.35×10^{-4} m;

ρ_c = solid catalyst density, kg m^{-3};

ρ_b = bulk density of catalyst bed, kg m^{-3}

$\rho_c \approx \rho_b \approx \rho_{cat.}$;

D_{eff} = effective diffusivity = 8.9×10^{-6} m^2 s^{-1};

C_{As} = gas concentration of NO_x at the catalyst surface, mol m^{-3}, $C_{As} \approx C_{Ab}$.

Table S4. The C_{WP} over the various catalysts in NH_3-SCR performance.

Catalysts	ρ_c	T_m	r_{obs}	$X_{NO_{x,m}}$	C_{As}	C_{WP}
$MnFeO_x$	2027	463.15	8.88×10^{-4}	17.0%	0.0185	0.1991
$MnFeO_x$/ZSM-5	748	463.15	6.79×10^{-4}	13.0%	0.0194	0.0536
$MnFeO_x$/S-1	782	433.15	3.40×10^{-4}	6.5%	0.0208	0.0261
$MnFeO_x$@YS-ZSM-5	733	473.15	4.56×10^{-4}	8.7%	0.0203	0.0336

$C_{WP} < 1$, therefore, internal mass transfer effects can be neglected.

Mears Criterion for External (Interphase) Heat Transfer

The absence of heat transfer was checked by Mears' criterion:

$$C_{Me.} = \left| \frac{-\Delta H r_{obs} \rho_b R_p E_a}{h T_m{}^2 R_g} \right|$$

Where ΔH = heat of reaction, kJ mol^{-1}= -1.628×10^3 kJ mol^{-1};

r_{obs} = observed reaction rate ≈ $r = \frac{X_{NO_{x,m}} F_{NO_x}}{m_{cat.}}$, mol kg$_{cat.}{}^{-1}$ s^{-1};

F_{NO_x} = gas flow rate of NO_x, mol s^{-1};

$m_{cat.}$ = mass weight of the sample = 0.0250 g;

T_m = the maximum temperatures during NH_3-SCR kinetic measurements, K;

$X_{NO_{x,m}}$ = the NO_x conversion at maximum temperatures;

R_p = catalyst particle radius = 1.35×10^{-4} m;

ρ_b = bulk density of catalyst bed, kg m^{-3};

E_a = activation energy, kJ mol^{-1} (from **Figure S37**);

h = heat transfer coefficient between gas and pellet = 5.3 kJ m^{-2} s^{-1} K^{-1};

R_g = gas constant = 8.314 $\times10^{-3}$ kJ mol^{-1} K^{-1}.

Table S5. The $C_{Me.}$ over the various catalysts in NH_3-SCR performance.

Catalysts	ρ_b	T_m	r_{obs}	$X_{NO_{x,m}}$	E_a	$C_{Me.}$
$MnFeO_x$	2027	463.15	8.88×10^{-4}	17.0%	40.6	1.7×10^{-3}
$MnFeO_x$/ZSM-5	748	463.15	6.79×10^{-4}	13.0%	19.1	2.3×10^{-4}
$MnFeO_x$/S-1	782	433.15	3.40×10^{-4}	6.5%	19.6	1.4×10^{-4}
$MnFeO_x$@YS-ZSM-5	733	473.15	4.56×10^{-4}	8.7%	20.9	1.6×10^{-4}

$C_{Me.} < 0.15$, therefore, external (interphase) heat transfer effects can be neglected.

Table S6. The acidic properties of the fresh $MnFeO_x$, $MnFeO_x$/ZSM-5, $MnFeO_x$/S-1, $MnFeO_x$@YS-ZSM-5, and related K-poisoned catalysts.

Samples	Total acid amount (mmol g^{-1})	Weak acid amount (mmol g^{-1})	Medium and strong acid (mmol g^{-1})	The desorption peak temperature (°C) and the acid amount corresponding to this peak (mmol g^{-1})
$MnFeO_x$	0.055	0.044	0.011	108 (0.010), 171 (0.034), 263 (0.011)
$MnFeO_x$/ZSM-5	0.243	0.157	0.086	110 (0.048), 153 (0.109), 280 (0.086)
$MnFeO_x$/S-1	0.113	0.078	0.035	106 (0.033), 145 (0.045), 270 (0.035)
$MnFeO_x$@YS-ZSM-5	0.341	0.203	0.138	111 (0.031), 155 (0.172), 295 (0.138)
ZSM-5	0.237	0.170	0.067	115 (0.079), 158 (0.091), 352 (0.067)
S-1	0.085	0.071	0.014	103 (0.055), 135 (0.016), 222 (0.014)
K-$MnFeO_x$	0.037	0.027	0.010	104 (0.008), 161 (0.019), 263 (0.010)
K-$MnFeO_x$/ZSM-5	0.199	0.136	0.063	107 (0.038), 144 (0.098), 246 (0.063)
K-$MnFeO_x$/S-1	0.068	0.052	0.016	109 (0.023), 144 (0.029), 237 (0.016)
K-$MnFeO_x$@YS-ZSM-5	0.227	0.183	0.044	115 (0.071), 161 (0.112), 318 (0.044)

Table S7. The surface atomic concentrations and Mn^{4+} ratios of each sample.

Catalysts	Atomic Concentration (mol.%)							Surface species content (%)
	Mn	Fe	Si	Al	O	K	S	Mn^{4+}/Mn
$MnFeO_x$	17.44	13.92	-	-	68.64	-	-	39.6
$MnFeO_x$/ZSM-5	5.80	8.74	23.79	1.62	60.05	-	-	32.3
$MnFeO_x$@YS-ZSM-5	5.70	7.24	21.71	1.55	63.80	-	-	29.4
S-$MnFeO_x$	13.97	17.29	-	-	66.76	-	1.98	30.9
S-$MnFeO_x$/ZSM-5	7.21	9.33	20.23	1.11	60.70	-	1.42	24.4
S-$MnFeO_x$@YS-ZSM-5	5.45	8.31	23.87	1.31	60.59	-	0.47	28.3
K-$MnFeO_x$	18.80	17.31	-	-	63.21	0.68	-	32.9
K-$MnFeO_x$/ZSM-5	6.48	7.33	22.76	1.48	61.24	0.71	-	32.4
K-$MnFeO_x$@YS-ZSM-5	7.22	6.43	20.12	1.32	64.30	0.61	-	29.5

Supplementary References

[1] H. Wang, M. Lin, T. Murayama, S. Feng, M. Haruta, H. Miura, T. Shishido, *ACS Catal.* **2021**, 8576-8584.

[2] S. T. Oyama, X. Zhang, J. Lu, Y. Gu, T. Fujitani, *J. Catal.* **2008**, 257, 1-4.

[3] R. A, H. J, K. G, *Journal of Physics: Condensed Matter*. **2003**, 15, 979.

[4] G. Kresse, J. Furthmüller, *Comput. Mater. Sci.* **1996**, 6, 15-50.

[5] K. Burke, M. Ernzerhof, J. P. Perdew, *Phys. Rev. Lett.* **1996**, 77, 3865-3868.

[6] S. L. Dudarev, G. A. Botton, S. Y. Savrasov, C. J. Humphreys, A. P. Sutton, *Phys. Rev. B* **1998**, 57, 1505.

[7] O. Bengone, M. Alouani, P. Blöchl, J. Hugel, *Phys. Rev. B* **2000**, 62, 16392.

[8] B. Zhu, Q. Fang, Y. Sun, S. Yin, G. Li, Z. Zi, T. Ge, Z. Zhu, M. Zhang, J. Li, *J. Mater. Sci.* **2018**, 53, 11500-11511.

[9] A. Bouzoubaa, D. Costa, B. Diawara, N. Audiffren, P. Marcus, *Corros. Sci.* **2010**, 52, 2643-2652.

[10] I. Song, H. Lee, S. W. Jeon, I. A. M. Ibrahim, J. Kim, Y. Byun, D. J. Koh, J. W. Han, D. H. Kim, *Nat. Commun.* **2021**, 12, 901.

[11] X. Fang, Y. Liu, Y. Cheng, W. Cen, *ACS Catal.* **2021**, 11, 4125-4135.

[12] L. Han, S. Cai, M. Gao, J. Hasegawa, P. Wang, J. Zhang, L. Shi, D. Zhang, *Chem. Rev.* **2019**, 119, 10916-10976.

[13] J. Yang, X. Li, S. Lyu, S. Wang, Z. Chen, J. Zhu, *Appl. Catal. B: Environ. Energy* **2026**, 389, 126609.

[14] Z. Jia, Y. Shen, T. Yan, H. Li, J. Deng, J. Fang, D. Zhang, *Environ. Sci. Technol.* **2022**, 56, 2647-2655.

[15] C. Chen, Y. Wang, J. Li, F. Tian, W. Chen, C. Feng, Y. Pan, Y. Liu, *Appl. Catal. B: Environ. Energy* **2023**, 338, 123086.

[16] J. Yang, S. Ren, Y. Zhou, Z. Su, L. Yao, J. Cao, L. Jiang, G. Hu, M. Kong, J. Yang, et al., *Chem. Eng. J.* **2020**, 397, 125446.

[17] Z. Wang, R. Guo, X. Shi, X. Liu, H. Qin, Y. Liu, C. Duan, D. Guo, W. Pan, *Chem. Eng. J.* **2020**, 381, 122753.

[18] F. Liu, H. He, *Catal. Today*. **2010**, 153, 70-76.

[19] Z. Lian, F. Liu, H. He, X. Shi, J. Mo, Z. Wu, *Chem. Eng. J.* **2014**, 250, 390-398.

[20] Z. Chen, S. Ren, X. Xing, X. Li, L. Chen, M. Wang, *Fuel* **2023**, 335, 126986.

[21] Z. Chen, S. Ren, M. Wang, J. Yang, L. Chen, W. Liu, Q. Liu, B. Su, *Fuel* **2022**, 321, 124113.

[22] C. Gao, B. Xiao, J. Shi, C. He, B. Wang, D. Ma, Y. Cheng, C. Niu, *J. Catal.* **2019**, 380, 55-67.

[23] F. Zhao, G. Zhang, Z. Tang, F. Zha, *Fuel* **2022**, 322, 124185.

[24] Z. Chen, R. Guo, S. Ren, L. Chen, X. Li, M. Wang, *J. Mater. Chem. A* **2022**, 10, 21474-21491.

[25] Z. Fan, J. Shi, C. Gao, G. Gao, B. Wang, C. Niu, *ACS Appl. Mater. Interfaces* **2017**, 9, 16117-16127.

[26] X. Tang, C. Wang, F. Gao, Y. Ma, H. Yi, S. Zhao, Y. Zhou, *J. Environ. Chem. Eng.* **2020**, 8, 104399.

[27] J. Shi, Z. Zhang, M. Chen, Z. Zhang, W. Shangguan, *Fuel* **2017**, 210, 783-789.

[28] Y. Wei, P. Liang, Y. Li, Y. Zhao, X. Min, P. Tao, J. Hu, T. Sun, *J. Environ. Chem. Eng.* **2022**, 10, 107772.

[29] X. Huang, N. Fang, S. Wu, F. Dong, Y. Chu, Z. Tang, *Appl. Catal. B: Environ. Energy* **2024**, 343, 123518.

[30] Y. Wei, W. Li, Q. Wang, M. Liu, P. Liang, L. Wang, T. Sun, *J. Ind. Eng. Chem.* **2023**, 123, 209-219.

[31] J. Xu, T. Zheng, X. Zou, H. Shen, F. Guo, Q. Zhang, M. Duan, *J. Energy Inst.* **2024**, 112, 101458.

[32] G. Li, B. Wang, H. Wang, J. Ma, W. Q. Xu, Y. Li, Y. Han, Q. Sun, *Catal. Commun.* **2018**, 108, 82-87.

[33] L. Li, J. Ji, W. Tan, W. Song, X. Wang, X. Wei, K. Guo, W. Zhang, C. Tang, L. Dong, *J. Rare Earths* **2022**, 40, 1454-1461.

[34] Y. Ma, W. Liu, Z. Li, Y. Sun, M. Shi, Z. Nan, R. Song, L. Wang, J. Guan, *Molecules* **2023**, *28*, 3068.